Three-dimensional numerical models for free convection in porous enclosures heated from below

MSC. FERNANDO JAVIER GUERRERO MARTINEZ

Submitted in fulfilment of the requirements for the degree of Doctor of Philosophy at the University of Glasgow.

School of Engineering
University of Glasgow
January 2017

Abstract

Numerical modeling of free convection in porous enclosures is investigated in order to determine the best approaches to solve the problem in two and three dimensions considering their accuracy and computing time. Two case studies are considered: sloping homogeneous porous enclosures and layered porous enclosures due to their relevance in the context of geothermal energy. The governing equations are based on Darcy's law and the Boussinesq approximation. The mathematical problem of free convection in 2D homogeneous porous enclosures is solved following the well known stream function approach and also in terms of primitive variables.

The numerical schemes are based on the Finite Volume numerical method and implemented in Fortran 90. Steady-state solutions are obtained solving the transient problem for long simulation times. The case study of a sloping porous enclosure is used for comparison of the results of the two models and for validation against results reported in the literature. The two modeling approaches generate consistent results in terms of the Nusselt number, the stream function approach however, turns out a faster computational algorithm.

A parametric study is conducted to evaluate the Nusselt number in a 2D porous enclosure as a function of the slope angle, Rayleigh number and aspect ratio. Te convective modes can be divided into two classes: multicellular convection for small slope angles and single cell convection for large angles. The transition angle between these convective modes is dependent on both the Rayleigh number and the aspect ratio. High Rayleigh numbers allow multicellular convection to remain in a larger interval of angles.

This study is extended to the three-dimensional case in order to establish the range of validity of the 2D assumptions. As in the 2D modeling, two different approaches to solve the problem are compared: primitive variables and vector potential. Similarly, both approaches lead to equivalent results in terms of the Nusselt number and convective modes, the vector potential model however, proved to be less mesh-dependent and also a faster algorithm. A parametric study of the problem considering Rayleigh number, slope angle and aspect ratio showed that convective modes with irregular 3D geometries can develop in a wide variety of situations, including horizontal porous

enclosure at relatively low Rayleigh numbers. The convective modes obtained in the 2D analysis (multicellular and single cell) are also present in the 3D case. Nonetheless the 3D results show that the transition between these convective modes follows a complex 3D convective mode characterized by the interaction of transverse and longitudinal coils. As a consequence of this, the transition angles between multicellular and single cell convection as well as the location of maxima Nusselt numbers do not match between the 2D and 3D models.

Finally in this research, three-dimensional numerical simulations are carried out for the study of free convection in a layered porous enclosure heated from below and cooled from the top. The system is defined as a cubic porous enclosure comprising three layers, of which the external ones share constant physical properties and the internal layer is allowed to vary in both permeability and thermal conductivity. A parametric study to evaluate the sensitivity of the Nusselt number to a decrease in the permeability of the internal layer shows that strong permeability contrasts are required to observe an appreciable drop in the Nusselt number. If additionally the thickness of the internal layer is increased, a further decrease in the Nusselt number is observed as long as the convective modes remain the same, if the convective modes change the Nusselt number may increase. Decreasing the thermal conductivity of the middle layer causes first a slight increment in the Nusselt number and then a drop. On the other hand, the Nusselt number decreases in an approximately linear trend when the thermal conductivity of the layer is increased.

Acknowledgments

This thesis represents the conclusion of around three years and a half of research. I would like to express my sincere gratefulness to the following people and institutions that in many ways supported my work:

To the National Council for Science and Technology (CONACYT) and Cluff Geothermal Ltd. for funding this research.

To my supervisor, Professor Paul Younger, for his enthusiastic reception of my research proposal. For his support and advise throughout my studies.

To my second supervisor Dr. Nader Karimi for invaluable discussions and his dedication to the topic addressed in this project. To Dr. Manosh C. Paul, Dr. Elsa Báez, and Dr. Robert Westaway for their support and helpful comments to my work. To Dr. Angela Busse and Dr. Andrew Rees for helpful comments to this thesis.

A special acknowledgment to the geologists Dr. Michael Feliks and Tom Elliot for the opportunity of collaborating with them in their geological and energy modelling of geothermal systems.

To Mrs Elaine McNamara and Mrs Heather Lambie of the University of Glasgow for answering my endless questions and being always willing to help.

To my friends from Mexico: Daniela Aguirre, Xóchitl Alvarado, Manuel Escareño, Armando Garduño, Diego Martínez, and Alejandro Vázquez. To my friends from Glasgow: Kathleen Smyth and Fatima Khan, and my colleagues and friends from the Univeristy of Glasgow: Daniel Agbo, Juan Álvarez, Sotirios Kyriakis, Alessandro Peloni, Helen Robinson, Linwei Wang, Aaron Williams, and Anggoro Wisaksono.

I express my most sincere gratitude to my family for their support and love.

Declarations

Part of the work presented in this thesis has been published in the following articles:

- Three-dimensional numerical simulations of free convection in a layered porous enclosure. Fernando J. Guerrero-Martínez, Paul L. Younger, Nader Karimi and Sotirios Kyriakis. *International Journal of Heat and Mass Transfer*, 2017, vol. 106.
- Three-dimensional numerical modeling of free convection in sloping porous enclosures. Fernando J. Guerrero-Martínez, Paul L. Younger and Nader Karimi. *International Journal of Heat and Mass Transfer*, 2016, vol. 98.
- Three-dimensional numerical modeling of free convection in a layered porous medium. Fernando J. Guerrero-Martínez, Paul L. Younger and Nader Karimi. 7th European Geothermal PhD Day, Bari, Italy, 2016.
- Geothermal systems simulation: a case study. Fernando J. Guerrero-Martínez, Paul L. Younger and Manosh C. Paul. Proceedings World Geothermal Congress, Melbourne, Australia, 2015.
- Geothermal Reservoir Simulation. Fernando J. Guerrero-Martínez. International workshop on geomechanics and energy, the ground as energy source and storage. EPFL, Lausanne, Switzerland, 2013.

I declare that, except when explicit reference is made to the contribution of others, this thesis is my own work and it has not been submitted for any other degree at the University of Glasgow or any other institution.

Fernando Javier Guerrero-Martínez

Mexico City, January 2017

Nomenclature

Greek symbols

α	Slope angle
β	Thermal expansion coefficient
$\boldsymbol{\psi}$	Vector potential
η	Overall thermal diffusivity
γ	Specific weight
κ	Thermal conductivity
Ω	Surface boundary
σ	Ratio of heat capacities
θ	Dimensionless temperature
φ	Porosity

Other symbols

$-$	Overbar denotes dimensional variable

Roman letters

$\hat{A}$	Amplitude
A	Area
B	Characteristic length
c	Specific heat
D	Aspect ratio
g	Gravitational constant
h	Height or piezometric head

J	Hydraulic gradient
K	Hydraulic conductivity
k	Permeability
L	Characteristic length
L_∞	Infinity norm
n	Number of cells
Nu	Nusselt number
P	Pressure
Q	Volumetric flow rate
$q, \mathbf{u}$	Darcy's velocity
Ra	Darcy-Rayleigh number
T	Temperature
t	Time
x, y, z	Cartesian coordinates

Subscripts

0	Reference quantity
c	Critical quantity
cpu	Computing
f	Fluid phase
l	Local value
m	Overall value
s	Solid phase
ss	Steady state

Contents

List of Figures

List of Tables

Chapter 1

Introduction

The problem of free convection in porous media has been of great interest in research due to the widespread presence of this mode of heat transfer in both nature and engineering processes. In recent decades, the need for clean and renewable energy resources as well as new environmental policies have motivated an intense research in this topic. In the context of bioclimatic architecture, this topic is important to model thermal isolation in buildings; CO_2 sequestration, nuclear waste storage, transport of pollutants in soil-water systems, and oil recovery treatments are some other application fields of this topic.

Geothermal reservoir and ground water modeling are two application areas in which free convection in porous media is particularly important. Fluid flow patterns in the earth crust can be strongly influenced by this heat transfer mode particularly in the ocean crust (Fisher 1998, Jupp & Schultz 2004). Thermal gradients in fractured-porous media can drive density-driven flow (Graf & Therrien 2009) that generates thermal anomalies of interest in geothermal applications (Gvirtzman et al. 1997, Guillou-Frottier et al. 2013, Souche et al. 2014).

Modelling geothermal systems involves multidisciplinary work for which numerical models are a fundamental tool of analysis. Numerical models are employed either to evaluate conceptual models (O'Sullivan et al. 2001, Mannington et al. 2004, Noorollahi & Itoi 2011, Franco & Vaccaro 2012), or to study a variety of physical and chemical processes that take place in geothermal reservoirs with a phenomenological approach (Ingebritsen et al. 2010, Wellmann & Regenauer-Lieb 2015). An overview of numerical modeling of geothermal systems and the approaches to model fluid flow and heat transfer in rocks is presented in Appendix A.1 for further details about this topic. This thesis is concerned with the second category of models. The phenomenological study presented here aims at describing the convective patterns and heat transfer properties in three-dimensional porous enclosures.

Geothermal systems are very often confined into geological units characterized by

some degree of inclination with respect to the surface level, so that gravitational effects can affect the fluid flow in all directions of the three-dimensional (3D) space. Likewise, the presence of layers with different physical properties, such as permeability and thermal conductivity, is a common feature of these systems. These two aspects of the problem of free convection in porous media will be the main interest of this work. The modeling approach to address these problems will be based on the continuum assumption which is commonly made in the context of geothermal systems (Appendix A.1).

The topics of free convection in sloping and layered porous media have been widely investigated from a theoretical perspective and numerically mainly by means of 2D models. The scarcity of three-dimensional models is partly due to the associated high computational demand and partly to the fact that 2D studies often provide enough insight into the physics of the problem. Extending the conclusions of 2D analysis to 3D systems must be done with care however, since in some cases 2D models do not allow to observe qualitative behavior only observable in 3D analysis even when the governing parameters of the problem seem to justify the 2D assumption.

1.1 Objectives

The general objectives of this thesis are the following:

1. To develop and validate a phenomenological model for free convection in a porous enclosure in three dimensions.
2. To carry out a parametric study of steady-state free convection in a sloping porous enclosure and compare it with previous 2D results.
3. To carry out a parametric study of steady-state free convection in a layered porous enclosure to obtain the qualitative behaviour of the convective modes and heat transfer.

To achieve this, the following specific objectives have been set:

1. To carry out a literature review on free convection in porous enclosures in 2D and 3D as well as the context of application of this problem.
2. To develop a 2D numerical model for free convection in a homogeneous porous enclosure based on the Finite Volume numerical method and implemented in Fortran code.

3. To carry out an investigation on the approaches to solve the problem numerically in 3D. The approaches will be implemented in Fortran, validated and compared in terms of numerical stability and accuracy.

4. To carry out parametric studies of the problem of free convection in a sloping homogeneous porous enclosure and in a layered porous enclosure.

This thesis is structured in five chapters. The remaining sections of this chapter are dedicated to introducing basic assumptions and the governing equations of the problem of free convection in porous media. Specific literature reviews according with the case studies analyzed are presented in the introduction sections of Chapters 2, 3, and 4. Additionally, a more general literature review on the context of application is presented in Appendix A.1. Two numerical models to solve the problem of free convection in porous media in 2D will be presented in Chapter 2: the primitive variables approach and the stream function approach. These numerical schemes will be developed using the case study of a sloping porous enclosure. These models will be compared and validated against results available in the literature. Additionally, a parametric analysis will be also presented to evaluate the impact of three governing parameters on the heat transfer capacity of the porous enclosure. The models presented in Chapter 2 will be the basis for the 3D numerical models presented in subsequent chapters. Chapter 3 presents the three-dimensional version of the problem analized in Chapter 2, two 3D models are compared in this chapter: primitive variables and vector potential, which can be considered the 3D counterpart of the stream function method. A numerical model for free convection in a layered porous medium is presented in Chapter 4 using as a case study a three-layer porous enclosure. A parametric study is then presented to evaluate the effect of permeability and thermal conductivity contrast between the layers. Finally, Chapter 5 presents the concluding remarks of this work.

1.2 Governing equations

1.2.1 Darcy's law

Fundamental aspects for the study of this topic rest on the experimental work published by the French engineer Henry Darcy in 1856. Motivated by the need of a reliable water supply system for his city of origin, Dijon, he developed a comprehensive study covering aspects as water sources, transport, and distribution (Freeze 1994, Simmons 2008). One of the most important contributions he made to the rising discipline of hydraulics is the determination of an empirical law governing the water flow through sand. Evaluating the discharge of water flowing through a vertical

column packed with sand he stablished that the discharge is directly proportional to the head and inversely proportional to the thickness of the layer traversed. This statement is given by the following equation (Bear 1979),

$$Q = KA\frac{h_1 - h_2}{L}, \tag{1.1}$$

where Q is the volumetric flow rate of water, A and L are the cross-section area and height of the sand column, respectively, K is a constant of proportionality called hydraulic conductivity that depends on the permeability of the medium, k, and properties of the fluid $K = \frac{k\rho g}{\mu}$. h_1 and h_2 represent the piezometric head measured at the top and bottom sections of the column, respectively. Equation 1.1 is commonly written in terms of the hydraulic gradient defined as $J = \frac{h_1 - h_2}{L}$ and the volumetric flow rate through a unit cross sectional area, q, known as Darcy's velocity.

$$q = KJ \tag{1.2}$$

The piezometric head accounts for pressure head and elevation head, $h = \frac{\bar{P}}{\gamma} + \bar{z}$.[1]Additionally, $h_1 - h_2$ represents a head loss, which is energy loss per unit weight. This energy loss is due to the viscous resistance of the fluid as it moves through the tortuous paths of the porous medium. An implication of Darcy's law is that kinetic energy changes in the fluid as it flows through the sand column are negligible. This imposes a range of validity for Equation 1.2. Kolditz (2001) pointed out that the upper limit for the validity of the Darcy's law is well before the transition from laminar to turbulent flow (Re$\sim$10), this condition is satisfied in most cases in groundwater flow.

It is important to note that Darcy's results state that flow takes place in the direction of decreasing head, rather than the direction of decreasing pressure. The fluid moves in the direction of decreasing pressure only in the case of a horizontal sand column where gravity is not the driving mechanism of the flow. From this considerations it can be stated that a difference in piezometric head represents a potential for the flow. This potential is described mathematically by means of the gradient of h, so that the volumetric flow rate per unit area is given by the following equation in a more general form.

$$\mathbf{q} = -K\bar{\nabla}h \tag{1.3}$$

The average velocity of the flow through the column is obtained from the effective cross section area available for the flow of fluid, which is the cross section area, A,

[1]Overbar notation will be used to refer to dimensional variables and operators in case a dimensionless counterpart is required in further sections of the thesis.

multiplied by the porosity, φ. For three-dimensional flow we have that (Bear 1979)

$$\mathbf{V} = \frac{\mathbf{q}}{\varphi} \tag{1.4}$$

Homogeneous and heterogeneous porous media

A porous medium is said to be homogeneous when the permeability does not vary with the position (the same applies to the hydraulic conductivity). A homogeneous porous medium can be *isotropic* or *anisotropic*. An isotropic porous medium is that for which the permeability is independent of the direction. On the other hand, the medium is anisotropic when the permeability depends on the direction of the flow, so that it is a tensor with components k_x, k_y and k_z.

A heterogeneous porous medium is that for which the permeability varies with the position. Bear (1979) distinguishes two types of heterogeneity depending on the way the permeability varies. In the first type the permeability is a continuous function of the spatial coordinates. The second type involves discontinuities (abrupt changes) in the permeability distribution. The main interests of this research are homogeneous isotropic porous media as well as layered porous media, so that the permeability is allowed to vary in the direction of z-axis parallel to gravity. Likewise, the heterogeneity considered in the present work will be of the first type so that only continuous changes in the physical properties will be considered, nonetheless this approach is capable of representing layers with enough accuracy.

1.2.2 Momentum equation

For the purposes of this work $\mathbf{q}$ and $\bar{\mathbf{u}} = (\bar{u}, \bar{v}, \bar{w})$ will be used as equivalent notation to refer to Darcy's velocity. Considering the definitions of hydraulic conductivity and piezometric head the components of Equation 1.3 for a homogeneous porous medium the momentum equation can be written as follows

$$\bar{u} = -\frac{k}{\mu}\frac{\partial \bar{P}}{\partial \bar{x}}, \tag{1.5}$$

$$\bar{v} = -\frac{k}{\mu}\frac{\partial \bar{P}}{\partial \bar{y}}, \tag{1.6}$$

$$\bar{w} = -\frac{k}{\mu}\left(\frac{\partial \bar{P}}{\partial \bar{z}} + \rho g\right). \tag{1.7}$$

The driving forces of motion in this equation are classified as external and body forces. External forces are those associated with pressure gradients, whereas body forces are

associated with gravitational effects, which are only important for the component $\bar{z}$ of the system.

1.2.3 Heat transfer equation

The energy transport throughout a porous medium saturated with fluid is derived under the assumptions that there exists local thermal equilibrium between the porous matrix and the fluid and that viscous dissipation is negligible. This corresponds to the simplest case to model convection in porous media. These assumptions require that there are no drastic temperature changes in the system. The condition $\beta T(g\beta/c_{Pf})L << 1$ has also to be satisfied in order to neglect viscous dissipation, where c_{Pf} is the specific heat of the fluid at constant pressure. These conditions are usually satisfied in free convection in porous media (Nield & Bejan 2013). Furthermore, it is assumed that density and specific heat do not vary with time nor position. The thermal conductivity however, will be in general considered a function of the spatial coordinates. Some of these assumptions are contained within the Boussinesq approximation, defined in Section 1.2.5. Additionally, it is assumed that there are no heat sources in the porous medium. Under these assumptions, the energy balance is made up of conductive and convective heat transfer in the medium and takes the form (Nield & Bejan 2013):

$$(1-\varphi)(\rho c)_s + \varphi(\rho c_P)_f \frac{\partial \bar{T}}{\partial \bar{t}} + (\rho c_P)_f \bar{\mathbf{u}} \cdot \bar{\nabla}\bar{T} = \bar{\nabla} \cdot ((1-\varphi)\kappa_s + \varphi\kappa_f \bar{\nabla}\bar{T}), \tag{1.8}$$

this equation can be rewritten using the subscript m that denotes overall value and f, fluid phase:

$$(\rho c)_m \frac{\partial \bar{T}}{\partial \bar{t}} + (\rho c)_f \bar{\mathbf{u}} \cdot \bar{\nabla}\bar{T} = \bar{\nabla} \cdot (\kappa_m \bar{\nabla}\bar{T}), \tag{1.9}$$

finally, the heat transfer equation can be simplified as follows:

$$\sigma \frac{\partial \bar{T}}{\partial \bar{t}} + \bar{\mathbf{u}} \cdot \bar{\nabla}\bar{T} = \bar{\nabla} \cdot (\eta \bar{T}), \tag{1.10}$$

where σ is the scaling factor $\sigma = (\rho c)_m/(\rho c_P)_f$, and η represents the overall thermal diffusivity.

1.2.4 Mass conservation

A mass balance in a control volume in a porous medium saturated with fluid is the result of quantifying inputs and outputs of fluid in the control volume plus density

variations with time. The result is the continuity equation:

$$\frac{\partial \rho}{\partial \bar{t}} + \bar{\nabla} \cdot (\rho \bar{\mathbf{u}}) = 0 \tag{1.11}$$

Keeping the assumption of constant density as regards the position and time the mass balance takes the form of the continuity equation for an incompressible fluid:

$$\bar{\nabla} \cdot \bar{\mathbf{u}} = 0 \tag{1.12}$$

1.2.5 The Boussinesq approximation

Free (or natural) convection is a heat transfer process induced by density-driven flow as a result of thermal expansion in a fluid. Density gradients due to thermal expansion in a fluid give rise to buoyancy, a body force that produces motion. In order to define such body force it is necessary to find a relation between density and temperature. The simplest equation is:

$$\rho(\bar{T}) = \rho_0 - \rho_0 \beta_0 (\bar{T} - \bar{T}_0), \tag{1.13}$$

which is derived from a Taylor series for ρ as a function of $\bar{T}$, considering the pressure P to be constant, and keeping only the first two terms of the series (Bird et al. 2002). The subindex 0 refers to values calculated at the mean temperature between the highest and the lowest temperatures of the system $\bar{T}_0 = \frac{1}{2}(\bar{T}_H + \bar{T}_C)$.

The Boussinesq approximation states that density variations are only significant in the buoyancy term, and can be neglected elsewhere. This definition is commonly extended to other properties (Nield & Bejan 2013), so that all the physical properties of the medium are set constant except the density involved in the buoyancy term (Eq. 1.7). Density variations in free convection are normally small enough to justify the assumption of incompressible flow. For large density gradients however, the Boussinesq approximation cannot be applied, Ingebritsen et al. (2010) describes some examples of geological systems in which this assumption is not justified. Tritton (1988) presents a theoretical examination of the conditions for the Boussinesq approximation to be a good approximation. An alternative approach to incorporate density gradients can be referred to Evans & Raffensperger (1992).

Writing the body force in Equation 1.7 in terms of Equation 1.13, the momentum equation turns out

$$\bar{u} = -\frac{k}{\mu}\frac{\partial \bar{P}}{\partial \bar{x}}, \tag{1.14}$$

$$\bar{v} = -\frac{k}{\mu}\frac{\partial \bar{P}}{\partial \bar{y}}, \tag{1.15}$$

$$\bar{w} = -\frac{k}{\mu}\left(\frac{\partial \bar{P}}{\partial \bar{z}} + \rho_0 g(1 - \beta_0(\bar{T} - \bar{T}_0)\right). \tag{1.16}$$

The equation can be simplified redefining the vertical pressure gradient so it is taken relative to a reference hydrostatic pressure gradient $\rho_0 g$. This leads to the most common version of the momentum equation based on Darcy's law and the Boussinesq approximation. In vectorial form this equation is

$$\bar{\mathbf{u}} = -\frac{k}{\mu}\left(\bar{\nabla}\bar{P} - \rho_0\beta_0(\bar{T} - \bar{T}_0)\mathbf{g}\right). \tag{1.17}$$

Once the governing equations have been stated, the problem of free convection in a porous enclosure can be formulated in mathematical terms. The numerical solution of this mathematical problem and case studies will be presented in the following chapters.

Chapter 2

2D free convection in a homogeneous porous enclosure

2.1 Introduction

Several studies of free convection in porous media in 2D have been carried out in the past. Fundamental aspects of the problem are given by the solution of the Horton-Rogers-Lapwood problem (Nield & Bejan 2013). The solution to this problem establishes the conditions for the onset of convection in a horizontal porous layer heated from below. The early works by Horton & Rogers (1945) and Lapwood (1948) determined a critical Rayleigh number ($Ra_c = 4\pi^2$) for the onset of convection in such a system. Elder (1967) presented one of the first numerical and experimental studies of steady state convection in a two-dimensional (2D) porous enclosure. He described the steady state cellular motion of the fluid, incorporating edge-effects of the porous enclosure. Straus (1974) carried out stability analysis of 2D convection in a horizontal porous layer, he showed that as the Rayleigh number increases the wavenumber increases, and for $Ra \geq 380$ there are no stable 2D solutions. In the same context, De La Torre Juárez & Busse (1995) showed that the maximum Nusselt number of steady-state convection shifts towards higher wavenumbers as Ra increases.

Kaneko et al. (1974) extended the experimental study by Elder (1967) to an inclined porous enclosure. They pointed out that there is an angle at which the system reaches the maximum level of convective motion, characterized by multiple convective cells, they reported that above this angle the system evolves towards single cell convection. Moya et al. (1987) studied numerically steady state convection in inclined porous enclosures and the transition between multicellular convective pattern and single cell as the slope angle and Rayleigh number were varied, as well as the existence of multiplicity of steady state solutions. Their model successfully reproduced the appearance of a single cell convective regime when $Ra\cos\alpha < 4\pi^2$ and $15 < \alpha < 80$, which was

experimentally obtained by Bories & Combarnous (1973). Sen et al. (1987) studied multiplicity of solutions of this kind of system following an analytical and numerical approach. They found that only one steady state solution exists for sub-critical Rayleigh numbers. For higher Rayleigh numbers however, when the inclinations with respect to the heated wall are small enough, multiple steady states exist and some of them are unstable. Riley & Winters (1990) described the mechanisms through which multiplicity of solutions characteristic of small slope angles reduces to leave an apparently unique solution for large slope angles. Rees & Bassom (2000) presented a linear stability analysis for the onset of convection in a sloping porous layer heated from below. They found the maximum inclination angle at which transverse convective modes can become unstable, which is $\alpha = 31.49°$ corresponding to a critical Rayleigh number of 104.30. More recently, Báez & Nicolás (2006) studied the problem considering a wide parameter space. They analyzed how the transition angle between multicellular and single-cell convection is affected by the Rayleigh number. They pointed out that a coarse numerical discretization can affect the number of convective cells of multicellular convection, which is again an expression of multiplicity of solutions. This problem has been further extended to the analysis of oblique porous enclosures (Baytaş & Pop 1999) and entropy generation (Baytaş 2000), and also to turbulence (Carvalho & de Lemos 2013) and non-Darcian effects (Khanafer 2013).

Two numerical schemes of free convection in a homogeneous porous enclosure are presented in this chapter: the stream function approach and primitive variables approach. These numerical schemes will be the basis for the presentation of the 3D models in the following chapters. Steady-state solutions are obtained from the simulation of the transient problem for long simulation time using a convergence criterion. The steady-state solutions obtained with the models presented here will be validated agains results available in the literature (Baytaş 2000, Báez & Nicolás 2006).

2.2 Problem formulation

The problem consists of a rectangular porous enclosure of height B and length C with impermeable walls, heated from below, and inclined an angle α with respect to the horizontal position (Figure 2.1). The basic assumptions presented in Section 1.2 are kept for this problem: local thermal equilibrium, fluid flow is described by Darcy's law, and the Boussinesq approximation is invoked. From these considerations the momentum equation can be stated as follows (the bar notation denotes dimensional variables and operators):

$$\bar{\mathbf{u}} = -\frac{k}{\mu}\left(\bar{\nabla}\bar{P} - \rho_0 g \beta_0 (\bar{T} - \bar{T}_0)\mathbf{e}\right) \tag{2.1}$$

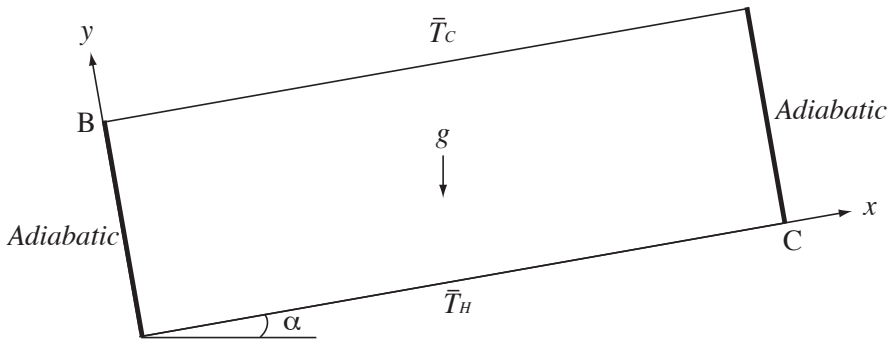

Figure 2.1: Schematic model of a rectangular porous enclosure tilted an angle α.

where the vector $\mathbf{e} = (\sin\alpha, \cos\alpha)$ gives account of the components of the buoyancy term in the system. The continuity equation for an incompressible fluid is also recalled

$$\bar{\nabla} \cdot \bar{\mathbf{u}} = 0. \tag{2.2}$$

Likewise, the heat transfer equation is as follows:

$$\sigma \frac{\partial \bar{T}}{\partial \bar{t}} + \bar{\mathbf{u}} \cdot \bar{\nabla} \bar{T} = \bar{\nabla} \cdot (\eta \bar{\nabla} \bar{T}). \tag{2.3}$$

The problem is nondimensionalized using the following dimensionless variables:

$$x = \frac{\bar{x}}{B}, \quad y = \frac{\bar{y}}{B}, \quad z = \frac{\bar{z}}{B}, \quad P = \frac{k}{\mu\eta}\bar{P},$$

$$\mathbf{u} = \frac{B}{\eta}(\bar{u}, \bar{v}, \bar{w}), \quad \theta = \frac{\bar{T} - \bar{T}_0}{\bar{T}_0 - \bar{T}_c}, \quad t = \frac{\bar{t}\eta}{\sigma B^2},$$

$$Ra = \frac{Bkg\beta\rho_0}{\eta\mu}(\bar{T}_0 - \bar{T}_c),$$

with Ra the Darcy-Rayleigh number (or simply the Rayleigh number). The dimensionless problem can be given as follows:

$$\mathbf{u} + \nabla P = Ra\theta\mathbf{e}, \tag{2.4}$$

$$\frac{\partial \theta}{\partial t} - \nabla^2\theta + \mathbf{u} \cdot \nabla\theta = 0, \tag{2.5}$$

$$\nabla \cdot \mathbf{u} = 0. \tag{2.6}$$

2.2.1 Boundary and initial conditions

It is assumed that the system rests at thermal and mechanical equilibrium as the initial condition. The initial dimensionless temperature is set to zero:

$$\theta = 0, \quad \text{for} \quad t = 0,$$

the boundary conditions for the heat transfer equation are as follows

$$\frac{\partial \theta}{\partial x} = 0, \quad \text{for} \quad x = 0 \quad \text{and} \quad x = D,$$

where D is the aspect ratio C/B, and

$$\theta = 1, \quad \text{for} \quad y = 0 \quad \text{and} \quad t > 0,$$

$$\theta = 0, \quad \text{for} \quad y = 1 \quad \text{and} \quad t > 0.$$

As regards the momentum equation, since the walls of the enclosure are impermeable, the perpendicular component of the velocity to the walls is set to zero. No restriction is imposed on the tangential velocity however, since the porous medium allows tangential motion at the boundaries. This is due to the fact that the Darcy model is based on a macroscopic view of the system, in which the fluid in the porous matrix is viewed as a unconfined continuum:

$$u = 0, \quad \text{for} \quad x = 0 \quad \text{and} \quad x = D,$$

$$v = 0, \quad \text{for} \quad y = 0 \quad \text{and} \quad y = 1.$$

The implementation of these boundary conditions as well as the initialization of the pressure will be described in the following sections according with two approaches that will be used to solve the mathematical problem, primitive variables and stream function methods.

2.3 Primitive variables approach

The primitive variables approach has been particularly associated with the solution of the Navier-Stokes equations in the context of splitting (or projection) methods (Davis & Jones 1983, Orszag et al. 1986, Karniadakis et al. 1991, Báez & Nicolás 2013). This method permits a non iterative solution of the system given by Equations 2.4 to 2.6 in each time step, which makes it easy to implement in a computational code. To describe this algorithm, let us recall the dimensionless momentum equation (Eq. 2.4):

$$\mathbf{u} + \nabla P = Ra\theta\mathbf{e}$$

the divergence of this equation considering the incompressibility condition $\nabla \cdot \mathbf{u} = 0$ leads to a Poisson equation

$$\nabla^2 P = Ra \nabla \cdot \theta \mathbf{e} \tag{2.7}$$

On the other hand, the dimensionless heat transfer equation remains the same as Equation 2.5. So that the problem can be summarized as follows:

$$\frac{\partial \theta}{\partial t} - \nabla^2 \theta + \mathbf{u} \cdot \nabla \theta = 0, \tag{2.8}$$

$$\Gamma \nabla^2 P = \left(\frac{\partial \theta}{\partial x} \sin \alpha + \frac{\partial \theta}{\partial y} \cos \alpha \right), \tag{2.9}$$

with $\Gamma = 1/Ra$.

The algorithm for each time step can be summarized as a three-step process (Fig. 2.2): The heat transfer equation is solved first (Eq. 2.8); once the temperature is known, the Poisson equation for the pressure is solved (Eq. 2.9); finally, the velocity field is obtained explicitly from the momentum equation (Eq. 2.4). The first two steps of this algorithm are the computationally expensive steps, they require the definition of matrices for the temperature and the pressure and the iterative solution of these matrices.

Boundary conditions

The boundary conditions for the heat transfer equation were described in Section 2.2.1. As regards the Poisson equation (Eq. 2.7), Neumann boundary conditions for the pressure are obtained from the momentum equation (Eq. 2.4) as follows, if the boundary of the porous enclosure is defined by a surface Ω, the pressure gradient normal to the surface must satisfy the following condition:

$$\frac{\partial P}{\partial \mathbf{n}}\Big|_{\Omega} = \mathbf{n} \cdot (Ra\theta \mathbf{e} - \mathbf{u})|_{\Omega} \tag{2.10}$$

This condition ensures mass conservation (Orszag et al. 1986, Báez & Nicolás 2013) which permits a non iterative algorithm to solve the system of differential equations. Considering the no flow condition through the walls, the velocity normal to the surfaces is zero. There is no restriction however, for the tangential velocity since the porous medium does not restrict the tangential motion at the boundary.

2.3.1 Discrete problem

The problem given by Equations 2.8 and 2.9 can be discretized by means of Finite Differences, Finite Element, and Finite Volume numerical methods. Of these methods the Finite Volume and Finite Differences are similar in the sense that equivalent

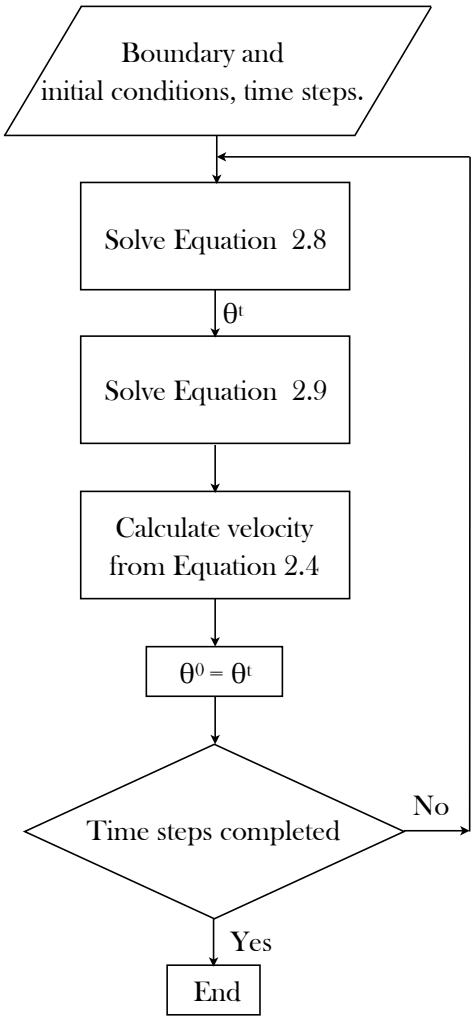

Figure 2.2: Flow diagram of the primitive variables algorithm to solve free convection in porous media.

meshes and time steps would lead to an equivalent set of algebraic equations. In this work the Finite Volume numerical method was chosen to carry out the discretization of the system. The equations were discretized using a structured and uniform mesh with mesh elements of aspect ratio 1. The notation presented by Versteeg & Malalasekera (1995) is used here: lowercase subscripts denote positions at the faces of the control volumes and capital subscripts denote positions at the centers of the control volumes. Both pressure and temperature can be calculated in cell centers (Fig. 2.3). This is possible because the velocities are given in terms of the pressure gradient in the direction of the flow (Darcy's law), this makes the approximation of velocities at cell faces straightforward, applying central differencing approximations for the pressure gradient from cell centers.

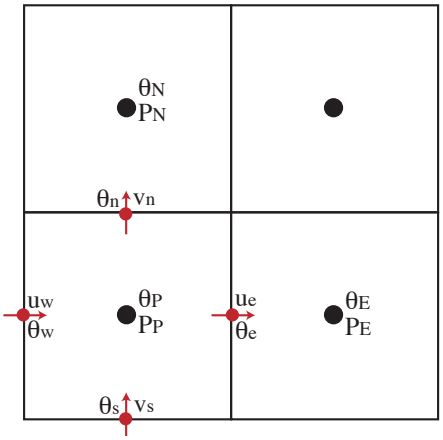

Figure 2.3: Finite volume mesh for the estimation of u_e, u_w, v_n, v_s, θ_e and θ_w. Both scalar variables, temperature and pressure are calculated at cell centers.

Discrete heat transfer equation

The integration of the heat transfer equation in a control volume was carried out using the central differencing scheme for the convective term, which is second order, and a first order fully implicit scheme was applied for the temporal discretization. This leads to the following discrete equation:

$$a_P\theta_P = a_E\theta_E + a_W\theta_W + a_N\theta_N + a_S\theta_S + s_P, \tag{2.11}$$

with

$$a_E = \frac{A_e}{\delta x} - \frac{u_e A_e}{2}, \quad a_W = \frac{A_w}{\delta x} + \frac{u_w A_w}{2},$$

$$a_N = \frac{A_n}{\delta y} - \frac{v_n A_n}{2}, \quad a_S = \frac{A_s}{\delta y} + \frac{v_s A_s}{2},$$

and

$$a_P = a_E + a_W + a_N + a_S + \frac{\Delta V}{\Delta t}, \quad s_P = \theta^0 \frac{\Delta V}{\Delta t}.$$

Boundary control volumes

West boundary: Neumann condition, adiabatic wall with impermeable boundary.

$$a_W = 0$$

East boundary: Neumann condition, adiabatic wall with impermeable boundary.

$$a_E = 0$$

South boundary: Dirichlet condition, $\theta = \theta_H$.

$$a_P\theta_P = a_E\theta_E + a_W\theta_W + a_N\theta_N + 2a_S\theta_H + s_P,$$
$$a_P = a_E + a_W + a_N + 2a_S + \frac{\Delta V}{\Delta t}.$$

North boundary: Dirichlet condition, $\theta = \theta_C$.

$$a_P\theta_P = a_E\theta_E + a_W\theta_W + a_S\theta_S + 2a_N\theta_C + s_P,$$
$$a_P = a_E + a_W + 2a_N + a_S + \frac{\Delta V}{\Delta t}.$$

Discrete Poisson equation for the pressure

The integration of Equation 2.9 in a control volume turns out (Appendix B)

$$a_P P_P = a_E P_E + a_W P_W + a_N P_N + a_S P_S - s_P, \tag{2.12}$$

with

$$a_E = \frac{\Gamma_e A_e}{\delta x}, \quad a_W = \frac{\Gamma_w A_w}{\delta x}, \quad a_N = \frac{\Gamma_n A_n}{\delta y}, \quad a_S = \frac{\Gamma_s A_s}{\delta y},$$

and

$$a_P = a_E + a_W + a_N + a_S.$$

These coefficients are written in the general form, however we can drop the subindexes of $\Gamma = 1/Ra$ since it is a constant. The source term s_P (buoyancy term) is obtained as follows:

$$s_P = \int_s^n \int_w^e \left(\frac{\partial\theta}{\partial x}\sin\alpha + \frac{\partial\theta}{\partial y}\cos\alpha\right) dxdy = \int_s^n \sin\alpha(\theta_e - \theta_w)dy + \int_w^e \cos\alpha(\theta_n - \theta_s)dx$$
$$= \sin\alpha(\theta_e - \theta_w)\delta y + \cos\alpha(\theta_n - \theta_s)\delta x.$$

Boundary control volumes

West boundary: Neumann condition, impermeable wall.

Considering the boundary condition for the momentum equation (Eq. 2.10) we have that the pressure gradient at the west boundary (WB) is the following:

$$\frac{\partial P}{\partial \mathbf{n}}\Big|_{WB} \simeq \frac{P_P - P_W}{\delta x} = Ra\theta_{WB}\sin\alpha,$$

this is equivalent to

$$\Gamma \frac{P_P - P_W}{\delta x} = \theta_{WB} \sin \alpha.$$

Since the west wall is adiabatic we have that $\theta_{WB} = \theta_P$, with θ_P the temperature of the adjacent control volume, which is always known. When the term $\Gamma \frac{P_P - P_W}{\delta x}$ is substituted by $\theta_{WB} \sin \alpha$ in the integrated form of Equation 2.7 it can be seen that the coefficient a_W no longer appears and there is an additional source term (the integration of a Poisson equation is presented in more detail in Appendix B). Therefore, the corrections for the discrete momentum equation (Eq. 2.12) are as follows:

$$a_W = 0, \quad s_P = \sin \alpha(\theta_e - \theta_w)\delta y + \cos \alpha(\theta_n - \theta_s)\delta x + \theta_{WB} \sin \alpha \delta y.$$

East boundary: Neumann condition, impermeable wall.

Similarly, for the east boundary (EB) we have that

$$\frac{\partial P}{\partial \mathbf{n}}\Big|_{EB} \simeq \frac{P_E - P_P}{\delta x} = Ra\theta_{EB} \sin \alpha,$$

or

$$\Gamma \frac{P_E - P_P}{\delta x} = \theta_{EB} \sin \alpha.$$

The east wall is also adiabatic, so that $\theta_{EB} = \theta_P$, with θ_P the temperature of the adjacent control volume. This leads to the following corrections:

$$a_E = 0, \quad s_P = \sin \alpha(\theta_e - \theta_w)\delta y + \cos \alpha(\theta_n - \theta_s)\delta x - \theta_{EB} \sin \alpha \delta y.$$

The change of sign in the additional source term is related with the sign of the derivatives in the integrated Poisson equation (Equation B.2).

South boundary: Neumann condition, impermeable wall.

$$\frac{\partial P}{\partial \mathbf{n}}\Big|_{South} \simeq \frac{P_P - P_S}{\delta y} = Ra\theta_H \cos \alpha,$$

or

$$\Gamma \frac{P_P - P_S}{\delta y} = \theta_H \cos \alpha.$$

The south wall has specified temperature θ_H. The corrections for the south control volumes are as follows:

$$a_S = 0, \quad s_P = \cos \alpha(\theta_e - \theta_w)\delta y - \sin \alpha(\theta_n - \theta_s)\delta x + \theta_H \cos \alpha \delta x.$$

North boundary: Neumann condition, impermeable wall.

$$\frac{\partial P}{\partial \mathbf{n}}\Big|_{North} \simeq \frac{P_N - P_P}{\delta y} = Ra\theta_C \cos\alpha,$$

or

$$\Gamma \frac{P_N - P_P}{\delta y} = \theta_C \cos\alpha.$$

The north wall has specified temperature θ_C. The corrections for the north control volumes are as follows:

$$a_N = 0, \quad s_P = \cos\alpha(\theta_e - \theta_w)\delta y - \sin\alpha(\theta_n - \theta_s)\delta x - \theta_C \cos\alpha \delta x.$$

Discrete momentum equation for the velocity field

To calculate the velocity field $\mathbf{u}$, second order approximations for the pressure gradient are applied to Equation 2.4:

$$u_e = Ra\theta_e \sin\alpha \frac{P_E - P_P}{\delta x},$$

$$u_w = Ra\theta_w \sin\alpha \frac{P_P - P_W}{\delta x},$$

$$v_n = Ra\theta_n \cos\alpha \frac{P_N - P_P}{\delta y},$$

$$v_s = Ra\theta_s \cos\alpha \frac{P_P - P_S}{\delta y}.$$

Equations 2.11 and 2.12 with the corresponding corrections for the boundary control volumes, as well as the discrete momentum equation constitute the discrete primitive variables problem. Both Equations 2.11 and 2.12 are pentadiagonal matrices that will be solved using the Gauss-Seidel iteration.

2.4 Stream function approach

This approach has been widely applied for the solution of free convection in both porous media and homogeneous fluids (Evans & Raffensperger 1992). A review of early works on free convection in homogeneous fluids is referred to Davis & Jones

(1983). The velocity is given in terms of the stream function, which satisfies mass conservation by definition (Eq. 2.6):

$$\mathbf{u} = \left(\frac{\partial \psi}{\partial y}, -\frac{\partial \psi}{\partial x} \right). \tag{2.13}$$

Using this definition the Laplacian of ψ can be written as:

$$\nabla^2 \psi = -\frac{\partial v}{\partial x} + \frac{\partial u}{\partial y}.$$

Combining with the momentum equation (Eq. 2.4) the pressure term is eliminated

$$\Gamma \nabla^2 \psi = \left(\frac{\partial \theta}{\partial x} \cos\alpha - \frac{\partial \theta}{\partial y} \sin\alpha \right), \tag{2.14}$$

where $\Gamma = -1/Ra$. The mathematical problem is now described by Equations 2.5 and 2.14. The problem can be summarized as follows

$$\begin{cases} \Gamma \nabla^2 \psi = \left(\frac{\partial \theta}{\partial x} \cos\alpha - \frac{\partial \theta}{\partial y} \sin\alpha \right), \\ \frac{\partial \theta}{\partial t} - \nabla^2 \theta + \mathbf{u} \cdot \nabla \theta = 0. \end{cases} \tag{2.15}$$

Considering that $\psi = 0$ at the boundaries satisfies the condition of impermeable walls, the boundary conditions are

$$\begin{aligned} \frac{\partial \theta}{\partial x} = 0, \quad \text{for} \quad x = 0 \quad \text{and} \quad x = D, \\ \theta = 1, \quad \text{for} \quad y = 0 \quad \text{and} \quad t > 0, \\ \theta = 0, \quad \text{for} \quad y = 1 \quad \text{and} \quad t > 0, \\ \psi = 0, \quad \text{for} \quad x = 0 \quad \text{and} \quad x = D, \\ \psi = 0, \quad \text{for} \quad y = 0 \quad \text{and} \quad y = 1. \end{aligned}$$

2.4.1 Fixed point iteration

The time-dependent problem given by the system of Equations 2.15 consists of a Poisson equation for the stream function, ψ, and the advection-diffusion equation for the temperature, θ. This system can be solved iteratively by means of the method of over-relaxation (see for instance Wilkes & Churchill (1966) and Moya et al. (1987)). An alternative approach is the fixed point method, the implementation of this method for the problem of free convection in porous media was reported by Báez & Nicolás (2006) and it was chosen for the numerical model presented here.

Time discretization

In order to implement the fixed point algorithm the heat transfer equation is discretized in time. Here we follow a fully implicit approach, which is a first order approximation and unconditionally stable. This approach has been recommended for general purpose CFD simulations in view of its stability (Versteeg & Malalasekera 1995), small time steps are required however, to avoid high numerical approximation error. Second order approximations such as the Crank-Nicolson scheme involve a considerably more intricate implementation in the fixed point algorithm, with an associated computational cost. For the purposes of obtaining steady-state solutions the fully implicit approach was considered suitable for the model.

It is important to mention that the solution of the steady-state equations, instead of the transient problem, requires a computing time that is comparable to the time-stepping solution. This observation was made after simulation tests developed in this study. A simulation was carried out for the transient problem for only five small time steps, and then the time step was increased taking it as very large, which implies solving the steady-state problem. It was observed that the computing time was comparable to that required to obtain the steady state from a full time-stepping solution. Additionally, the primitive variables approach that was presented in the previous section is a method conceived for time-dependent problems. From these considerations the time-stepping solution was also chosen for the stream function approach.

Applying the integral $\int_t^{t+\Delta t} dt$ to the heat transfer equation turns out

$$\theta^{t+\Delta t} - \theta^t - \int_t^{t+\Delta t} \nabla^2\theta dt + \int_t^{t+\Delta t} (\mathbf{u}\cdot\nabla\theta) dt = 0,$$

and then applying the fully implicit criterion the variables in the diffusive and convective terms are taken at the new time step $t + \Delta t$ so that we can approximate the integrals as follows

$$\theta^{t+\Delta t} - \theta^t - \nabla^2\theta^{t+\Delta t}\Delta t + (\mathbf{u}^{t+\Delta t}\cdot\nabla\theta^{t+\Delta t})\Delta t = 0.$$

Renaming the subscripts as $\theta = \theta^{t+\Delta t}$ for the new time step and $\theta^0 = \theta^t$ for the old time step and dividing by Δt, the heat transfer equation discretized in time can be written as

$$\frac{\theta - \theta^0}{\Delta t} - \nabla^2\theta + \mathbf{u}\cdot\nabla\theta = 0.$$

We can call this equation $\Upsilon(\theta, \psi)$ and rewrite in the following form

$$\Upsilon(\theta,\psi) = \frac{1}{\Delta t}\theta - \nabla^2\theta + \mathbf{u}\cdot\nabla\theta - \frac{1}{\Delta t}\theta^0. \tag{2.16}$$

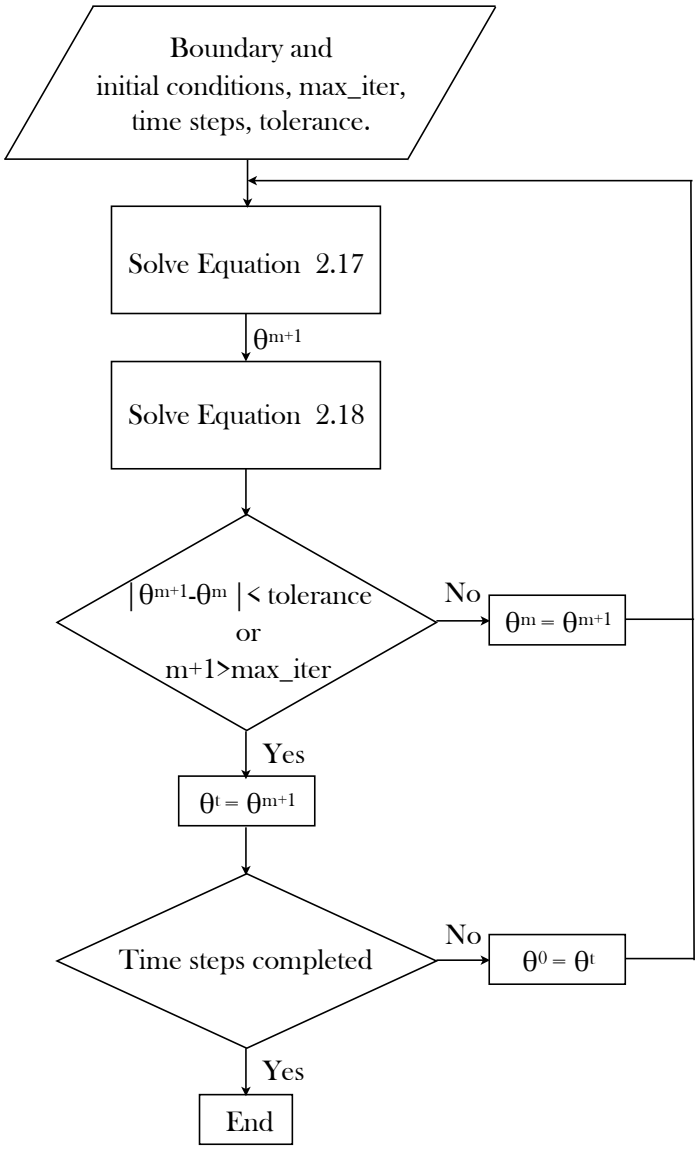

Figure 2.4: Fixed point iterative algorithm to solve the system of Equations 2.17-2.18 with the corresponding boundary conditions.

The fixed point iteration assumes that the linear terms of this equation $\frac{1}{\Delta t}\theta - \nabla^2\theta$ at an iteration $m+1$ are equal to the linear terms at the iteration m minus a correction $\lambda\Upsilon(\theta^m, \psi^m)$, with $0 < \lambda < 1$. Defining an operator $L = (\frac{1}{\Delta t} - \nabla^2)$ to simplify notation, the system of Equations 2.15 subject to the boundary and initial conditions referred above can be written as follows

$$L\theta^{m+1} = L\theta^m - \lambda\Upsilon(\theta^m, \psi^m), \tag{2.17}$$

$$\Gamma\nabla^2\psi^{m+1} = \left(\frac{\partial\theta^{m+1}}{\partial x}\cos\alpha - \frac{\partial\theta^{m+1}}{\partial y}\sin\alpha\right). \tag{2.18}$$

This system can be solved iteratively and it converges when the term $\lambda\Upsilon(\theta^m, \psi^m)$ tends to zero. In this form we have a system of linear differential equations since

the right-hand side of Equation 2.17 containing the convective term is known and becomes a source term in this equation. Figure 2.4 shows a flow chart of the iterative process.

2.4.2 Discrete problem

The mathematical problem given by Equations 2.17 and 2.18 was also discretized following the Finite Volume numerical method. A staggered grid was defined to calculate the scalars θ and ψ as shown in Figure 2.5, the velocities are calculated on the faces of the temperature control volume, whereas ψ is calculated on the corners of the temperature control volume, uniform mesh is assumed in what follows.

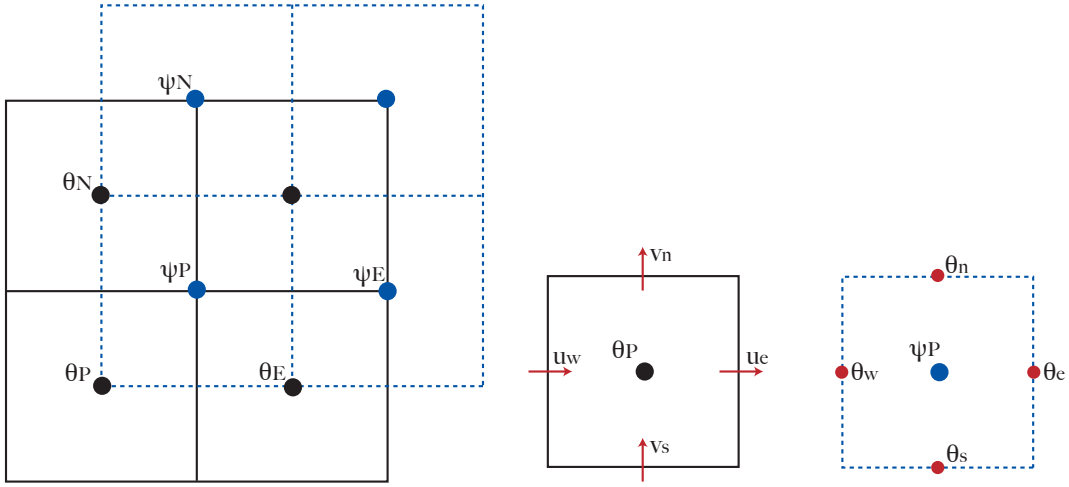

Figure 2.5: Staggered grid for the estimation of u_e, u_w, v_n, v_s, θ_e, θ_w, θ_n, and θ_s. The continuous line represents temperature control volume and dashed line represents stream function control volume.

Discrete heat transfer equation: integration of the terms $L\theta^{m+1}$ and $L\theta^{m}$

The integration of the heat transfer equation (Eq. 2.17) in the temperature control volume was carried out using a central differencing scheme for the convective term, which is a second order approximation. The integration of the term $L\theta^{m+1}$ of Equation 2.17 excluding boundary control volumes turns out

$$\int_{CV} L\theta^{m+1} dV \simeq a_P\theta_P^{m+1} - a_E\theta_E^{m+1} - a_W\theta_W^{m+1} - a_N\theta_N^{m+1} - a_S\theta_S^{m+1}, \tag{2.19}$$

with

$$a_E = \frac{A_e}{\delta x}, \quad a_W = \frac{A_w}{\delta x}, \quad a_N = \frac{A_n}{\delta y}, \quad a_S = \frac{A_s}{\delta y},$$

and

$$a_P = a_E + a_W + a_N + a_S + \frac{\Delta V}{\Delta t},$$

with $\Delta V = \delta x \delta y$. Additionally, since we are dealing with uniform meshes, the areas of the faces are constants $A_e = A_w = A_n = A_s = \delta x = \delta y$. Likewise, the integration of the term $L\theta^m$ of the equation is

$$\int_{CV} L\theta^m dV \simeq a_P\theta_P^m - a_E\theta_E^m - a_W\theta_W^m - a_N\theta_N^m - a_S\theta_S^m, \tag{2.20}$$

with the same values for the coefficients a_E, a_W, a_N, a_S, and a_P as those for Equation 2.19.

Boundary control volumes

The following considerations are made for boundary control volumes (BCV) (Versteeg & Malalasekera 1995). Equivalent corrections to the coefficients apply for both $\int_{BCV} L\theta^m dV$ and $\int_{BCV} L\theta^{m+1} dV$:

West boundary: Neumann condition, adiabatic wall.

$$a_W = 0$$

East boundary: Neumann condition, adiabatic wall.

$$a_E = 0$$

South boundary: Dirichlet condition, $\theta = \theta_H$.

$$\int_{BCV} L\theta^{m+1} dV \simeq a_P\theta_P^{m+1} - a_E\theta_E^{m+1} - a_W\theta_W^{m+1} - a_N\theta_N^{m+1} - 2a_S\theta_H,$$

$$a_P = a_E + a_W + a_N + 2a_S + \frac{\Delta V}{\Delta t}.$$

North boundary: Dirichlet condition, $\theta = \theta_C$.

$$\int_{BCV} L\theta^{m+1} dV \simeq a_P\theta_P^{m+1} - a_E\theta_E^{m+1} - a_W\theta_W^{m+1} - a_S\theta_S^{m+1} - 2a_N\theta_C,$$

$$a_P = a_E + a_W + 2a_N + a_S + \frac{\Delta V}{\Delta t}.$$

Discrete heat transfer equation: Integration of the term $\Upsilon(\theta^m, \psi^m)$

Finally, the integration of the term $\Upsilon(\theta^m, \psi^m)$ turns out

$$\int_{CV} \Upsilon(\theta^m, \psi^m) dV \simeq b_P\theta_P^m - b_E\theta_E^m - b_W\theta_W^m - b_N\theta_N^m - b_S\theta_S^m + s_P, \tag{2.21}$$

with

$$b_E = \frac{A_e}{\delta x} - \frac{u_e^m A_e}{2}, \quad b_W = \frac{A_w}{\delta x} + \frac{u_w^m A_w}{2},$$

$$b_N = \frac{A_n}{\delta y} - \frac{v_n^m A_n}{2}, \quad b_S = \frac{A_s}{\delta y} + \frac{v_s^m A_s}{2},$$

$$b_P = b_E + b_W + b_N + b_S + \frac{\Delta V}{\Delta t}, \quad s_P = -\theta^0 \frac{\Delta V}{\Delta t},$$

and

$$u_e^m = \left(\frac{\partial \psi^m}{\partial y}\right)_e, \quad u_w^m = \left(\frac{\partial \psi^m}{\partial y}\right)_w, \quad v_n^m = \left(-\frac{\partial \psi^m}{\partial x}\right)_n, \quad v_s^m = \left(-\frac{\partial \psi^m}{\partial x}\right)_s.$$

These expressions for the velocity justify the choice of a staggered grid to discretize the equations. As shown in Figure 2.5 the velocities are required on the faces of the temperature control volume so that having the stream function on the corners permits a straightforward approximation of the derivatives of ψ at the location of u_e, u_w, v_n, and v_s, this can be done with a second order approximation.

Boundary control volumes

West boundary: Neumann condition, adiabatic wall with impermeable boundary ($\psi_{bound.} = 0$).

$$b_W = 0$$

East boundary: Neumann condition, adiabatic wall with impermeable boundary ($\psi_{bound.} = 0$).

$$b_E = 0$$

South boundary: Dirichlet condition, $\theta = \theta_H$.

$$\int_{BCV} \Upsilon(\theta^m, \psi^m) dV \simeq b_P \theta_P^m - b_E \theta_E^m - b_W \theta_W^m - b_N \theta_N^m - 2 b_S \theta_H + s_P,$$

$$b_P = b_E + b_W + b_N + 2 b_S + \frac{\Delta V}{\Delta t}.$$

North boundary: Dirichlet condition, $\theta = \theta_C$.

$$\int_{BCV} \Upsilon(\theta^m, \psi^m) dV \simeq b_P \theta_P^{m+1} - b_E \theta_E^{m+1} - b_W \theta_W^{m+1} - b_S \theta_S^{m+1} - 2 b_N \theta_C,$$

$$b_P = b_E + b_W + 2 b_N + b_S + \frac{\Delta V}{\Delta t}.$$

Gathering Equations 2.19, 2.20, and 2.21 and taking into account the corrections to the boundary control volumes a pentadiagonal system of equations is obtained of the form:

$$\begin{aligned} &a_P\theta_P^{m+1} - a_E\theta_E^{m+1} - a_W\theta_W^{m+1} - a_N\theta_N^{m+1} - a_S\theta_S^{m+1} = \\ &a_P\theta_P^{m} - a_E\theta_E^{m} - a_W\theta_W^{m} - a_N\theta_N^{m} - a_S\theta_S^{m} \\ &- \lambda(b_P\theta_P^{m} - b_E\theta_E^{m} - b_W\theta_W^{m} - b_N\theta_N^{m} - b_S\theta_S^{m} + s_P). \end{aligned} \tag{2.22}$$

Momentum equation

The discretized form of the momentum equation at the iteration $m+1$ (Eq. 2.18) is

$$a_P\psi_P^{m+1} = a_E\psi_E^{m+1} + a_W\psi_W^{m+1} + a_N\psi_N^{m+1} + a_S\psi_S^{m+1} - s_P, \tag{2.23}$$

with

$$a_E = \frac{\Gamma_e A_e}{\delta x}, \quad a_W = \frac{\Gamma_w A_w}{\delta x}, \quad a_N = \frac{\Gamma_n A_n}{\delta y}, \quad a_S = \frac{\Gamma_s A_s}{\delta y},$$

again, the terms $\Gamma_e = \Gamma_w = \Gamma_n = \Gamma_s = \Gamma = -1/Ra$

$$a_P = a_E + a_W + a_N + a_S.$$

The source term s_P (buoyancy term) is obtained as follows

$$\begin{aligned} s_P &= \int_s^n \int_w^e \left(\frac{\partial\theta^{m+1}}{\partial x}\cos\alpha - \frac{\partial\theta^{m+1}}{\partial y}\sin\alpha \right) dxdy = \\ &\int_s^n \cos\alpha(\theta_e^{m+1} - \theta_w^{m+1})dy - \int_w^e \sin\alpha(\theta_n^{m+1} - \theta_s^{m+1})dx \\ &= \cos\alpha(\theta_e^{m+1} - \theta_w^{m+1})\delta y - \sin\alpha(\theta_n^{m+1} - \theta_s^{m+1})\delta x, \end{aligned}$$

with θ_e^{m+1}, θ_w^{m+1}, θ_n^{m+1}, and θ_s^{m+1} calculated at the positions shown in Figure 2.5.

Boundary control volumes

For the momentum equation all the boundary conditions are of type Dirichlet $\psi_{bound} = 0$.

West boundary:

$$a_W = 0$$

East boundary:

$$a_E = 0$$

South boundary:

$$a_S = 0$$

North boundary:

$$a_N = 0$$

Equations 2.22 and 2.23 represent the discretized energy and momentum equations, respectively. These are pentadiagonal algebraic systems that can be solved by iterative methods.

2.5 Numerical results

2.5.1 Validation

Both the primitive variables and the stream function algorithms were implemented in Fortran 90 and the simulations were carried out on a PC based on Ubuntu 14.04 with a processor Intel Core i7. A comparison between the Three-diagonal Matrix Algorithm with alternating directions and the Gauss-Seidel iteration was carried out. The latter method proved to be a faster solution, for this reason all the simulations were based on this method. There are other available algorithms such as SOR, Multigrid, and Minimal Residual Methods (GMRES). A comparison of these algorithms with the Gauss-Seidel iteration was not considered necessary in this study, since this method permitted to obtain solutions in computing times short enough to justify the implementation and comparison of other methods. Nevertheless, these alternative algorithms can potentially speed up the numerical solutions, which would be important when handling high resolution grids.

Steady-state solutions were obtained from the evaluation of the convergence of the temperature matrix. The infinity norm of the difference $L_\infty = |\boldsymbol{\theta}^t - \boldsymbol{\theta}^{t-1}|_\infty$ was calculated for successive time steps over a long time interval that proved to be long enough after several tests (2.2×10^4 time steps in this case). The convergence criterion was defined according to the condition $\langle L_\infty \rangle_{t_{int}} < 5 \times 10^{-7}$, where $\langle L_\infty \rangle_{t_{int}}$ is the average infinity norm over the time interval t_{int}.

A local Nusselt number (Nu_l) was defined (Eq. 2.24) to quantify the convective heat transfer throughout the porous enclosure. It is important to notice that given the boundary conditions for the heat transfer equation (Section 2.2.1), a purely conductive steady-state solution in the cavity leads to a linear thermal profile of the form $\theta(x, y) = y - 1$, that has a derivative with respect to y equal 1. This implies that a in convective steady-state solution $Nu > 1$.

$$Nu_l = \left| \frac{\partial \theta}{\partial y} \right|_{y=0}. \tag{2.24}$$

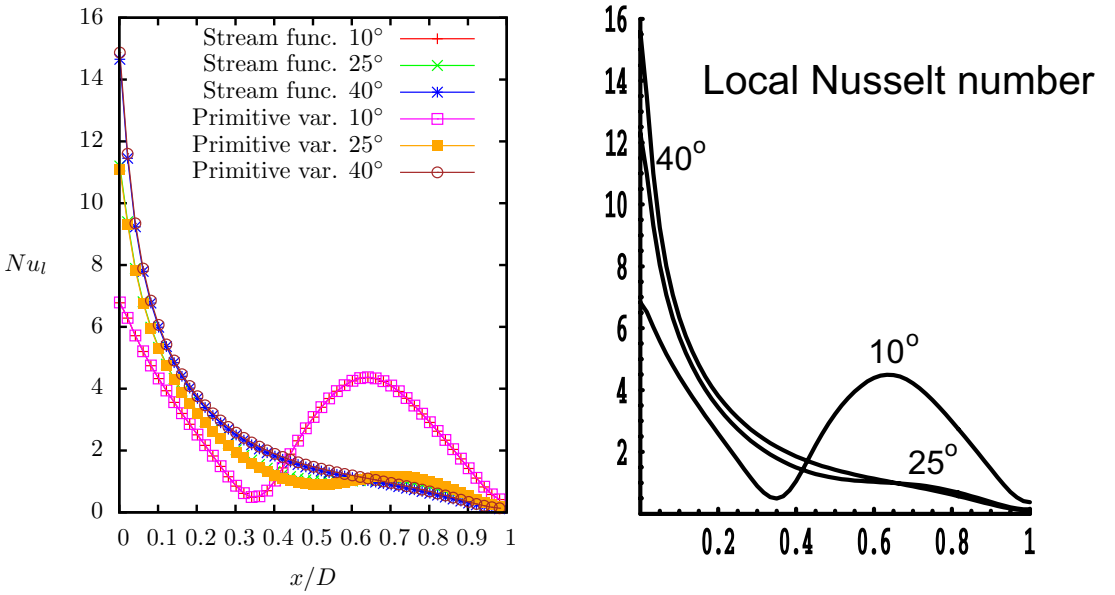

Figure 2.6: Comparison of the local Nusselt number between the simulation results obtained with the models presented in this work (left) and the results reported by Báez & Nicolás (2006) (right), which are based on the stream function approach. The x axis was normalized dividing by 3, so that $x \in (0, 1)$. This figure shows a good agreement between the three numerical models.

A model of aspect ratio $D = 3$ was considered for the validation of the model with a constant Rayleigh number $Ra = 100$. Three slope angles were analyzed: 10°, 25° and 40°. After a calibration process a time step $\Delta t = 2.0 \times 10^{-4}$ was chosen for the simulations. Likewise, a uniform mesh consisting of $\Delta x = \Delta y = 100^{-1}$ was employed for the spatial discretization. A mesh dependency study showed that a mesh consisting of $\Delta x = \Delta y = 25^{-1}$ leads to equivalent results with a difference of 0.48% in the global Nusselt number (Section 2.5.2).

The local Nusselt number for the three angles studied here are shown in Figure 2.6. This figure shows that the two numerical models developed in this work are in good agreement with each other. Particularly, the local Nusselt number for $\alpha = 10°$ presents a perfect match between the two models. The Nusselt number for $\alpha = 25°$ and $\alpha = 40°$ displays very small differences between the stream function and primitive variables models. Similarly, the models show a good agreement with the results reported by Báez & Nicolás (2006), which are based on the stream function approach.

Figure 2.7 shows the temperature and velocity fields of the three angles analyzed. Figure 2.8 shows the streamlines and isotherms calculated from the results of the primitive variables model. The streamlines were calculated invoking the vorticity and stream function definition: $\omega = \nabla \times \mathbf{u}$ and $\nabla^2 \psi = -\omega$, so that another Poisson equation was solved numerically assuming that the stream function is zero at the boundary of the porous enclosure $\psi|_\Omega = 0$. The transition from multiple convective cells to a single cell is shown as the angle of inclination is increased.

The highest Nusselt number occurs close to $x = 0$ in the three cases analyzed. This is due to the cold fluid that comes from the upper part of the cavity and flows down at this point absorbing heat. Two maxima and two minima can be observed for $\alpha = 10°$. The convective mode at this angle comprises three convective cells (Figs. 2.7 and 2.8), which implies that there are two downwellings and two upwellings. The temperature distribution for $\alpha = 10°$ shows clearly the presence of two thermal plumes that correspond with the two maxima in the local Nusselt number (Fig. 2.6).

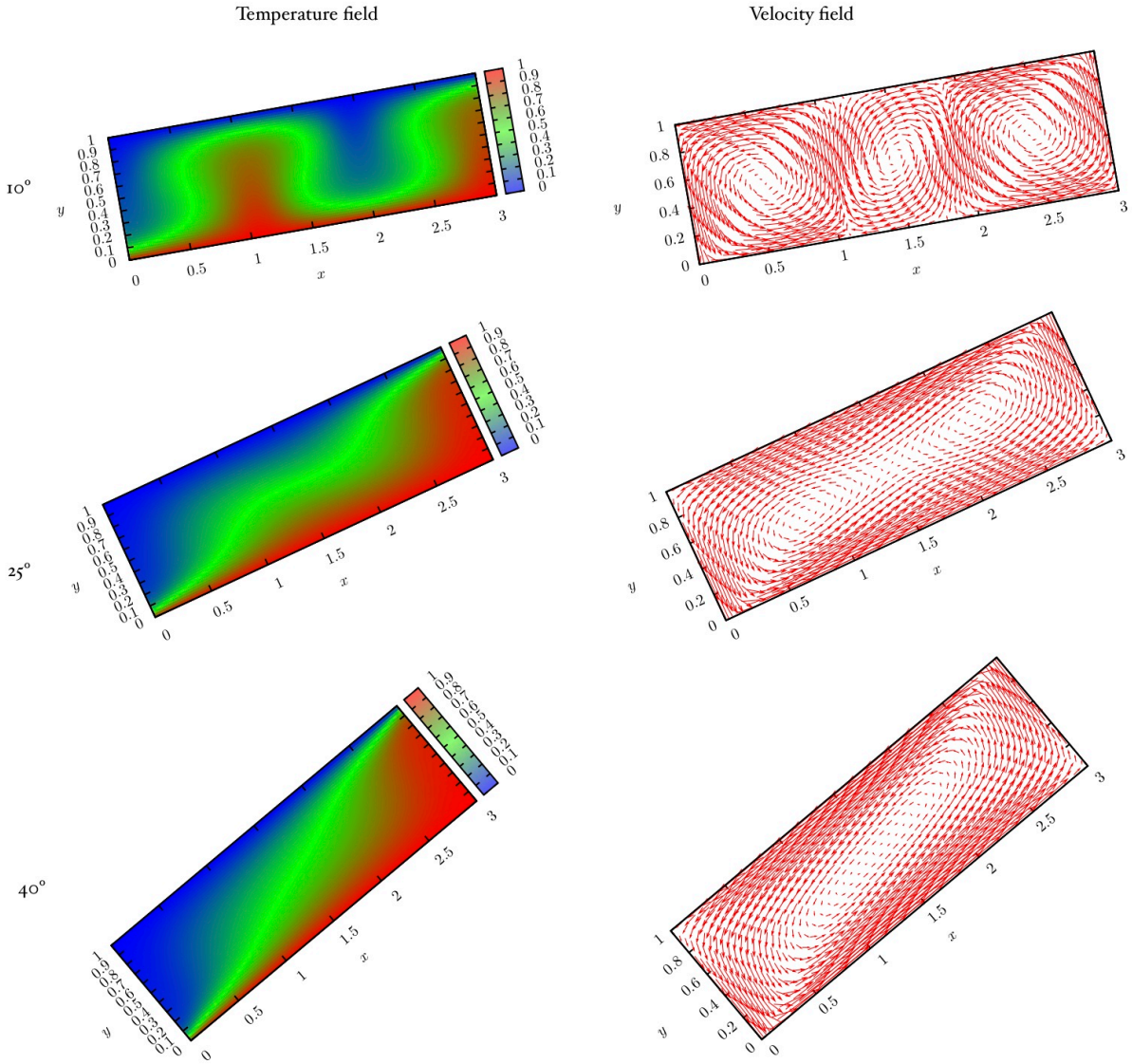

Figure 2.7: Steady-state temperature and velocity fields of free convection in a sloping porous enclosure obtained from the primitive variables model for three slope angles.

As the inclination is increased the component of the gravity on the x-axis becomes more important, increasing buoyancy forces in this direction. This causes a transition from multiple cell regime to single cell convection. At $\alpha = 25°$ the steady-state solution is characterized by a single cell with two internal secondary cells (Fig. 2.8).

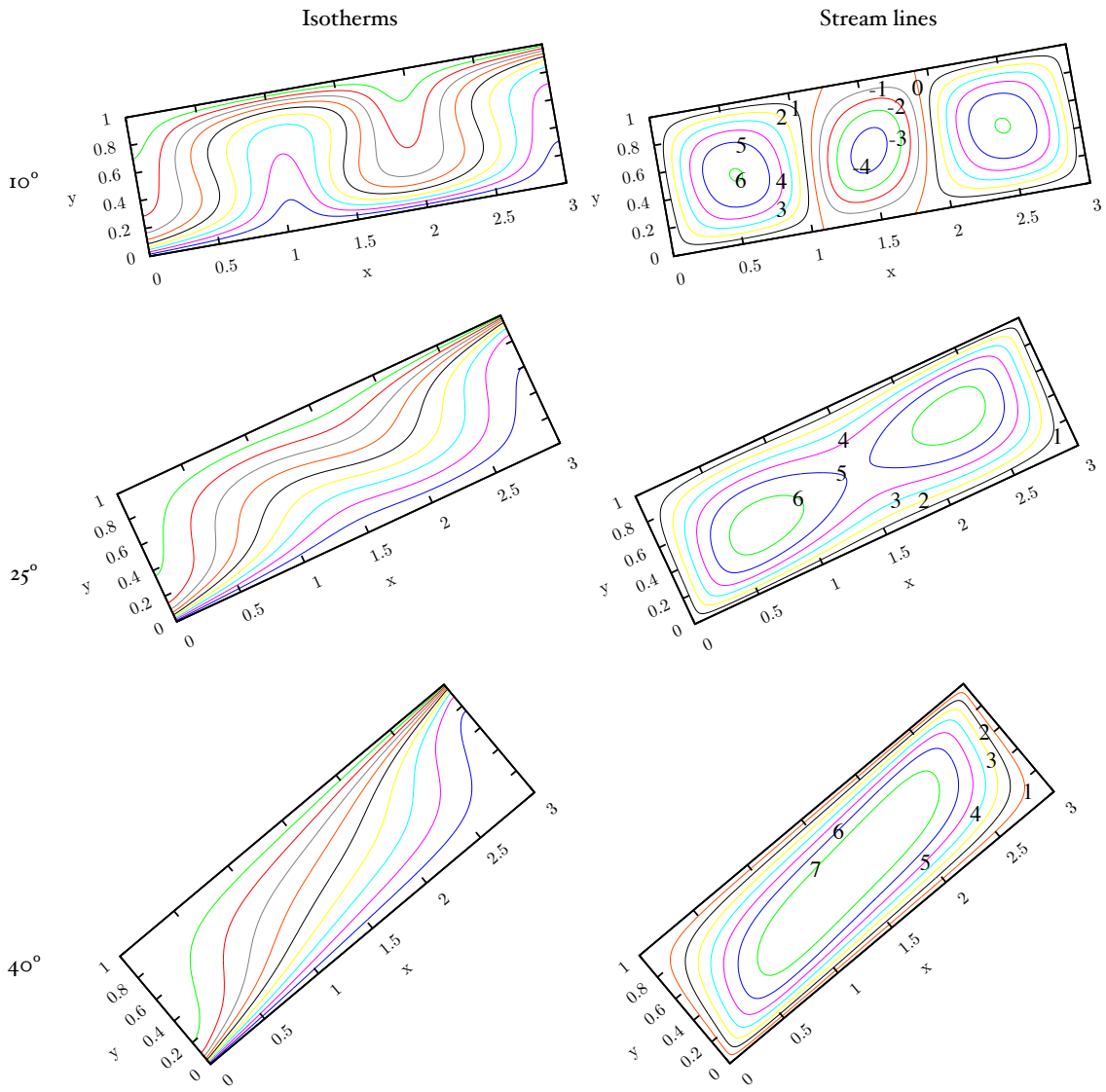

Figure 2.8: Isotherms and streamlines for three slope angles. Three convective modes can be identified: multicellular, for $\alpha = 10°$; single cell with two internal cells, for $\alpha = 25°$; and single cell, for $\alpha = 40°$.

Table 2.1: Global Nusselt numbers and computing time for the steady-state solution of free convection in a 2D sloping porous enclosure. The two numerical models proposed in this work show good agreement with the results reported by Báez & Nicolás (2006).

	Stream function		Primitive variables		Báez & Nicolás (2006)
α	Nu	t_{cpu} (sec)	Nu	t_{cpu} (sec)	Nu
10°	8.37	5.0	8.38	14.0	8.60
25°	6.37	2.8	6.38	14.0	6.75
40°	7.33	1.66	7.34	12.0	7.65

A further increase in α leads to a single cell convection.

In order to compare the overall convective heat transfer in the enclosures a global Nusselt number is defined as follows:

$$Nu = \int \left| \frac{\partial \theta}{\partial y} \right|_{y=0} dx. \tag{2.25}$$

Table 2.1 shows a comparison of the global Nusselt number between the models developed here and the results reported by Báez & Nicolás (2006). The results are in general in agreement. The small difference in Nu between our results and those reported by the authors can be associated with the different mesh size and time step employed. The referred authors employed a mesh defined by $\Delta x = 60^{-1}$, $\Delta y = 40^{-1}$ and a larger time step $\Delta t = 2 \times 10^{-3}$, so that the convergence criterion might not lead to exactly the same result. A systematic underestimation can be observed in the comparison in Table 2.1, the highest difference (5.8%) being associated with $\alpha = 25°$. The table also shows the computing time t_{cpu} required for the simulations, the stream function approach despite being based on an iterative solution proved faster simulations than the primitive variables model.

An additional comparison of the primitive variables model presented here was carried out with the results reported by Baytaş (2000), who studied the problem with a model based on the stream function approach. This author analyzed an analogous problem to that described in Section 2.2. In this case however, the aspect ratio was defined as a square porous cavity and the boundary conditions were defined as illustrated in Figure 2.9.

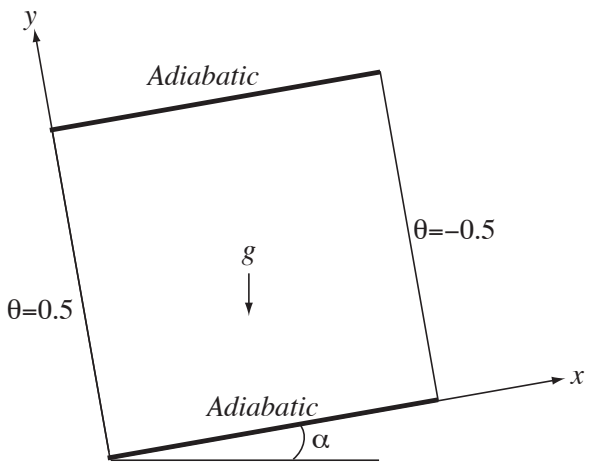

Figure 2.9: Schematic model of a porous enclosure heated from one of its sides and cooled from the opposite side and adiabatic boundaries as presented by Baytaş (2000).

The numerical results turned out in good agreement with those reported in the referred work. Figure 2.10 shows the local Nusselt number calculated at several angles

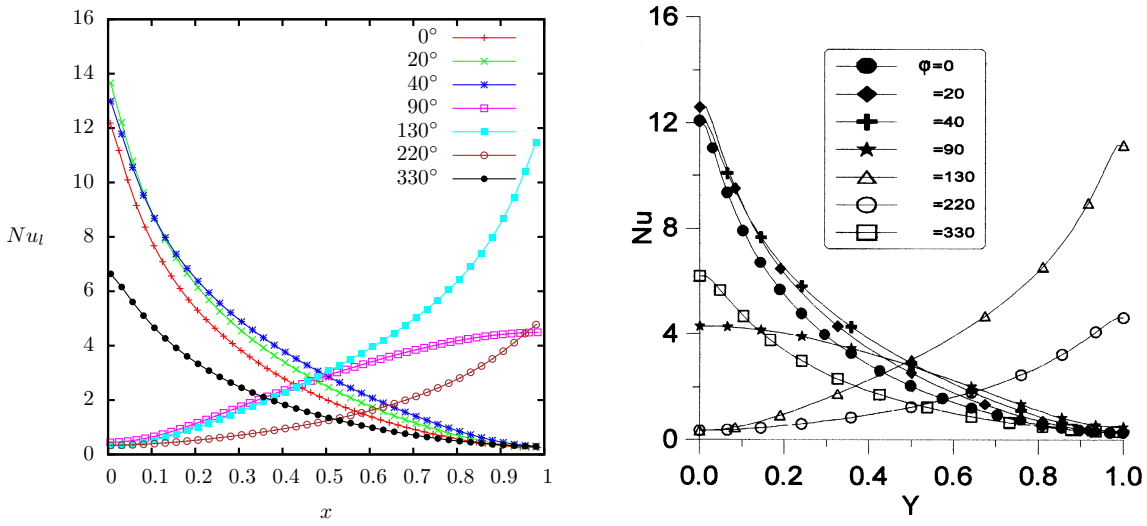

Figure 2.10: Comparison of Nu_l between the results obtained with the primitive variables model (left) and the results reported by Baytaş (2000) (right).

α. For $\alpha = 90°$ the resulting local Nusselt number curve was inverted which means that the direction of rotation of the convective cell was the opposite. This behavior can be attributed to the fact that $\alpha = 90°$ is equivalent to the horizontal porous layer heated from below and multiplicity of solutions can happen, nonetheless the magnitude of Nu_l was consistent.

2.5.2 Parametric study

A parametric study was carried out to determine the relation between the Nusselt number and the slope angle of the enclosure. All the simulations were carried out with the stream function model on the basis that it is a faster computational solution. A mesh study was conducted to determine the sensitivity of the result to the mesh size. The model of reference was that presented in Table 2.1 for $D = 3$, $Ra = 100$ and $\alpha = 10°$ for which $Nu = 8.37$ was obtained. From these model parameters a Nusselt number $Nu = 8.36$ was obtained from a uniform mesh $\Delta x = \Delta y = 50^{-1}$, which is very close (0.12% difference) to the result obtained with a fine mesh. Likewise, a Nusselt number $Nu = 8.33$ was obtained using a coarse mesh $\Delta x = \Delta y = 25^{-1}$ representing a difference of 0.48%. From these results, a mesh $\Delta x = \Delta y = 50^{-1}$ was employed for the aspect ratio $D = 3$, $\Delta x = \Delta y = 40^{-1}$ for $D = 5$, and $\Delta x = \Delta y = 25^{-1}$ for $D = 10$. The time step was kept as in the validation presented before, $\Delta t = 2.0 \times 10^{-4}$.

The parametric study presented here aims to provide the followings. First, it gives an overall view of the Nusselt number as a function of the governing parameters of the system. Second, it puts forward a high-resolution view of the evolution of the convective modes that are possible in 2D. The former study was conceived for comparison with 3D analysis, and the latter to provide a wider background on the

problem of free convection in a sloping porous enclosure.

The results in this section are presented as follows. Firstly, the overall view of the Nusselt number as a function of the slope angle is analyzed for five Rayleigh numbers considering the initial condition defined in the problem formulation (Section 2.2). Subsequently, a high-resolution parametric study is presented for $Ra = 70$ and $Ra = 100$ using suitable initial conditions. This is to determine the number of convective cells that can constitute a multicellular steady-state solution, as well as the slope angles at which they appear. This high-resolution parametric study cannot be carried out in 3D with the available computational facilities in a reasonable time. Therefore, these results serve as a background to interpret more accurately the 3D studies of the problem.

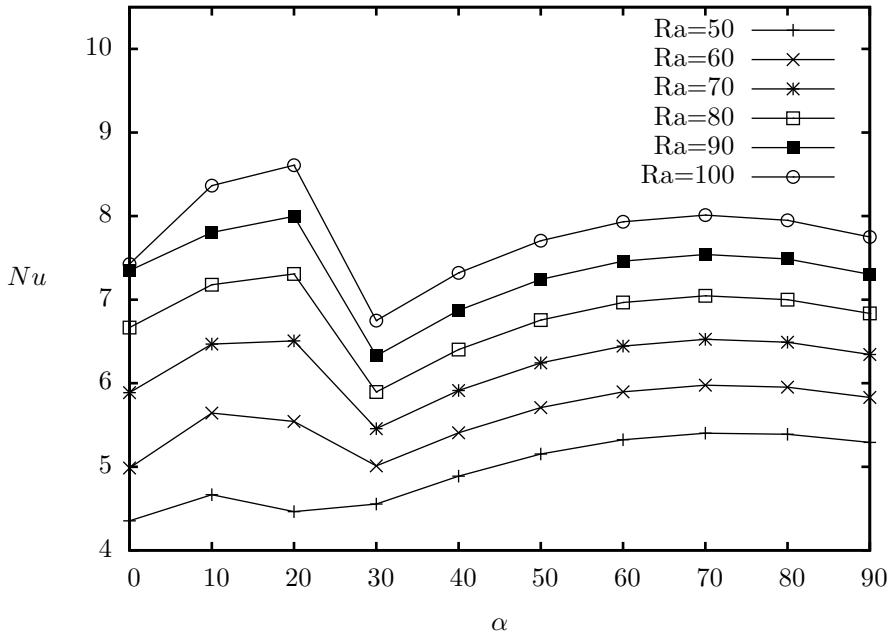

Figure 2.11: Steady state Nusselt number vs slope angle for a 2D porous enclosure with aspect ratio $D = 3$.

Overall behavior for aspect ratio $D = 3$

Moderate Rayleigh numbers were considered between 50 and 100 and ten slope angles between 0 and 90°. Figure 2.11 shows the Nusselt number as a function of the slope angle α. Two trends can be distinguished, the first one between 0 and 30°, and the second one from 30° onwards. As shown in Figure 2.12 the convective modes between 0 and 20° are multicellular. There is in general a drop in Nu between 20 and 30° (the exception is $Ra = 50$ that presents a slight increase) where the system transits to a single cell regime. Table 2.2 shows the local Nusselt maxima, two local maxima can be identified in the two intervals referred above. For the multicellular regime

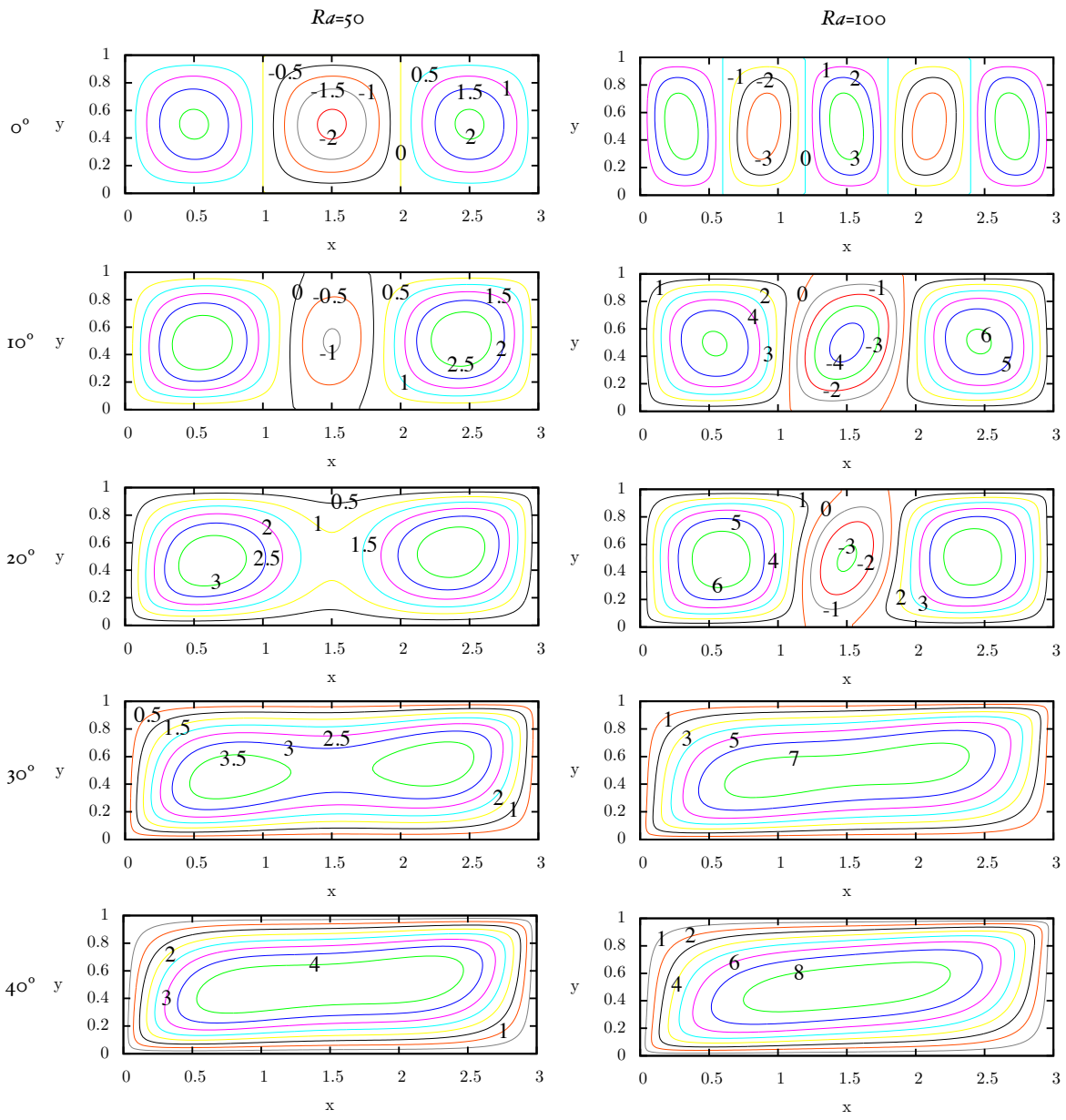

Figure 2.12: Streamlines for a porous enclosure with $D = 3$, for $Ra = 50$ and $Ra = 100$ showing the transition from multicellular flow to single cell convection.

the local maximum is located at 10° for low Ra and 20° for higher Ra, on the other hand, for the single cell regime the local maximum is located at $\alpha = 70°$ for all the Rayleigh numbers analyzed. We can observe that for low Rayleigh numbers (up to $Ra = 70$), the absolute maximum corresponds to the single cell convection, and from $Ra = 80$ the maximum corresponds to multicellular convection. This means that the multiplication of upwellings enhances the heat transfer as long as the Rayleigh number is high.

As it has been reported before (Moya et al. 1987, Báez & Nicolás 2006), a horizontal porous enclosure heated from below ($\alpha = 0$) displays multicellular convection. In the results presented here this convective mode comprised between three and five

Table 2.2: Local Nusselt maxima for a 2D porous enclosure with aspect ratio $D = 3$. The angle α at which the maximum is located is given beside each local maximum.

	Local Nu maximum	
Ra	$0° \leq \alpha \leq 30°$	$30° < \alpha \leq 90°$
50	4.66 ($\alpha = 10°$)	5.40 ($\alpha = 70°$)
60	5.64 ($\alpha = 10°$)	5.97 ($\alpha = 70°$)
70	6.50 ($\alpha = 20°$)	6.52 ($\alpha = 70°$)
80	7.30 ($\alpha = 20°$)	7.04 ($\alpha = 70°$)
90	7.99 ($\alpha = 20°$)	7.54 ($\alpha = 70°$)
100	8.60 ($\alpha = 20°$)	8.01 ($\alpha = 70°$)

convective cells, with an increasing number of cells as Ra increases, as predicted by Straus (1974). It can be seen that for the horizontal cavity ($\alpha = 0$) the Nusselt number for $Ra = 100$ turned out slightly higher than that for Ra =90. These solutions are characterized by five and four convective cells, respectively. In order to confirm this result, a new simulation was carried out for Ra =100 using a very long simulation time instead of the convergence criterion, the result was confirmed. This behavior is consistent with the results presented by De La Torre Juárez & Busse (1995) who showed that increasing the Rayleigh number in the horizontal cavity and the number of cells of the system does not necessarily imply an increase in Nu.

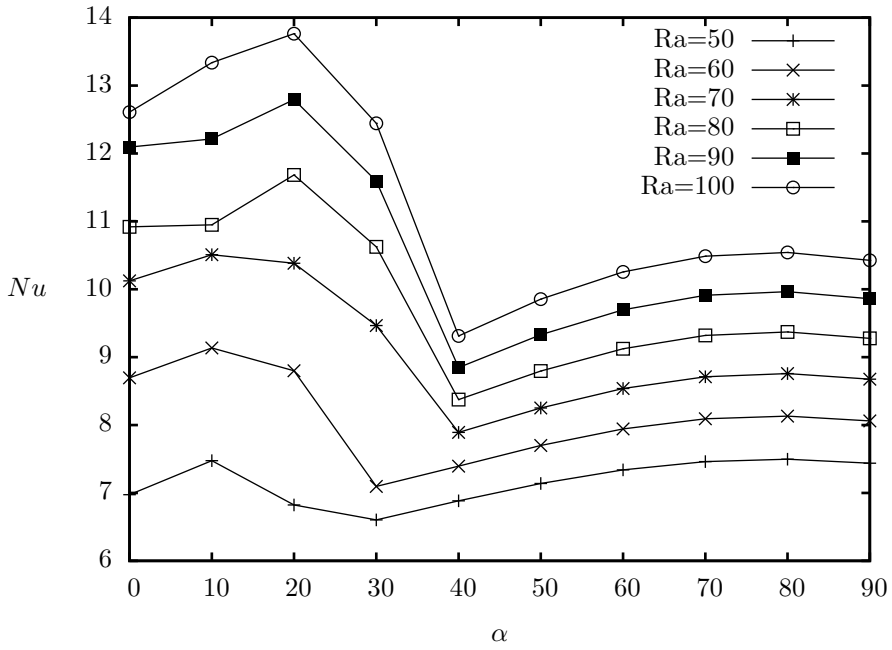

Figure 2.13: Steady state Nusselt number vs slope angle for a 2D porous enclosure with aspect ratio $D = 5$.

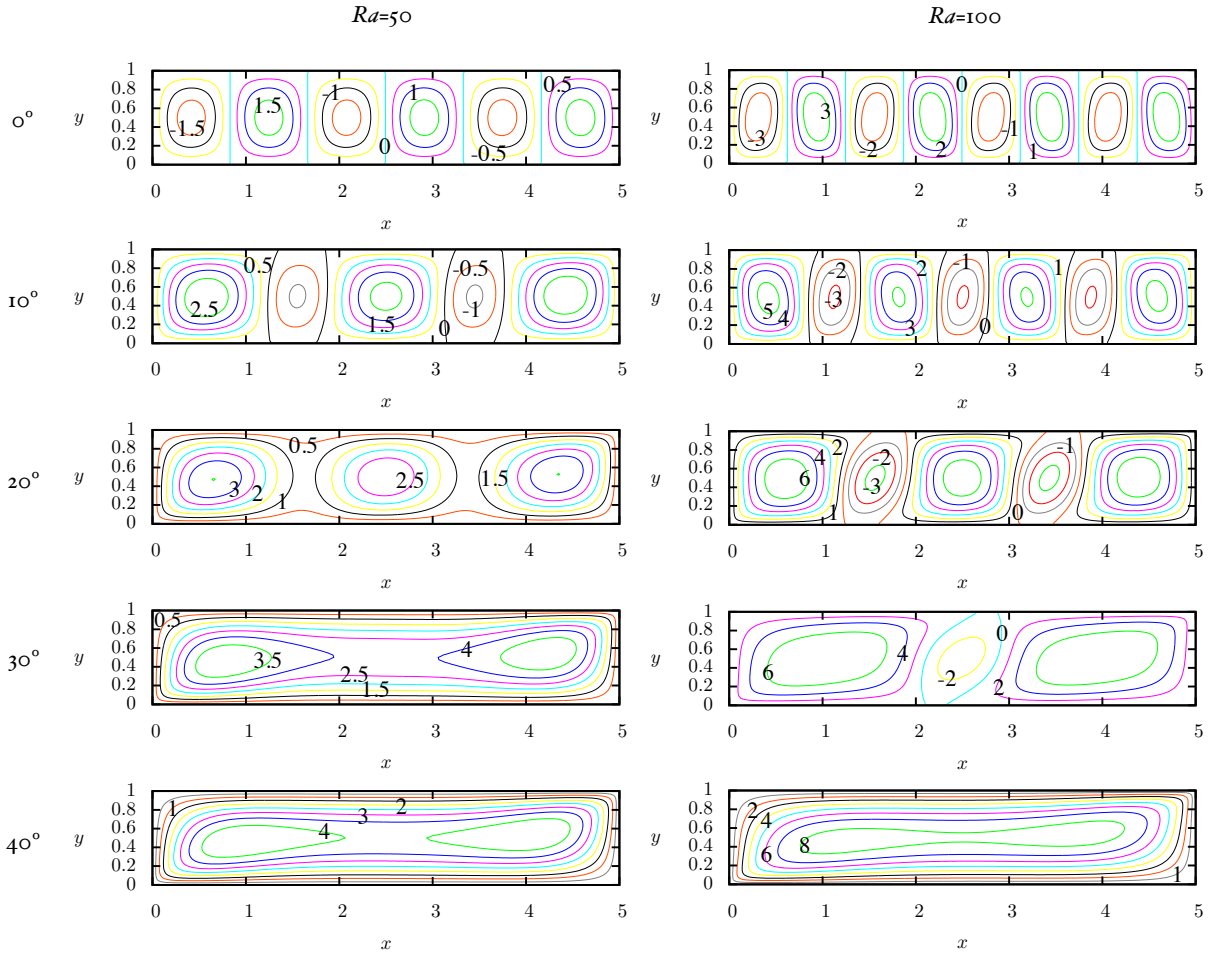

Figure 2.14: Streamlines for a porous enclosure with $D = 5$, for $Ra = 50$ and $Ra = 100$ showing the transition from multicellular flow to single cell convection.

Overall behavior for aspect ratios $D = 5$ and $D = 10$

Figure 2.13 shows the Nusselt number as a function of the slope angle for a porous enclosure of aspect ratio $D = 5$. Figure 2.14 shows streamlines for the first five slope angles and two Rayleigh numbers. The relation between Nu and α shows again

Table 2.3: Local Nusselt maxima for a 2D porous enclosure with aspect ratio $D = 5$. The angle α at which the maximum is located is given beside each local maximum.

	Local Nu maximum	
Ra	$0° \leq \alpha \leq 30°$	$30° < \alpha \leq 90°$
50	7.47 ($\alpha = 10°$)	7.49 ($\alpha = 80°$)
60	9.13 ($\alpha = 10°$)	8.13 ($\alpha = 80°$)
70	10.50 ($\alpha = 10°$)	8.75 ($\alpha = 80°$)
80	11.68 ($\alpha = 20°$)	9.37 ($\alpha = 80°$)
90	12.79 ($\alpha = 20°$)	9.96 ($\alpha = 80°$)
100	13.76 ($\alpha = 20°$)	10.54 ($\alpha = 80°$)

two trends or curves corresponding to multicelluar and single cell convection. The angle of transition between these two curves is $\alpha = 30°$ for $Ra = 50$ and $Ra = 60$ and $\alpha = 40°$ for higher Rayleigh number. This is consistent with the fact that the multicellular convection is favored by high Rayleigh numbers so that the transition to single cell convection occurs for higher α. For the horizontal case $\alpha = 0$ the multicellular convection comprised between 6 and 8 convective cells. Table 2.3 shows the local maxima for this aspect ratio, which are located at $\alpha = 10°$ and $\alpha = 20°$ for the multicellular regime and at $\alpha = 80°$ for the single cell regime.

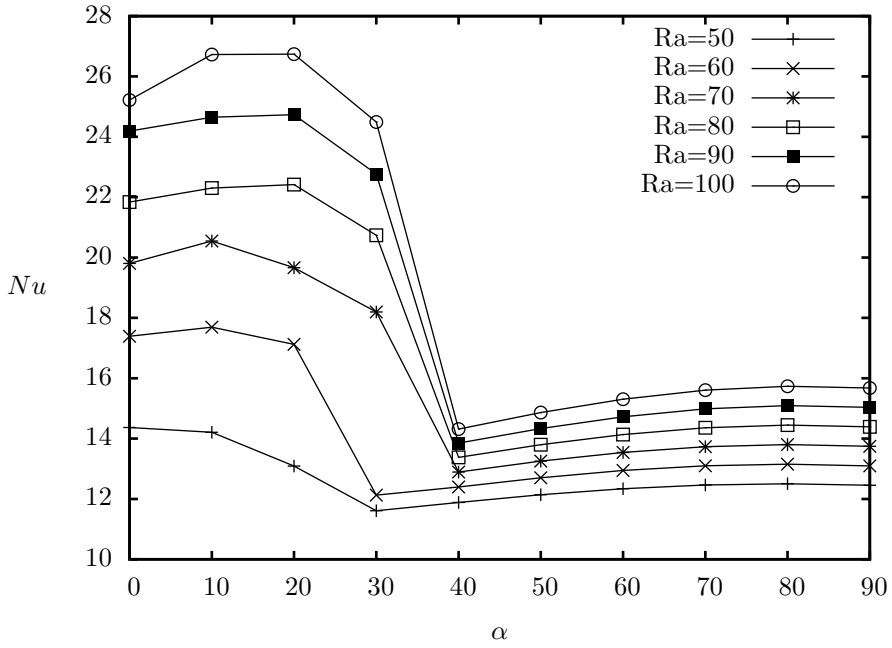

Figure 2.15: Steady state Nusselt number vs slope angle for a 2D porous enclosure with aspect ratio $D = 10$.

Table 2.4: Local Nusselt maxima for a 2D porous enclosure with aspect ratio $D = 10$. The angle α at which the maximum is located is given beside each local maximum.

	Local Nu maximum	
Ra	$0° \leq \alpha \leq 30°$	$30° < \alpha \leq 90°$
50	14.36 ($\alpha = 0$)	12.50 ($\alpha = 80°$)
60	17.68 ($\alpha = 10°$)	13.15 ($\alpha = 80°$)
70	20.54 ($\alpha = 10°$)	13.80 ($\alpha = 80°$)
80	22.41 ($\alpha = 20°$)	14.44 ($\alpha = 80°$)
90	24.73 ($\alpha = 20°$)	15.09 ($\alpha = 80°$)
100	26.73 ($\alpha = 20°$)	15.73 ($\alpha = 80°$)

Similarly, the porous enclosure with aspect ratio $D = 10$ displays transition angles at $\alpha = 30°$ and $\alpha = 40°$ (Figure 2.15). For this aspect ratio, the difference in the Nusselt number between multicellular and single cell convection becomes larger due

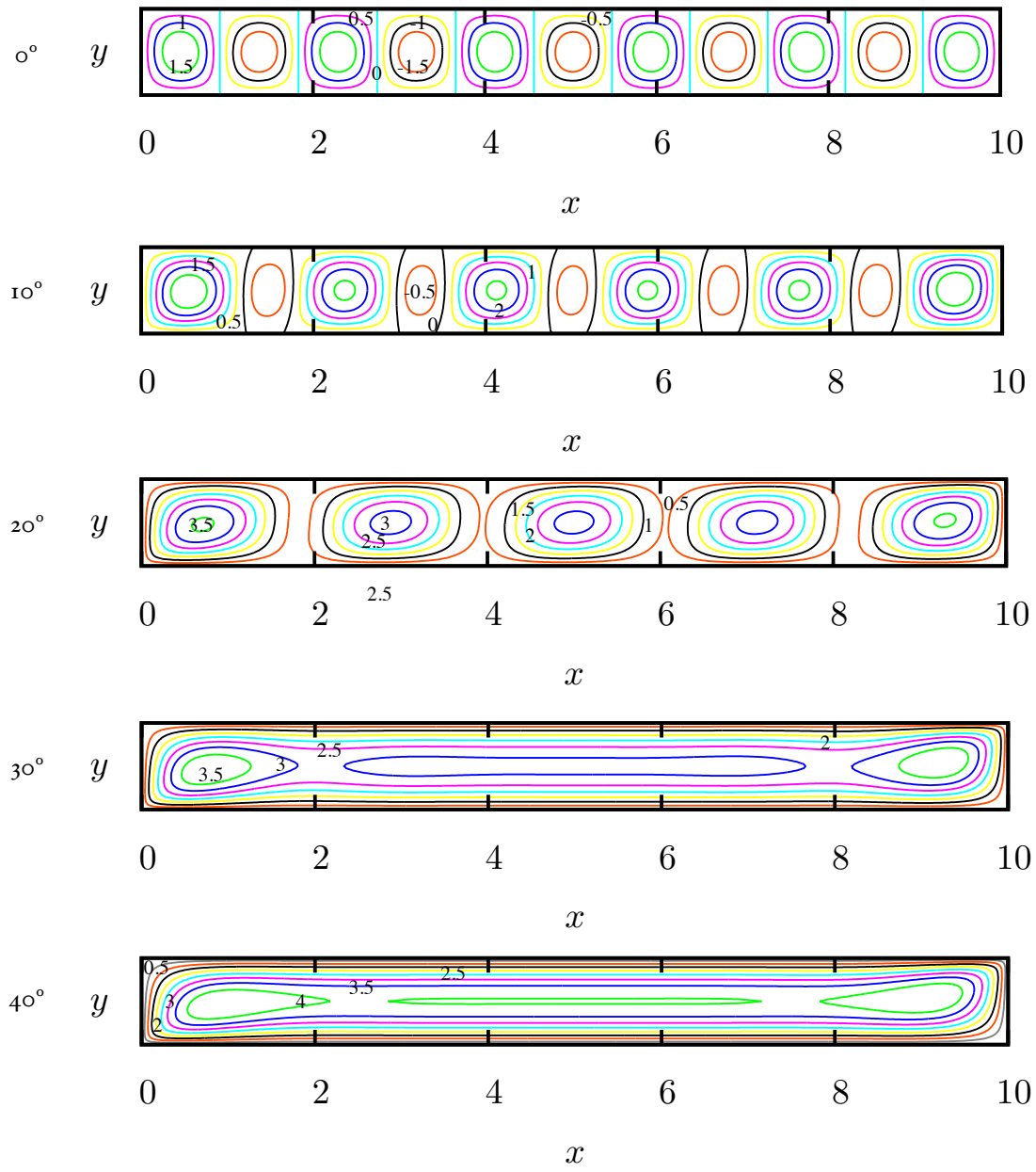

Figure 2.16: Streamlines for a porous enclosure with $D = 10$ and for $Ra = 50$ showing the transition from multicellular flow to single cell convection.

to the fact that multicellular convection considerably enhances the heat transfer in the cavity. The transition from multicellular and single cell convection is shown in Figures 2.16 and 2.17 for $Ra = 50$ and $Ra = 100$, respectively. It can be observed that the number of cells in the multicellular convection depends on Ra. For $\alpha = 0$ for instance, 16 cells are observed at $Ra = 100$, and 11 cells at $Ra = 50$. The local Nusselt maxima are presented in Table 2.4.

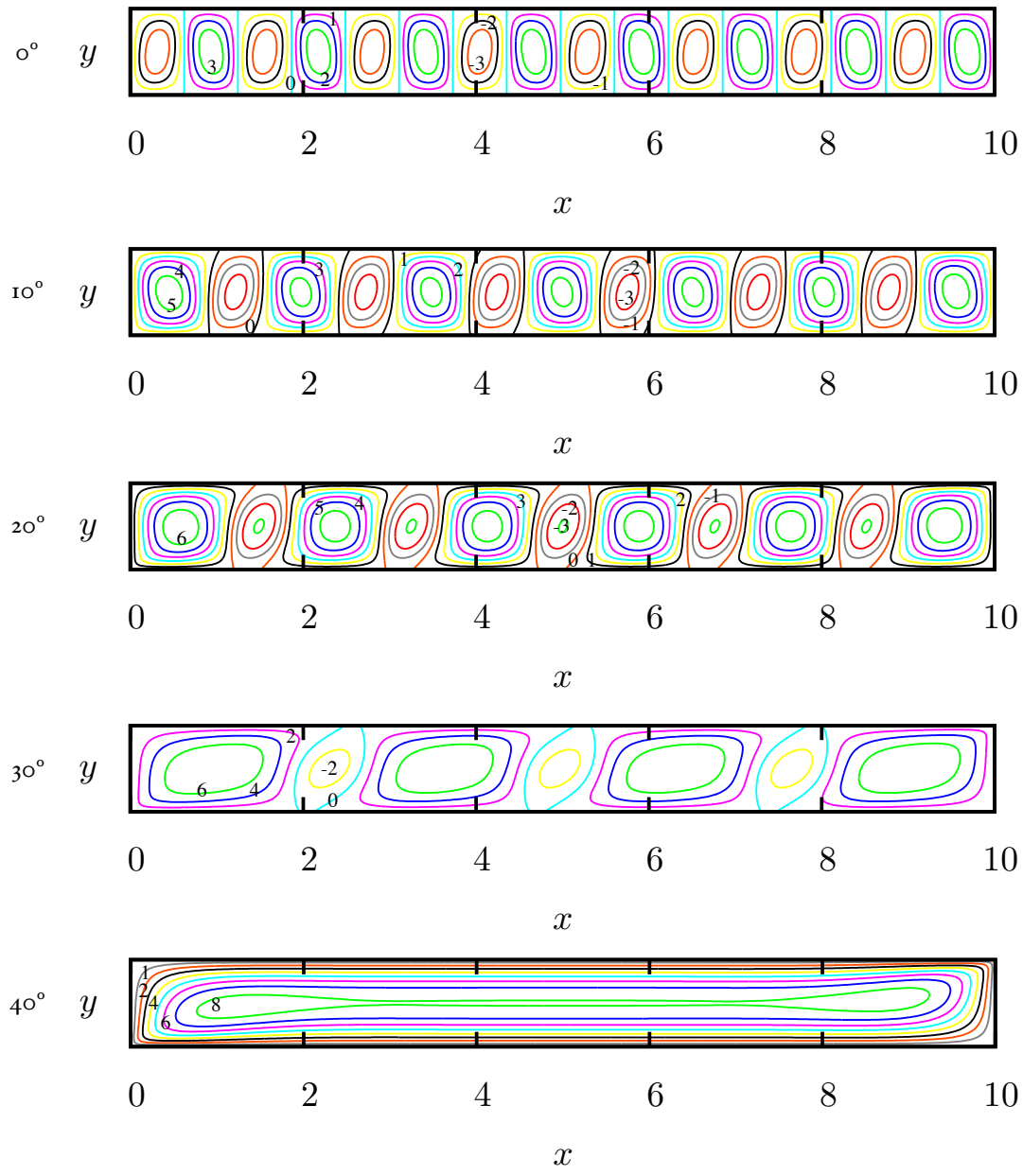

Figure 2.17: Streamlines for a porous enclosure with $D = 10$ and for $Ra = 100$ showing the transition from multicellular flow to single cell convection.

High-resolution parametric study for $Ra = 70$ and $Ra = 100$.

The number of convective cells comprising a multicellular convective mode is studied here numerically for three aspect ratios of the cavity and two Rayleigh numbers. Likewise, more accurate transition angles from multicellular to single-cell convetion are obtained. Suitable initial conditions can be defined to give rise to a specific number of convective cells in a horizontal 2D porous enclosure of aspect ratio D. Such initial condition can be given by the following function:

$$\theta(x, y) = (1 - y) + \hat{A} \sin(\pi y) \cos\left(\frac{n\pi x}{D}\right), \tag{2.26}$$

this equation defines a temperature field that is characteristic of multicellular convection at $\alpha = 0$, with n the number of cells, and $\hat{A}$ the amplitude of the sinusoidal perturbation. In general the amplitude is defined as $0 < |\hat{A}| < 1$, which is a moderate perturbation of the linear temperature profile $(1 - y)$. In this study, an amplitude $|\hat{A}| = 0.3$ was suitable to give rise to multicellular convection at $\alpha = 0$ for a wide number con convective cells, n, and the three aspect ratios analyzed. Additionally, it is important to note that for a given aspect ratio D and number of cells n, the sign of the perturbation, whether it is positive or negative, permits to give rise to equivalent convective modes as regards n but with opposite direction of rotation of the convective cells.

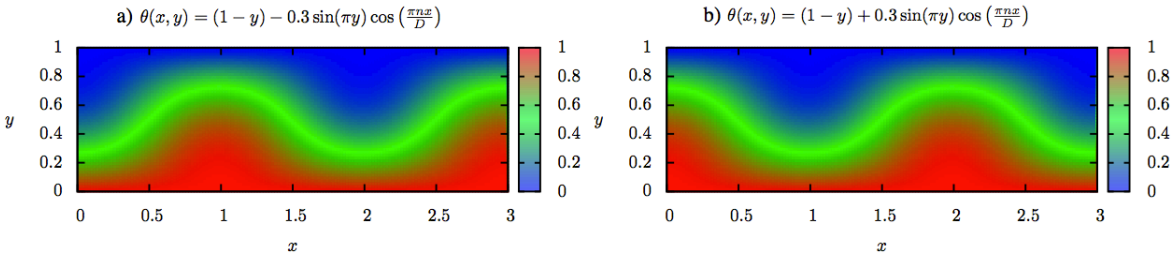

Figure 2.18: Temperature fields obtained from Equation 2.26 for $\hat{A}$=-0.3 and $\hat{A}$=0.3. These can be used as initial conditions to generate multicellular convection consisting of three cells, $n = 3$, in a porous cavity of aspect ratio $D = 3$ (the steady-state solutions obtained form these initial conditions are shown in Figure 2.19).

For $D = 3$ and $n = 3$ for instance, two initial temperature distributions can be calculated according with either a positive or a negative sign of $\hat{A}$, this is shown in Figure 2.18. The corresponding steady-state solutions obtained from these initial conditions are shown in Figure 2.19 for $Ra = 100$ and $\alpha = 0$. This figure shows that two steady-state solutions comprising three cells can be obtained from the same model parameters characterized by opposite vorticity signs. This is a manifestation of multiplicity of solutions of the system. As a consequence of this property, it is pertinent to analyze the existence of the three-cell multicellular convection for $\alpha \neq 0$ considering the two forms of the solution.

The existence of these three-cell solutions (Figure 2.19) in the range $\alpha > 0$ was examined here as follows. The slope angle α was increased in steps of 0.1° up to 40°. For the case $\alpha_1 = 0.1°$, simulations were carried out using the steady-state temperatures obtained for $\alpha_0 = 0$ (Figure 2.19) as the initial conditions. Subsequently, the steady-state temperature fields obtained for α_1 were used as the initial condition for $\alpha_2 = 0.2°$, and so on. This process was continued up to 180°, in steps of 1° in the interval $40° < \alpha < 90°$, and 5° in the interval $90° < \alpha < 180°$. The Nusselt number was then analyzed as a function of the slope angle. The relation Nu vs α permitted to identify the evolution of the three-cell solution and the transition to a single cell

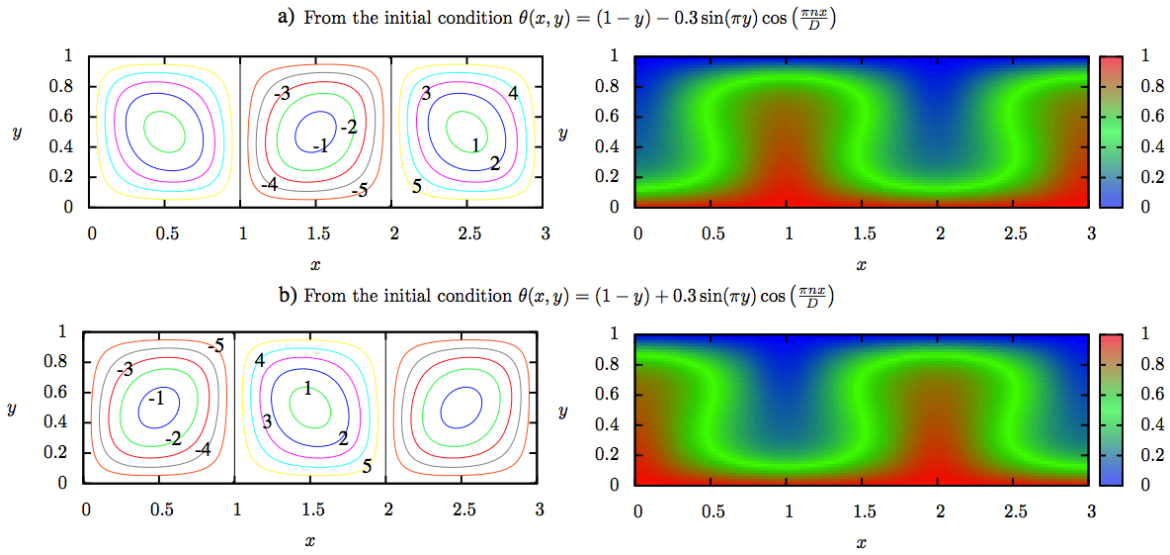

Figure 2.19: Streamlines and temperature fields of three-cell multicellular convection for $Ra = 100$ and $\alpha = 0$ obtained from the initial conditions shown in Figure 2.18.

convective mode.

Figure 2.20 shows the result of the analysis for the three-cell solutions shown in Figure 2.19 along with the four and one-cell solutions ($n = 1$ and $n = 4$). The four-cell solution, $n = 4$, was calculated in the same way as $n = 3$. The one-cell solution however, was obtained from simulations starting at $\alpha = 40°$ with the initial condition given by Equation 2.26 with $n = 1$, $D = 3$, and $\hat{A}$=-0.3.[1] Then the remaining angles were analyzed moving backwards up to $\alpha = 0$ in steps of 0.1°, these simulations allowed the identification of the minimum angle at which the one-cell solution appears.

The figure shows (Fig. 2.20) that the two forms of the three-cell solution evolve in different ways, on the one hand the Nusselt number increases with α for the configuration shown in Figure 2.19-a ($\hat{A}$=-0.3). This result is consistent with that presented in the overall parametric study (Fig. 2.11). The convection in this case consists of two cells rotating anti-clockwise, that can be called natural cells, since the fluid next to the hot wall flows upwards, whereas there is one clockwise rotating cell, or anti-natural cell. This multicellular configuration will be denoted as $n = 3^+$. On the other hand, the configuration shown in Figure 2.19-b leads to a quick decrease in the Nusselt until 11.1°, where the rotation of the cells is switched to adopt the configuration $n = 3^+$. This decreasing branch of the three-cell solution contains only one natural cell and two anti-natural cells, this explains why the Nusselt number associated with this configuration is low, and why it exists only in relatively small slope angles. Similarly, this configuration will be denoted as $n = 3^-$.

[1]For convenience the starting angle was increased to 60° for $D = 5$ and $D = 10$ at $Ra = 100$.

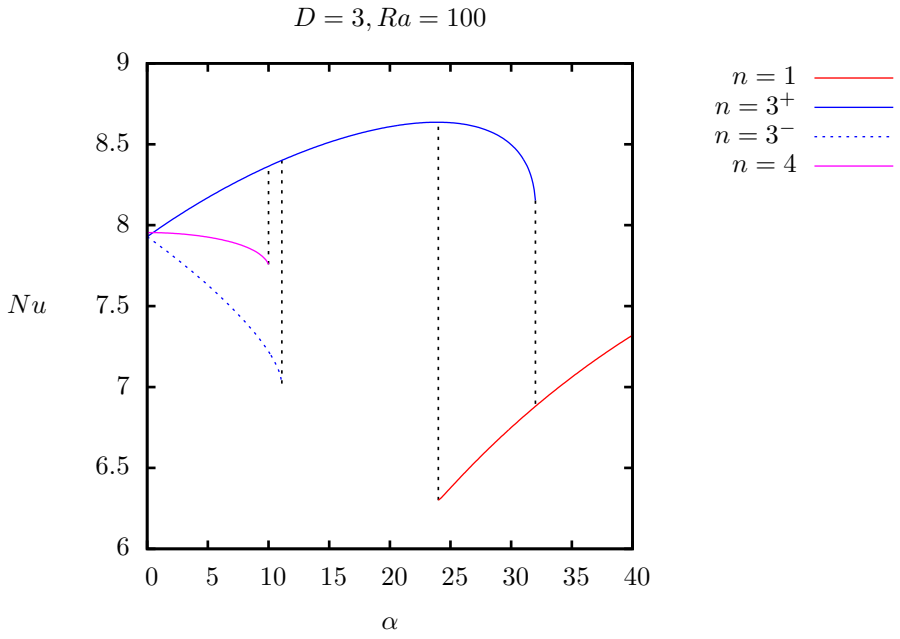

Figure 2.20: Nu vs α for three, four-cell, and one-cell convection. The solid blue line corresponds to the case $\hat{A}$=-0.3, whereas the dashed blue line in the same interval corresponds to $\hat{A}$=0.3 (Figure 2.19). The black dashed line shows the transition between number of cells.

Similar to the three-cell case for $\alpha = 0$, two steady-state solutions were obtained for the four-cell configuration with opposite signs of vorticity, each of the solutions associated with a sign of the perturbation (Eq. 2.26). Despite having opposite sign of vorticity, the Nusselt number as a function of α turned out to be the same in both cases: the Nusselt number decreased up to 10° where the convection became $n = 3^+$ (Figure 2.20). This behavior is explained by the fact that both four-cell solutions have two natural and two anti-natural cells, the only difference is the position of them, so that both cases are equivalent in terms of the heat transfer in the porous enclosure. It can also be observed a zero-slope curve at $\alpha = 0$, unlike the curves for the three cell configurations.

It is important to observe what happens at the end of the curves, which is the transition to a different configuration. The Nusselt number for $n = 3^+$ has a maximum at $\alpha = 24°$ and then decreases until the slope tends to infinite. It is expected that the three-cell configuration starts vanishing at this high slope region. Figure 2.21-a shows the streamlines for this configuration at the transition angle $\alpha = 32°$, the internal cell has almost disappeared which resembles a two-cell configuration, yet the two cells have the same direction of rotation characteristic of the three-cell convection. An increase up to $\alpha = 32.1°$ leads to single-cell convection. On the other hand, the transition from $n = 3^-$ to $n = 3^+$ shows a deformation of the external cells at $\alpha = 11.1°$ (Figure 2.21-b), and then for $\alpha = 11.2°$ the configuration changes to

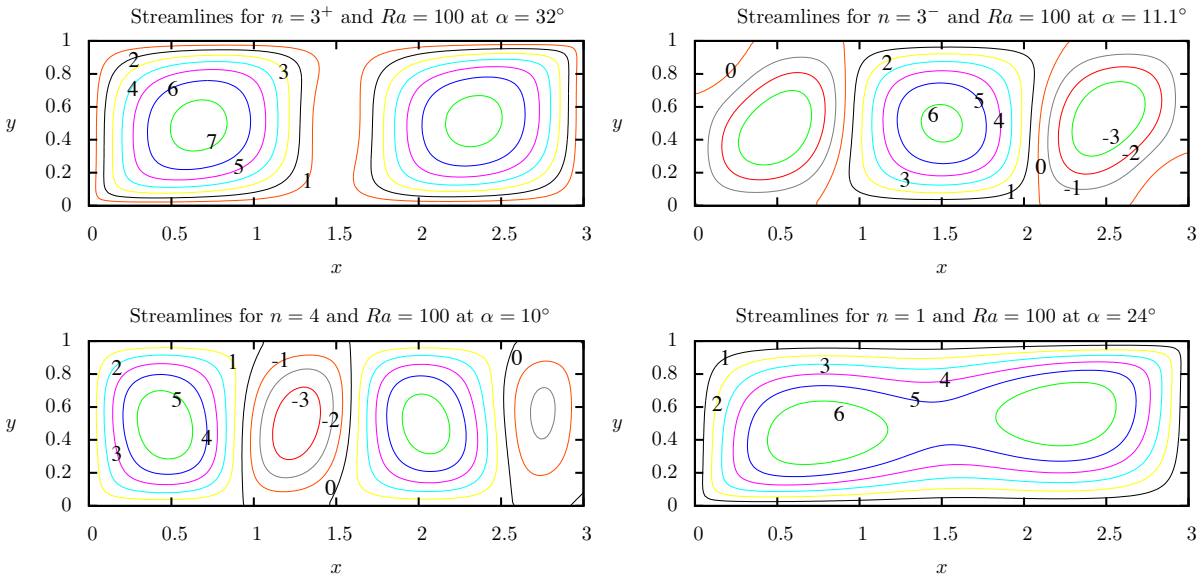

Figure 2.21: Streamlines of the convective modes $n = 1$, $n = 3^+$, $n = 3^-$, and $n = 4$ at their transition angles to a different configuration.

$n = 3^+$. Likewise, for $n = 4$ the external anti-natural cell vanishes (Figure 2.21-c) and then the configuration changes to $n = 3^+$. Finally, $n = 1$ was observed until $\alpha = 24°$ which is single cell with two internal cells (Figure 2.21-d).

In summary, each of the convection configuration starts becoming unstable at the end of the curves, so that a further increase in α gives rise to a transition to a different convective mode. The transition angles presented here are by no means definitive, steady-state simulations would be required to confirm whether these configurations exist beyond the transition angles presented here, nonetheless these results provide the order of magnitude of the transition angles, the strength of the different configurations as α varies, and their relative importance as regards the Nusselt number in the cavity.

The behavior observed for the three and four-cell solutions can be generalized for all the odd and even number of cells at any aspect ratio. Additionally, considering the property of symmetry regarding the rotation of the cavity, the results can be extrapolated to the range $\alpha < 0$. From these considerations, the cases $n = 1$, 2, ..., 5 were analyzed for $D = 3$, the cases $n = 1$, 3, 4, ..., 11 for $D = 5$, and the cases $n = 1$, 7, 8, ..., 19 for $D = 10$. The presence of these multicellular convective modes was analyzed considering two Rayleigh numbers $Ra = 70$ and $Ra = 100$.

Figure 2.22 shows the results for $D = 3$ and $Ra = 70$, it can be observed that the configuration $n = 3^+$ is dominant as regards the Nusselt number and the range α. The configuration $n = 3^-$ on the other hand, displays a high-rate decrease in Nu, yet the Nusselt number is higher than the that related with $n = 2$, 4, and 5. It can be observed that the one-cell solution presents a bend upwards before the transition,

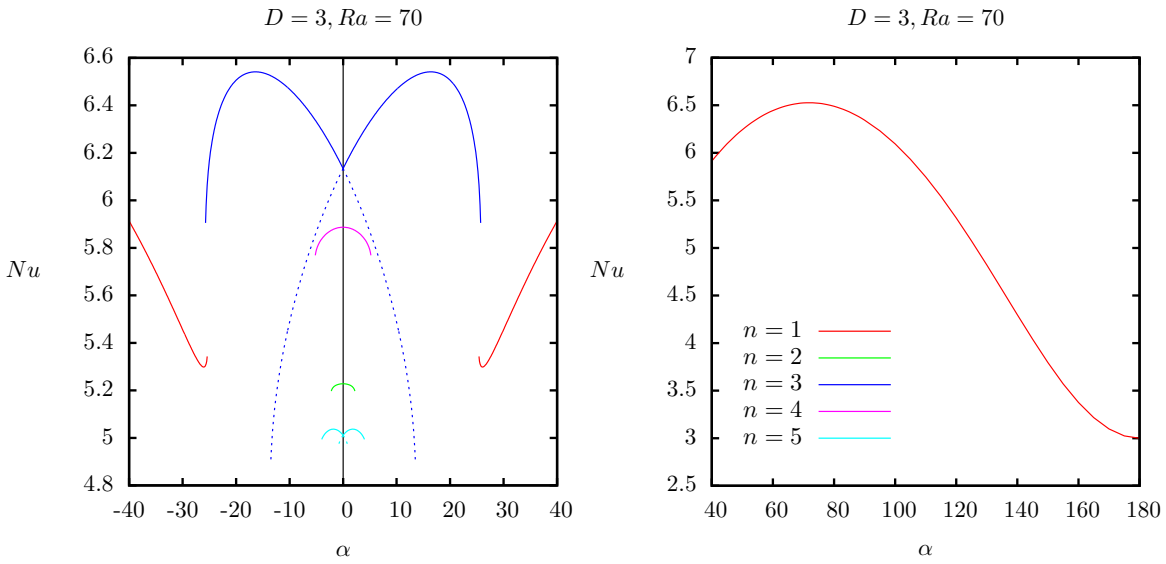

Figure 2.22: Nusselt number vs slope angle for $n = 1, 2, ..., 5$ convective cells in a 2D porous cavity of aspect ratio $D = 3$ and $Ra = 70$ (for n odd, the dotted line represents the configuration n^- and the continuous line represents n^+).

unlike the one-cell curve for $Ra = 100$ (Fig. 2.20), nevertheless it was confirmed that the convective mode at the end of this curve is also once-cell with internal secondary cells, similar to that presented in Figure 2.21-d. The transition angles for this case are presented in Table 2.5. Additionally, the curve $n = 1$ evolves in a sinusoidal way up to 180° reaching a minimum equal to the aspect ratio $D = 3$ at $\alpha = 180°$. Since this case is equivalent to a cavity heated form above there is no convection contributing to the heat transfer throughout the cavity but only conduction, therefore the Nusselt

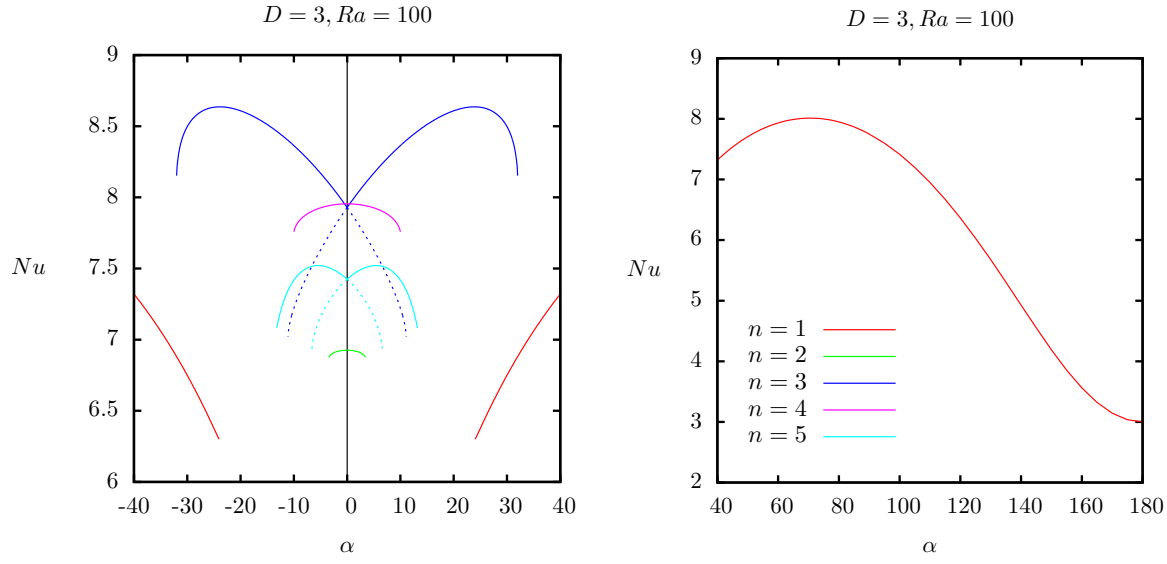

Figure 2.23: Nusselt number vs slope angle for $n = 1, 2, ..., 5$ convective cells in a 2D porous cavity of aspect ratio $D = 3$ and $Ra = 100$ (for n odd, the dotted line represents the configuration n^- and the continuous line represents n^+).

number is equal to the steady-state conductive solution of a cavity with a linear temperature profile $\theta(x, y) = 1 - y$.

Figure 2.23 shows the results for $Ra = 100$ that was partly described above (Fig. 2.20). Unlike $Ra = 70$ the maximum Nu at $\alpha = 0$ in this case is associated with an even number of cells $n = 4$, which is slightly higher than that for $n = 3$. Likewise, at this Rayleigh number the multicellular configurations remain in wider range α with the exception of $n = 3^-$. The transition angles of the different configurations observed are presented in Table 2.5. There is consistency regarding the configuration to which each case n becomes, being $n = 3^+$ the preferred convective mode that is adopted. It can be observed that there is an increase in the maximum transition angle to single cell, being 25.7° for $Ra = 70$ and 32° for $Ra = 100$.

Table 2.5: Transition angles of the multicellular configurations observed in $D = 3$ for $Ra = 70$ and $Ra = 100$ (the transition to odd number of cells is always to the positive branch n^+).

$D = 3$					
$Ra = 70$			$Ra = 100$		
n	Transition to	α_t	n	Transition to	α_t
1	3	25.4	1	3	24.0
2	3	2.2	2	3	3.4
3^+	1	25.7	3^+	1	32.0
3^-	3	13.5	3^-	3	11.1
4	3	5.2	4	3	10.0
5^+	3	4.0	5^+	3	13.2
5^-	4	0.8	5^-	4	6.6

Regarding the transition angles, Rees & Bassom (2000) presented a linear stability analysis for the onset of convection in an infinitely long sloping porous layer heated from below. They found the maximum inclination angle at which transverse convective modes can become unstable, which is $\alpha = 31.49032°$. This condition is satisfied by $Ra = 70$, where $n = 3^+$ is destabilized at $\alpha = 25.7°$, for $Ra = 100$ however, the transition for $n = 3^+$ occurs at a slightly higher angle $\alpha = 32°$ (Table 2.5).

A test simulation was carried out in order to confirm this result. The case $n = 3^+$ for $Ra = 100$ at $\alpha = 32°$ was simulated again with no convergence criterion, using instead a total simulation time $t = 100$. The resulting Nusselt number was $Nu = 8.147451$, whereas the Nusselt with convergence criterion was $Nu = 8.152843$ referred to a simulation time for steady state $t_{ss} = 4.83$. This accounts for a difference in Nu of about 0.066%. Likewise, no appreciable change was observed in the streamlines for the new result in comparison with those presented in Figure 2.21-a. It is important to mention that even larger transition angles were observed (up to 45°) when higher

aspect ratios were analyzed (Tables 2.6 and 2.7). All these cases were associated with odd number of cells.

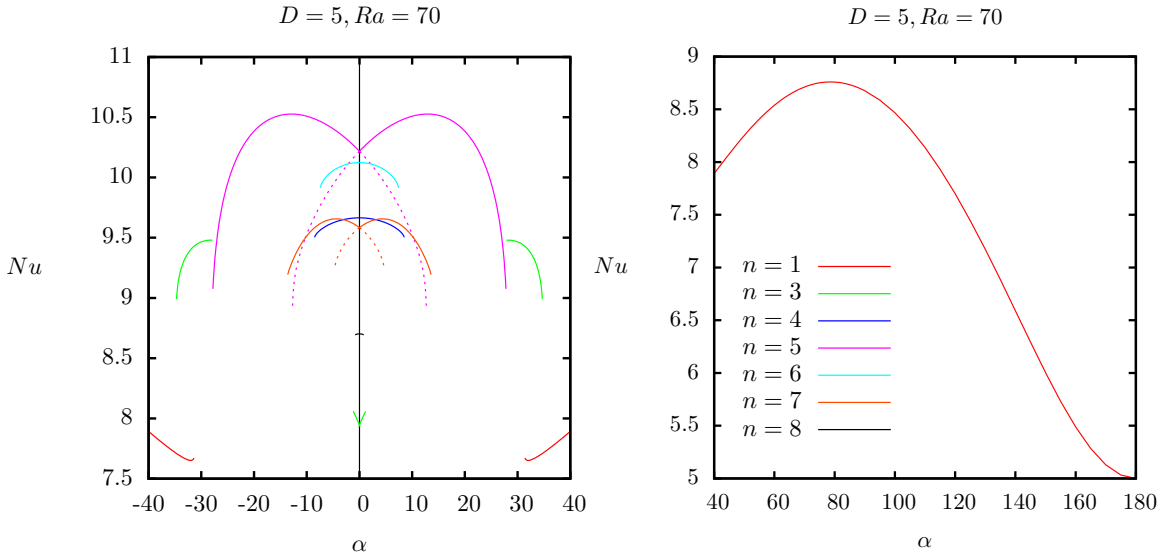

Figure 2.24: Nusselt number vs slope angle for $n = 1$, 3, 4, ..., 8 convective cells in a 2D porous cavity of aspect ratio $D = 5$ and $Ra = 70$ (for n odd, the dotted line represents the configuration n^- and the continuous line represents n^+).

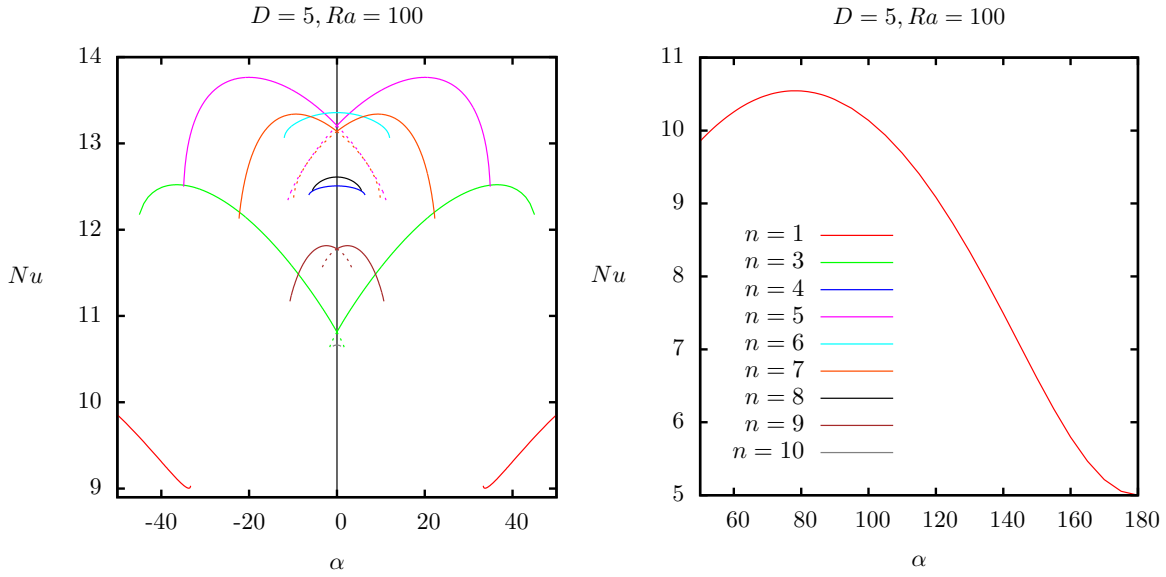

Figure 2.25: Nusselt number vs slope angle for $n = 1$, 3, 4, ..., 11 convective cells in a 2D porous cavity of aspect ratio $D = 5$ and $Ra = 100$ (for n odd, the dotted line represents the configuration n^- and the continuous line represents n^+).

Figure 2.24 presents the Nusselt number as a function of α for $D = 5$ and $Ra = 70$ and Figure 2.25 for $Ra = 100$. In both Rayleigh numbers, the cases $n = 1$, 3, 4, ..., 11 were examined however, for $Ra = 70$, $n = 8$ was the maximum number of cells that constituted steady-state. When comparing these two Figures, it can be observed that increasing the Rayleigh number favors the formation of more multicellular configura-

tions (Straus 1974). Likewise there is in general an increase in the transition angles (Table 2.6). As regards $Ra = 70$ (Fig. 2.24), $n = 5^+$ is the dominant configuration which terminates at $\alpha = 27.8°$. There is an interesting feature in this graph, $n = 3^+$ is interrupted at $\alpha = 1.2°$ where it becomes $n = 5^+$, and then it appears again at $\alpha = 27.8°$, it finally changes to $n = 1$ at $\alpha = 34.7°$. Since the Nusselt number for this case is too low at small α it is possible that in cannot remain as steady state at small inclination angles, more refined steady-state modelling would be required however to confirm whether it cannot be steady-state in the range $1.2° < \alpha < 27.8°$.

Table 2.6: Transition angles of the multicellular configurations observed in $D = 5$ for $Ra = 70$ and $Ra = 100$ (the transition to odd number of cells is always to the positive branch n^+).

$D = 5$					
$Ra = 70$			$Ra = 100$		
n	Transition to	α_t	n	Transition to	α_t
1	3	31.4	1	3	33.3
3^+	5	1.2	3^+	1	45.0
3^-	4	0.1	3^-	5	1.9
4	5	8.5	4	5	6.4
5^+	3	27.8	5^+	3	34.9
5^-	5	13.1	5^-	7	11.4
6	5	7.4	6	5	12.0
7^+	5	13.6	7^+	5	22.3
7^-	5	4.7	7^-	5	9.9
8	7	0.8	8	7	5.6
—	—	—	9^+	7	10.7
—	—	—	9^-	7	3.6
—	—	—	10	9	0.9

It can also be observed in these Figures that the maximum Nusselt number for $\alpha = 0$ corresponds to $n = 5$ at $Ra = 70$ and $n = 6$ at $Ra = 100$, this increase in the number of cells is consistent with the predictions presented by De La Torre Juárez & Busse (1995) (a similar behavior can be observed for $D = 3$ and $D = 10$). Regarding $Ra = 100$, as α is increased $n = 5^+$ becomes the dominant configuration remaining up to $\alpha = 34.9°$ where it becomes three-cell convection (Table 2.6). It can be observed that as the number of cells increases the corresponding Nusselt number decreases as well as the range α in which the particular configuration exists, such is the case of $n = 10$ that appears in a range of inclinations less than 1°. The highest transition angle observed for $Ra = 100$ is 45° corresponding to $n = 3^+$, at this angle the gravitational effects are equally distributed between the x and y axes of the cavity.

Finally, the Figures for the aspect ratio $D = 5$ at 180° show a Nusselt number equal to 5. Similar to case $D = 3$, this Nusselt number is equivalent to that obtained from

a purely conductive solution $\theta(x, y) = 1 - y$, since the cavity is being heated from the top and cooled from below.

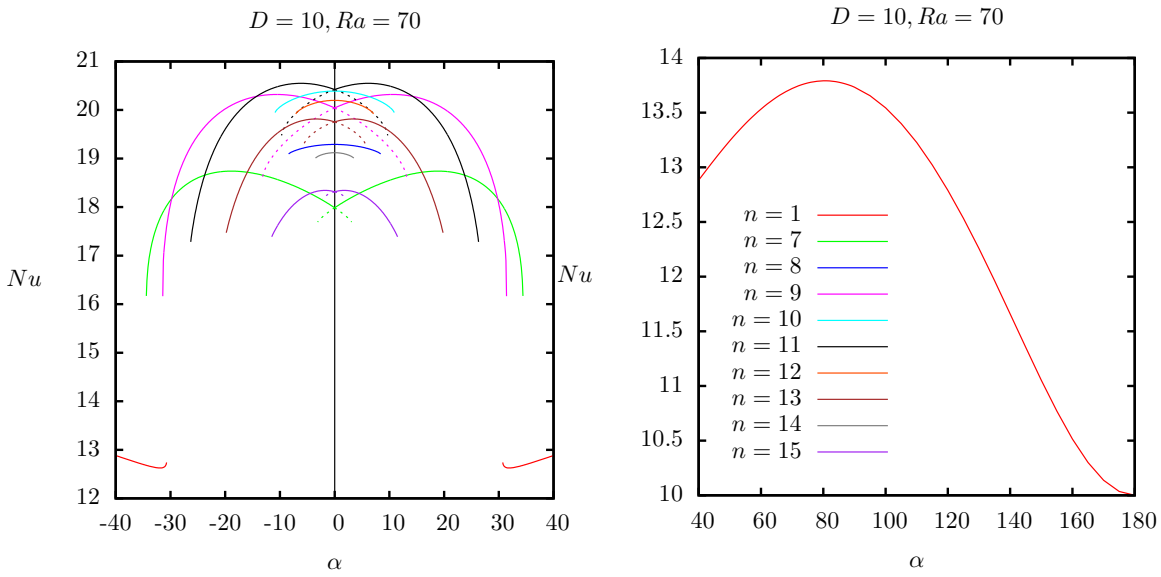

Figure 2.26: Nusselt number vs slope angle for $n = 1$, 7, 8, ..., 15 convective cells in a 2D porous cavity of aspect ratio $D = 10$ and $Ra = 70$ (for n odd, the dotted line represents the configuration n^- and the continuous line represents n^+).

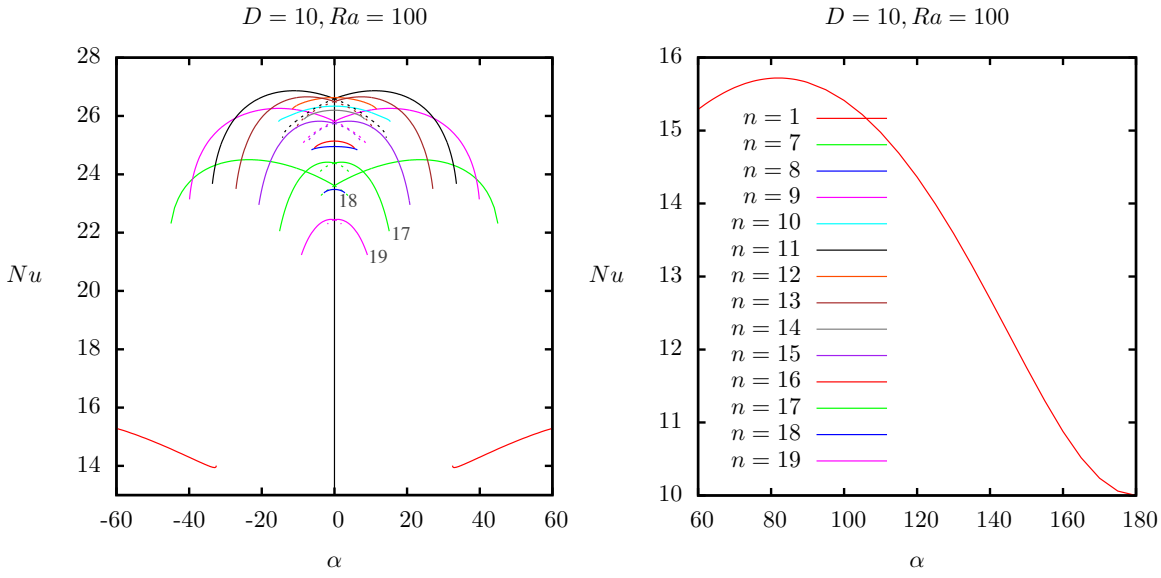

Figure 2.27: Nusselt number vs slope angle for $n = 1$, 7, 8, ..., 19 convective cells in a 2D porous cavity of aspect ratio $D = 10$ and $Ra = 70$ (for n odd, the dotted line represents the configuration n^- and the continuous line represents n^+).

The fact that multicellular convective modes with odd number of cells prevail beyond the critical angle predicted by Rees & Bassom (2000) is an evidence for the strong convection of those modes. It can be expected that there are some forms of multicellular convection in the range $31.49 < \alpha < 45°$ since the component of the external force due to gravity is larger on the y-axis than on the x-axis, which favors

flow in the y direction. This means that multiple upwellings and downwellings are possible in the y-direction as long as $\alpha < 45°$. An increase of this angle destabilize any multicellular convection to give rise to single-cell convection, in response to a larger component of the external force on the x-axis. The presence of these convective modes in the range $31.49 < \alpha < 45°$ can be justified by the fact that single-cell convection consists of a flow of the form $\sin(\pi x/D)$, but since the flow is non-linear it can self-interact to cause components of the form $\sin(3\pi x/D)$, $\sin(5\pi x/D)$, etc., allowing strong convection of theses modes.

Table 2.7: Transition angles of the multicellular configurations observed in $D = 10$ for $Ra = 70$ and $Ra = 100$ (the transition to odd number of cells is always to the positive branch n^+).

$D = 10$					
$Ra = 70$			$Ra = 100$		
n	Transition to	α_t	n	Transition to	α_t
1	7	30.6	1	7	32.4
7^+	1	34.4	7^+	1	45.0
7^-	9	3.2	7^-	15	4.1
8	9	8.5	8	9	6.4
9^+	1	31.4	9^+	1	40.0
9^-	7	13.3	9^-	13	8.8
10	9	11.0	10	9	15.5
11^+	7	26.4	11^+	7	33.7
11^-	9	9.8	11^-	9	14.4
12	7	7.2	12	11	11.7
13^+	11	19.9	13^+	9	25.9
13^-	11	5.8	13^-	11	10.6
14	13	3.6	14	13	8.4
15^+	13	11.6	15^+	11	20.9
15^-	13	2.3	15^-	12	7.4
—	—	—	16	15	5.6
—	—	—	17^+	13	15.2
—	—	—	17^-	15	4.5
—	—	—	18	17	3.0
—	—	—	19^+	15	9.2
—	—	—	19^-	17	2.0

The parametric analysis for $D = 10$ is shown in Figures 2.26 and 2.27, the cases from $n = 7$ up to $n = 21$ were examined. Between 7 and 15 cells were observed for $Ra = 70$, and between 7 and 21 cells for $Ra = 100$, the cases $n = 20$ and $n = 21$ were marginal though (lying in the range $0 \leq \alpha \leq 1°$) and are not shown in Figure 2.27. For $Ra = 70$ it can be observed that $n = 9^+$ and $n = 11^+$ are dominant regarding Nu, but $n = 7^+$ prevails in a wider range of inclination angles, with an angle of transition $\alpha = 34.4°$.

Likewise, for $Ra = 100$ (Figure 2.27), the dominant convective modes are $n = 9^+$ and $n = 11^+$ regarding Nu, and $n = 7^+$ is the dominant mode regarding the transition angle being $\alpha = 45°$. It can be clearly seen in this Figure for $\alpha = 0$ that a large number of convective cells does not necessarily mean a high Nusselt number. It can be seen that from about 13 cells the Nusselt number of the n-odd cases starts decreasing. On the other hand, for n even, $n = 12$ has the highest Nusselt number and form $n = 14$ Nu decreases.

A common characteristic of the two Figures is that there is a large decrease in Nu as the convective modes evolve towards single-cell convection. As it was mentioned in the overall study this due to the large difference in the number of upwellings between multicellular and single-cell convection that can be hosted in large aspect ratio. Additionally, it can be seen that as n increases the convective modes are destabilized at successively smaller angles, for $Ra = 70$ for instance, the highest transition angle corresponds to $n = 7^+$ and then the transition angle decreases monotonically as n increases, the same happens for the n-even cases, being $n = 12$ the convective mode with the highest transition angle.

2.6 Conclusion

Two numerical models for free convection in a 2D porous enclosure were developed and validated. The models were based on the primitive variables approach and the stream function approach for which the solution algorithms and numerical discretization were described. The primitive variables approach led to a non-iterative algorithm per time step, which makes it easy to implement in a computational code, whereas the stream function approach requires an iterative algorithm. Despite this fact, the primitive variables model turned out computationally slower than the stream function model. A comparison of the models was carried out using the case study of a sloping porous enclosure. The numerical results were in agreement as regards the local Nusselt number with small differences. Likewise, the numerical results were in agreement with those reported by Báez & Nicolás (2006) and Baytaş (2000). In this validation, multiplicity of solutions was observed in the case of the horizontal square porous cavity reported by Baytaş (2000).

Parametric studies were carried out to provide an overall view of the Nusselt number as a function of the governing parameters of the system. Additionally, the study determined most of the steady-state solutions that are possible in 2D along with their transition angles to other convective modes. The steady-state convection was grouped into two modes: multicellular convection for moderate slope angles, and single cell for large angles. Multiple multicellular solutions were obtained for the horizontal

cavity ($\alpha = 0$) based on the property of multiplicity. Each of these multicellular configurations was characterized by a given number of cells and by either of two possible distributions of signs of the vorticity of the cells. Some of these configurations proved to be more stable than others and prevailed in different extent as α was varied.

The configurations consisting of odd number of cells displayed a common behavior regarding the trend of the Nusselt number as α was varied. On the one hand, when the predominant sign of vorticity of the cells matched with the sign of vorticity of the single-cell convection for $\alpha \to 90°$, Nu increases until a maximum is reached and then decreases to adopt either a different number of cells or the single-cell configuration. Otherwise, if the predominant rotation of the cells is against the single-cell natural convection, the Nusselt number decreases monotonically as α varies and becomes unstable quickly. The n-even solutions also displayed a common behavior. Since in this case both distributions of signs of vorticity contain the same number of clockwise and anti-clockwise rotation cells, the Nusselt number of both forms of the solution behaved in the same way as α was varied unlike the n-odd case; Nu decreased monotonically with α forming a zero-slope curve as $\alpha \to 0$. These solutions became unstable relatively quickly as α increased in comparison with the n-odd solutions.

Transition angles for all these solutions were also obtained. The results showed that multicellular convection can become unstable at angles larger than the critical angle predicted by Rees & Bassom (2000) ($\alpha = 31.49°$). Some of the multicellular convective modes were destabilized and became single-cell at angles as large as $\alpha = 45°$ which represents the physical limit for multicellular convection. The explanation to this behavior can be associated with the fact that below this angle (45°) gravitational effects have a larger component in the y-direction favoring the formation of multiple upwellings in this direction. Likewise, in relation with the stability analysis presented by Rees & Bassom (2000) it can be argued that the single-cell solution self interacts due to nonlinearities to create n-odd solutions in the range $31.49° < \alpha < 45°$.

Chapter 3

3D numerical modeling of free convection in a sloping porous enclosure

3.1 Introduction

As it was presented in the previous chapter, the problem of free convection in sloping porous enclosures has been widely investigated. The interest in this problem arises from several application contexts. Porous layers that are inclined with respect to the horizontal level are frequently found in nature and engineering systems. Geothermal energy and ground water modeling are examples of this. Permeable horizons in hydrothermal systems can have this characteristic so that gravitational effects are present in all the coordinate axes.

Steady-state solutions of free convection in sloping porous enclosures in three dimensions are presented in this chapter for a range of governing parameters (aspect ratio, slope angle and Rayleigh number). The 3D convective modes observed in the parameter space will be compared with the 2D results presented in the previous chapter.

The theoretical basis of the analysis presented in this chapter lies on the early works by Horton & Rogers (1945) and Lapwood (1948) introduced previously. After an early numerical model by Elder (1967), who studied steady-state convection in a 2D porous enclosure, Bories & Combarnous (1973) extended the analysis to a sloping porous enclosure in 3D following an experimental and theoretical approach. They observed three different kinds of convective regimes, dependent on the parameters of the model: polyhedral cells similar to the Bénard-Rayleigh cells for small slope angles ($\sim 15°$), longitudinal coils (with axis parallel to the longest side of the box) and unicellular flow (which is a 2D velocity distribution) for nearly vertical positions. Regarding the possible convective modes in a horizontal porous enclosure, Holst &

Aziz (1972) presented one of the earliest numerical models to study this problem in 3D. Considering a set of aspect ratios of a horizontal porous enclosure they determined the possible convective modes for several Rayleigh numbers. They pointed out that as the 2D motion always satisfies the governing equations, when 3D steady state is possible, then the problem is characterized by a multiplicity of solutions. In a later 3D study by Schubert & Straus (1979) the Rayleigh numbers at which 2D and 3D solutions can be steady were examined for the case of a cubic porous enclosure. Horne (1979) emphasized that steady flows do not necessarily maximize the energy transfer. When multiple solutions are possible, these early studies agree on the dependence of the resulting steady flow on the initial conditions of the problem. Caltagirone & Bories (1985) presented a theoretical and numerical study for a sloping porous box, their results were consistent with the experimental results by Bories & Combarnous (1973). However they also predicted convective regimes characterized by the interaction of longitudinal coils and transverse rolls. More recent research has been carried out by Barletta & Storesletten (2011) to study the stability of transverse and longitudinal convective rolls in an inclined porous channel. These authors described the discontinuous nature of the critical Rayleigh number as a function of the inclination angle.

The aim of the analysis presented in this chapter is to illustrate the complexity of the steady-sate convective modes that can be present in 3D porous enclosures even at low Rayleigh numbers, and to highlight the importance of 3D modeling for a better understanding of this problem in real three-dimensional systems.

3.2 Problem formulation

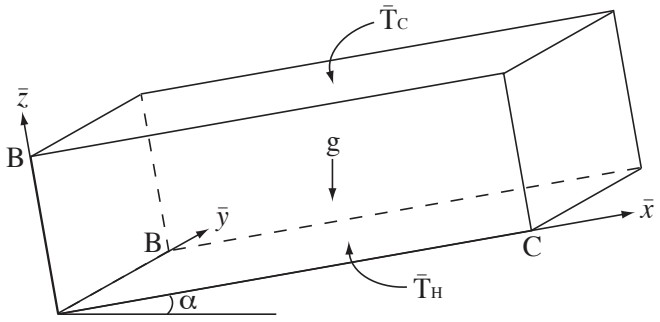

Figure 3.1: Schematic model of a sloping porous enclosure heated from below and cooled from the top with adiabatic lateral boundaries.

The problem consists of a rectangular porous cavity, tilted at an angle α with respect to the horizontal axis (Figure 3.1). The porous medium is assumed to be homogeneous and fully saturated. The problem was stated assuming local thermal

equilibrium. Fluid flow is described by Darcy's law and buoyancy effects by the Boussinesq approximation. Viscous heat generation is assumed negligible. From these considerations the momentum equation can be stated as follows:

$$\bar{\mathbf{u}} = -\frac{k}{\mu}\left(\bar{\nabla}\bar{P} - \rho_0 g\beta(\bar{T} - \bar{T}_0)\mathbf{e}\right), \tag{3.1}$$

where k, μ, ρ_0, β, and g are permeability, viscosity, density of reference, thermal expansion coefficient and gravitational constant, respectively. Likewise $\mathbf{e} = (\sin\alpha, 0, \cos\alpha)$ gives account of the components of the gravity in the system. We recall the heat transfer equation

$$\sigma\frac{\partial\bar{T}}{\partial\bar{t}} + \bar{\mathbf{u}}\cdot\bar{\nabla}\bar{T} = \bar{\nabla}\cdot(\eta\bar{\nabla}\bar{T}), \tag{3.2}$$

where η is the thermal diffusivity. The condition of incompressibility of the fluid is also invoked:

$$\bar{\nabla}\cdot\bar{\mathbf{u}} = 0. \tag{3.3}$$

Dimensionless variables are defined as follows:

$$x = \frac{\bar{x}}{B}, \quad y = \frac{\bar{y}}{B}, \quad z = \frac{\bar{z}}{B}, \quad P = \frac{k}{\mu\eta}\bar{P},$$

$$\mathbf{u} = \frac{B}{\eta}(\bar{u}, \bar{v}, \bar{w}), \quad \theta = \frac{\bar{T} - \bar{T}_0}{\bar{T}_0 - \bar{T}_c}, \quad t = \frac{\bar{t}\eta}{\sigma B^2},$$

$$Ra = \frac{Bkg\beta\rho_0}{\eta\mu}(\bar{T}_0 - \bar{T}_c),$$

where Ra is the Darcy-Rayleigh number and B the characteristic length. The dimensionless equations are then as follows, heat transfer equation:

$$\frac{\partial\theta}{\partial t} - \nabla^2\theta + \mathbf{u}\cdot\nabla\theta = 0. \tag{3.4}$$

The dimensionless momentum equation reads:

$$\mathbf{u} + \nabla P = Ra\theta\mathbf{e}. \tag{3.5}$$

In this case the domain is given by $0 \le x \le D$, $0 \le y \le 1$, $0 \le z \le 1$, with $D = C/B$, the aspect ratio. Additionally, a global Nusselt number is defined to quantify the heat transfer through the upper surface $z = 1$:

$$Nu = \int \left|\frac{\partial\theta}{\partial z}\right|_{z=1} dA. \tag{3.6}$$

3.2.1 Boundary conditions and initial conditions

It is assumed that the system rests at mechanical and thermal equilibrium as the initial condition. Additionally, the initial dimensionless temperature is set to zero. Assuming that the lateral walls of the cavity are adiabatic ($x = 0$, $x = D$, $y = 0$, $y = 1$) and the bottom and top boundaries have specified temperatures, the boundary conditions for the heat transfer equation can be written as

$$\frac{\partial \theta}{\partial x} = 0, \quad \text{for} \quad x = 0 \quad \text{and} \quad x = D,$$
$$\frac{\partial \theta}{\partial y} = 0, \quad \text{for} \quad y = 0 \quad \text{and} \quad y = 1,$$

$$\theta = 1, \quad \text{for} \quad z = 0 \quad \text{and} \quad \theta = 0, \quad \text{for} \quad z = 1 \quad \text{for} \quad t > 0.$$

Regarding the momentum equation impermeable boundary conditions are assumed. The implementation of these boundary conditions is described in the following section.

3.3 Numerical solution

As the two-dimensional problem described in the previous chapter there are two numerical approaches to solve the problem given above: primitive variables and vector potential. The vector potential approach is analogous to the stream function approach in the sense that pressure is eliminated from the equations. This approach has been historically preferred (Holst & Aziz 1972, Horne 1979, Hewitt et al. 2014a, Harfash 2014), since it has proven to be a faster computational algorithm. A comparison of these two methods has not been presented before in the literature however.

3.3.1 Primitive variables approach

As it was mentioned in the previous chapter, taking the divergence of Equation 3.5 and considering the incompressibility condition, it is obtained a Poisson equation for the pressure:

$$\nabla^2 P = Ra \left(\frac{\partial \theta}{\partial x} \sin \alpha + \frac{\partial \theta}{\partial z} \cos \alpha \right). \tag{3.7}$$

As it was done in the previous chapter, Neumann boundary conditions for this Poisson equation are obtained from the momentum equation (Eq. 3.5). Again, let us define

the boundary of the enclosure as a surface Ω . Then the pressure gradient normal to the surface must satisfy the following condition (Báez & Nicolás 2013).

$$\frac{\partial P}{\partial \mathbf{n}}\Big|_{\Omega} = \mathbf{n} \cdot (Ra\theta\mathbf{e} - \mathbf{u})|_{\Omega} \tag{3.8}$$

The velocity component normal to the boundary is zero in this equation. No restriction is required regarding the tangential velocity (further details of this approach can be referred to Orszag et al. (1986) and Karniadakis et al. (1991)). As it was mentioned in the previous chapter, this boundary condition ensures mass conservation and leads to a non-iterative solution algorithm for the problem given by Equations 3.4 and 3.7 with the corresponding boundary and initial conditions. The algorithm was described previously (Figure 2.2), it consists of a three-step procedure per each time step: 1) the heat transfer equation is solved to obtain the temperature field; 2) the Poisson equation is solved; 3) Finally, the velocity field is obtained from Equation 3.5, for which a second order approximation is applied to calculate the pressure gradient.

The mathematical problem was also discretized using the finite volume numerical method (Versteeg & Malalasekera 1995). A first order fully implicit scheme was used for temporal discretization which is unconditionally stable. Likewise a central differencing scheme was applied to approximate the convective term in the heat transfer equation.

Discrete problem

The discretized equations for this mathematical problem are very similar to that for the 2D case. The integration of the heat transfer equation in a control volume P_P (Figure 3.2) using central differencing for the convective term and fully implicit discretization in time leads to the following algebraic equation:

$$a_P\theta_P = a_E\theta_E + a_W\theta_W + a_N\theta_N + a_S\theta_S + a_S\theta_F + a_S\theta_B + s_P, \tag{3.9}$$

with

$$a_E = \frac{A_e}{\delta x} - \frac{u_e A_e}{2}, \quad a_W = \frac{A_w}{\delta x} + \frac{u_w A_w}{2},$$

$$a_N = \frac{A_n}{\delta y} - \frac{v_n A_n}{2}, \quad a_S = \frac{A_s}{\delta y} + \frac{v_s A_s}{2},$$

$$a_F = \frac{A_f}{\delta z} - \frac{w_f A_f}{2}, \quad a_B = \frac{A_b}{\delta z} + \frac{w_b A_b}{2},$$

and

$$a_P = a_E + a_W + a_N + a_S + a_F + a_B + \frac{\Delta V}{\Delta t}, \quad s_P = \theta^0 \frac{\Delta V}{\Delta t}.$$

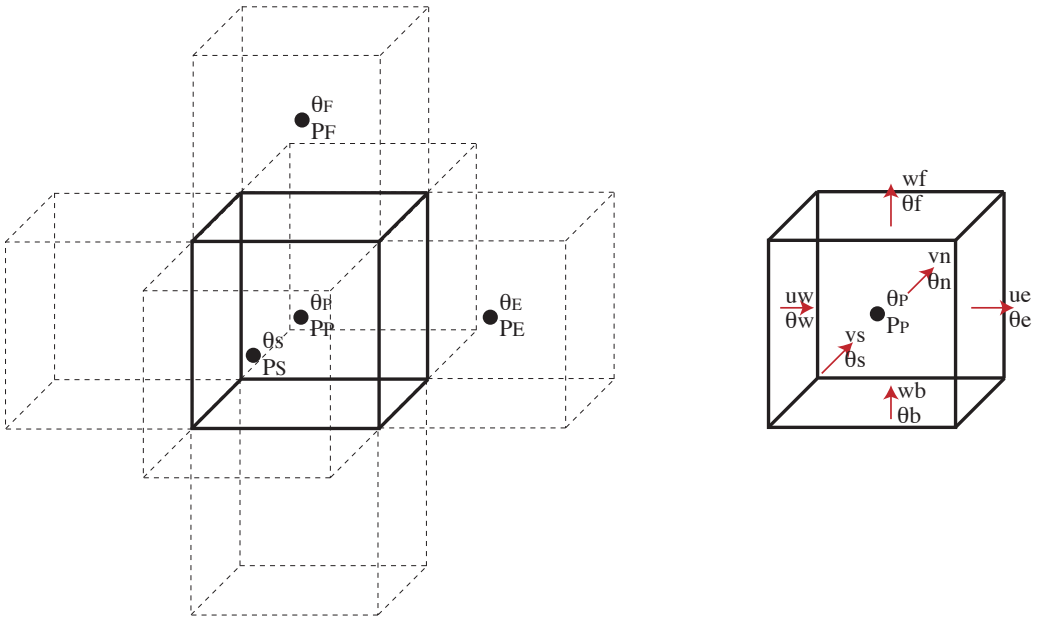

Figure 3.2: Three-dimensional mesh for the discrete primitive variables problem. Pressure and temperature are both calculated in the centers of the control volume. The velocities and temperatures of the coefficients of Equation 3.9 are calculated on the faces e, w, n, s, f, and b as shown on the right of the figure.

As in the 2D problem, the areas of the faces are constant in a uniform mesh: $A_e = A_w = A_n = A_s = A_f = A_b = \delta x \delta y = \delta x \delta z = \delta y \delta z$. The corrections to the coefficients of Equation 3.9 will be omitted here to avoid redundancy. The correction must be done as it was shown for the 2D problem considering whether the boundaries are Dirichlet or Neumann (Versteeg & Malalasekera 1995). In this case the Dirichlet boundaries are the top (F) and bottom (B) boundaries, whereas the east (E), west (W), north (N), and south (S) boundaries are adiabatic.

As regards the momentum equation, the integration of Equation 3.7 in the control volume P_P turns out to be

$$a_P P_P = a_E P_E + a_W P_W + a_N P_N + a_S P_S + a_F P_F + a_B P_B - s_P, \tag{3.10}$$

with

$$a_E = \frac{\Gamma_e A_e}{\delta x}, \quad a_W = \frac{\Gamma_w A_w}{\delta x}, \quad a_N = \frac{\Gamma_n A_n}{\delta y}, \quad a_S = \frac{\Gamma_s A_s}{\delta y},$$

$$a_F = \frac{\Gamma_f A_f}{\delta z}, \quad a_B = \frac{\Gamma_b A_b}{\delta z},$$

$$\Gamma = \frac{1}{Ra},$$

$$a_P = a_E + a_W + a_N + a_S + a_F + a_B.$$

It is important to notice that since $\Gamma = \frac{1}{Ra}$ is a constant then Γ calculated at each face of the control volume is simply $\frac{1}{Ra}$. The source term s_P (buoyancy term) is obtained as follows

$$\begin{aligned} s_P = \int_{CV} \left(\frac{\partial \theta}{\partial x} \sin\alpha + \frac{\partial \theta}{\partial y} \cos\alpha \right) dV &= \int_s^n \int_b^f \sin\alpha(\theta_e - \theta_w) dz dy \\ &+ \int_s^n \int_w^e \cos\alpha(\theta_n - \theta_s) dx dy \\ &= \sin\alpha(\theta_e - \theta_w)\delta z \delta y + \cos\alpha(\theta_n - \theta_s)\delta x \delta y. \end{aligned}$$

The implementation of the boundary control volumes can be obtained referring to the 2D case in Section 2.3.1.

3.3.2 Vector potential

The vector potential approach is the counterpart of the stream function approach implemented in the 2D problem. The solution algorithm is also based on the fixed point iteration. Pressure is eliminated from the momentum equation (Equation 3.5) by taking the curl. It is then assumed that there exists a vector potential, $\boldsymbol{\psi}$, such that $\mathbf{u} = \nabla \times \boldsymbol{\psi}$ and with the property $\nabla \cdot \boldsymbol{\psi} = 0$. So that the curl of Equation 3.5 leads to:

$$\nabla \times (\nabla \times \boldsymbol{\psi}) = Ra \nabla \times \theta \mathbf{e}. \tag{3.11}$$

Owing to the divergence-free property of $\boldsymbol{\psi}$, it can be simplified as

$$\nabla^2 \boldsymbol{\psi} = -Ra \nabla \times \theta \mathbf{e}. \tag{3.12}$$

The components of this equation are the following:

$$\begin{cases} \nabla^2 \psi_1 = -Ra \frac{\partial \theta}{\partial y} \cos\alpha, \\ \nabla^2 \psi_2 = Ra \left(\frac{\partial \theta}{\partial x} \cos\alpha - \frac{\partial \theta}{\partial z} \sin\alpha \right), \\ \nabla^2 \psi_3 = Ra \frac{\partial \theta}{\partial y} \sin\alpha. \end{cases} \tag{3.13}$$

The corresponding boundary conditions are:

$$\frac{\partial \psi_1}{\partial x} = \psi_2 = \psi_3 = 0, \quad \text{for} \quad x = 0 \quad \text{and} \quad x = D,$$

$$\frac{\partial \psi_2}{\partial y} = \psi_1 = \psi_3 = 0, \quad \text{for} \quad y = 0 \quad \text{and} \quad y = 1,$$
$$\frac{\partial \psi_3}{\partial z} = \psi_1 = \psi_2 = 0, \quad \text{for} \quad z = 0 \quad \text{and} \quad z = 1.$$

The problem given by Equations 3.4 and 3.13 and their boundary conditions is discretized using the Finite Volume numerical method. A central differencing scheme was also applied for the convective term of the heat transfer equation and a first-order fully implicit scheme was used for the temporal term.

Discrete problem

The discretization of the problem is carried out on a staggered grid for convenience (Figure 3.3). The starting point to discretize the problem are the equations in the form of the fixed point iteration (Section 2.4.1) as follows:

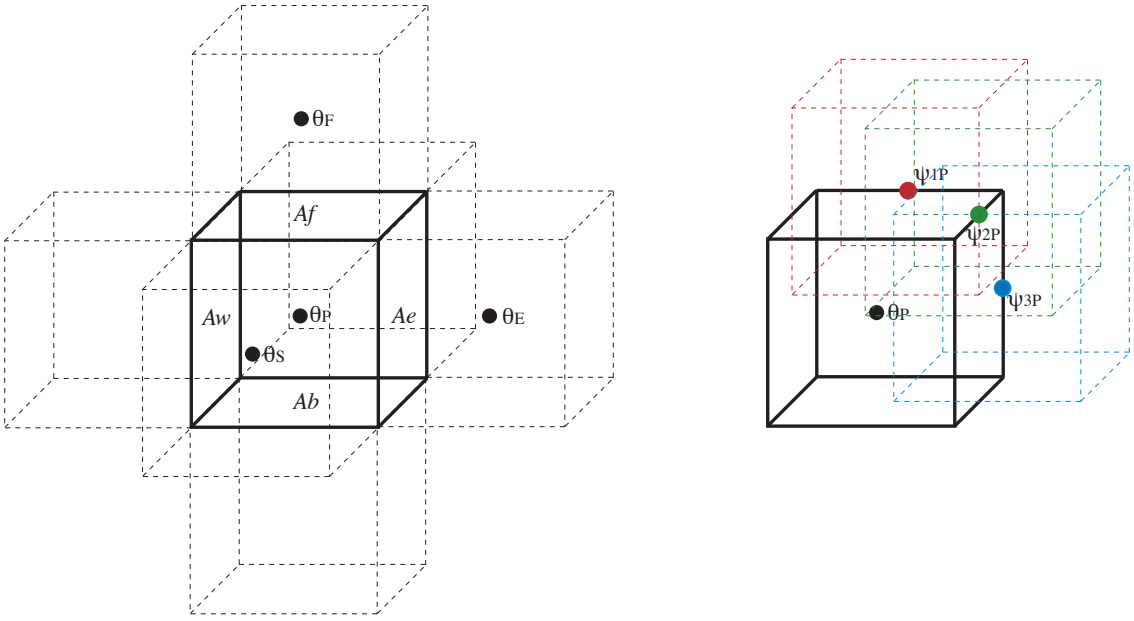

Figure 3.3: Three-dimensional staggered grid for the discrete vector potential problem. The main mesh, represented on the left hand side hosts the temperature control volumes calculated at the centers. The vector potential components are calculated on the edges of the temperature control volumes leading to three staggered grids as shown on the right of the figure.

$$L\theta^{m+1} = L\theta^m - \lambda\Upsilon(\theta^m, \psi^m), \tag{3.14}$$

$$\nabla^2\psi_1^{m+1} = -Ra\frac{\partial\theta^{m+1}}{\partial y}\cos\alpha, \tag{3.15}$$

$$\nabla^2\psi_2^{m+1} = Ra\left(\frac{\partial\theta^{m+1}}{\partial x}\cos\alpha - \frac{\partial\theta^{m+1}}{\partial z}\sin\alpha\right), \tag{3.16}$$

$$\nabla^2\psi_3^{m+1} = Ra\frac{\partial\theta^{m+1}}{\partial y}\sin\alpha. \tag{3.17}$$

These equations are solved following the algorithm shown in Figure 2.4 replacing accordingly the 3D form of the heat transfer equation and considering the three components of the vector potential. The integration of the heat transfer equation (Eq. 3.14) on a control volume θ_P turns out

$$\begin{aligned} &a_P\theta_P^{m+1} - a_E\theta_E^{m+1} - a_W\theta_W^{m+1} - a_N\theta_N^{m+1} - a_S\theta_S^{m+1} - a_F\theta_N^{m+1} - a_B\theta_S^{m+1} = \\ &a_P\theta_P^m - a_E\theta_E^m - a_W\theta_W^m - a_N\theta_N^m - a_S\theta_S^m - a_F\theta_N^m - a_B\theta_B^m \\ &- \lambda(b_P\theta_P^m - b_E\theta_E^m - b_W\theta_W^m - b_N\theta_N^m - b_S\theta_S^m - b_F\theta_F^m - b_B\theta_B^m + s_P). \end{aligned} \tag{3.18}$$

with

$$a_E = \frac{A_e}{\delta x}, \quad a_W = \frac{A_w}{\delta x}, \quad a_N = \frac{A_n}{\delta y}, \quad a_S = \frac{A_s}{\delta y}, \quad a_F = \frac{A_f}{\delta z}, \quad a_B = \frac{A_b}{\delta z},$$

$$a_P = a_E + a_W + a_N + a_S + a_F + a_B + \frac{\Delta V}{\Delta t},$$

$$b_E = \frac{A_e}{\delta x} - \frac{u_e^m A_e}{2}, \quad b_W = \frac{A_w}{\delta x} + \frac{u_w^m A_w}{2},$$

$$b_N = \frac{A_n}{\delta y} - \frac{v_n^m A_n}{2}, \quad b_S = \frac{A_s}{\delta y} + \frac{v_s^m A_s}{2},$$

$$b_F = \frac{A_f}{\delta z} - \frac{w_f^m A_f}{2}, \quad b_B = \frac{A_b}{\delta z} + \frac{w_b^m A_b}{2},$$

$$b_P = b_E + b_W + b_N + b_S + b_F + b_B + \frac{\Delta V}{\Delta t}, \quad s_P = -\theta^0\frac{\Delta V}{\Delta t}.$$

And from the definition of the vector potential $\mathbf{u} = \nabla \times \boldsymbol{\psi}$

$$u = \left(\frac{\partial\psi_2}{\partial y} - \frac{\partial\psi_3}{\partial z}\right),$$

$$v = \left(\frac{\partial \psi_1}{\partial z} - \frac{\partial \psi_2}{\partial x} \right),$$

$$w = \left(\frac{\partial \psi_3}{\partial x} - \frac{\partial \psi_1}{\partial y} \right).$$

The correction of the coefficients for the boundary control volumes are made following the criterion that was discussed in Chapter 2. The momentum equation consists of a Poisson equation for each component of the vector potential, differing only in the source term. Each equation is integrated in its corresponding control volume ψ_{1P}, ψ_{2P}, and ψ_{3P} (Fig. 3.3). The discrete form of these equations for internal control volumes has the general form (boundary control volumes are treated as shown in the previous chapter):

$$a_P \psi_P^{m+1} = a_E \psi_E^{m+1} + a_W \psi_W^{m+1} + a_N \psi_N^{m+1} + a_S \psi_S^{m+1} + a_F \psi_F^{m+1} + a_B \psi_B^{m+1} - s_P, \quad (3.19)$$

with

$$a_E = \frac{A_e}{\delta x}, \quad a_W = \frac{A_w}{\delta x}, \quad a_N = \frac{A_n}{\delta y}, \quad a_S = \frac{A_s}{\delta y}, \quad a_F = \frac{A_f}{\delta z}, \quad a_B = \frac{A_b}{\delta z},$$

$$a_P = a_E + a_W + a_N + a_S + a_B + a_F.$$

The source term (s_{P1}) for ψ_1 is

$$s_{P1} = \int_{CV} \left(-Ra \frac{\partial \theta^{m+1}}{\partial y} \cos\alpha \right) dV = -Ra \cos\alpha (\theta_n^{m+1} - \theta_s^{m+1}) \delta x \delta z.$$

The source term for ψ_2 is

$$\begin{aligned} s_{P2} &= \int_{CV} Ra \left(\frac{\partial \theta^{m+1}}{\partial x} \cos\alpha - \frac{\partial \theta^{m+1}}{\partial z} \sin\alpha \right) dV = \\ &\int_b^f \int_s^n \cos\alpha (\theta_e^{m+1} - \theta_w^{m+1}) dy dz - \int_s^n \int_w^e \sin\alpha (\theta_f^{m+1} - \theta_b^{m+1}) dx dy \\ &= \cos\alpha (\theta_e^{m+1} - \theta_w^{m+1}) \delta y \delta z - \sin\alpha (\theta_f^{m+1} - \theta_b^{m+1}) \delta x \delta y. \end{aligned}$$

Finally, the discrete source term for ψ_3 is

$$s_{P3} = \int_{CV} \left(Ra \frac{\partial \theta^{m+1}}{\partial y} \sin\alpha \right) dV = Ra \sin\alpha (\theta_n^{m+1} - \theta_s^{m+1}) \delta x \delta z.$$

3.4 Numerical results and discussion

The determination of the steady state was carried out as in the 2D case, by means of the evaluation of the convergence of the temperature matrix. The infinity norm of the difference $L_\infty = |\boldsymbol{\theta}^t - \boldsymbol{\theta}^{t-1}|_\infty$ was calculated for successive time steps over a long time interval that proved to be long enough after several tests ($t_{int} = 4.4$). The convergence criterion was defined according to the condition $\langle L_\infty \rangle_{t_{int}} < 5 \times 10^{-7}$, where $\langle L_\infty \rangle_{t_{int}}$ is the average infinity norm over the time interval t_{int}. Both algorithms were implemented in Fortran 90 and a Gauss-Seidel iteration was employed for the solution of the resulting system of algebraic equations.

3.4.1 Validation

The numerical models were validated considering a horizontal cubic cavity ($D = 1$ and $\alpha = 0$). The models were tested just above the critical Rayleigh number ($Ra_c = 39.48$); for this particular test no convergence criterion was used. Instead, a long simulation time was applied ($t = 60$) until significant evidence of convection was detected. Table 3.1 shows the steady-state Nusselt number, both models presented convection at $Ra = 41$ using a coarse mesh defined as $\Delta x = \Delta y = \Delta z = 25^{-1}$. With a finer mesh however ($\Delta x = \Delta y = \Delta z = 50^{-1}$.) the primitive variables model remained conductive ($Nu \simeq 1$). The steady-state convective modes in all these cases were characterized by a single 2D convective cells.

As regards the time step of these simulations, the optimum time step for the primitive variables model using fine mesh was smaller (10 times) than the other cases studied. The fine mesh primitive variables model required $\Delta t = 2 \times 10^{-5}$ to generate numerically stable results, whereas a time step $\Delta t = 2 \times 10^{-4}$ was suitable in the other cases.

Table 3.1: Nusselt number for a cubic porous enclosure considering two mesh sizes.

		Nu	
Mesh size	Ra	Primitive variables	Vector potential
$\Delta x = 25^{-1}$	40	0.999	0.999
	41	1.070	1.058
$\Delta x = 50^{-1}$	40	1.000	1.000
	41	1.000	1.061
$\Delta x = 25^{-1}$	60	1.773	1.773
	120	2.934	2.934
$\Delta x = 50^{-1}$	60	1.778	1.778
	120	2.945	2.945

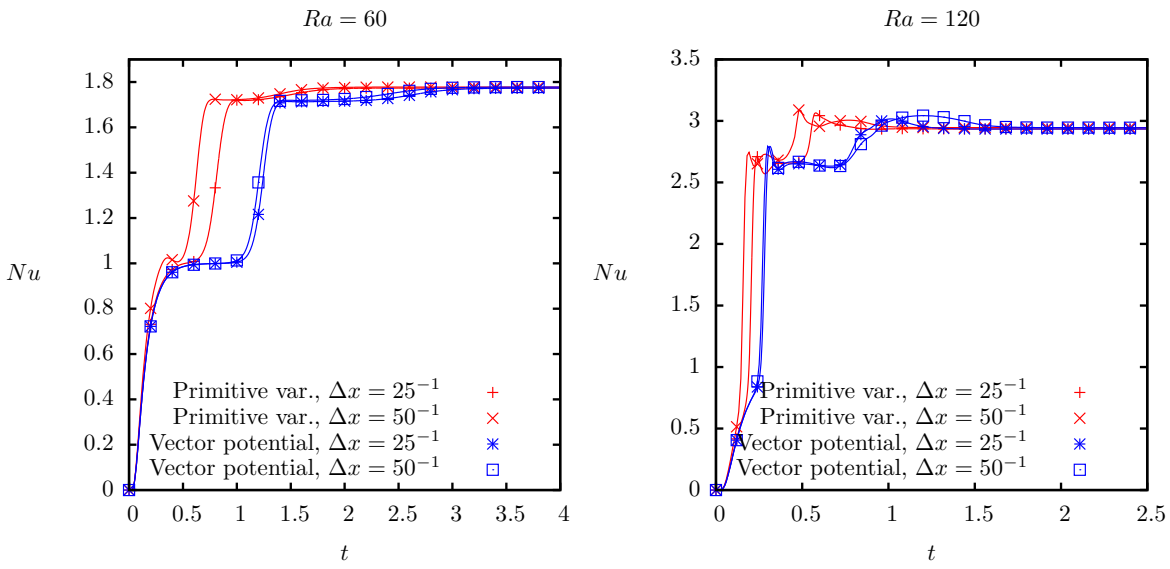

Figure 3.4: Nusselt number as a function of time for primitive variables and vector potential models using two different mesh sizes ($\Delta x = 25^{-1}$ and $\Delta x = 50^{-1}$).

The steady-state Nusselt number was more consistent between the two models when higher Rayleigh numbers were examined. Table 3.1 shows that identical results were obtained with both models. However, the evolution towards the steady state was different. As shown in Figure 3.4, primitive variables reaches the steady state sooner than vector potential. This fast-convergence effect is increased when using a fine mesh in primitive variables (with the associated smaller time step $\Delta t = 2 \times 10^{-5}$). It is important to note that the fast convergence of the primitive variables in comparison with vector potential is observed even when the same time-step is used, such is the case of the coarse-mesh results. So that the reason why primitive variables converges faster than vector potential is probably due to a different way in which round-off errors are propagated in the numerical solution rather than time-step effects.

Due to the non-iterative solution of the momentum equation in primitive variables, the divergence-free condition of the velocity field is satisfied more weakly than in vector potential. In most cases observed in this study for primitive variables, the maximum value of the divergence of the velocity field ($\nabla \cdot \mathbf{u}$) in each time step was order 10^{-3} whereas for vector potential was closer to zero, with values order 10^{-7}. This difference in the way the divergence-free condition is satisfied might explain the difference in the speed of convergence of the two methods. In support of this observation, it is important to mention that the finest mesh for primitive variables (the fastest convergence) was also the case study with the highest numerical approximation error in the divergence-free condition ($\sim 10^{-3}$ in each time step). This case was not numerically stable for a higher time step ($\Delta t = 2 \times 10^{-4}$) which led to errors in the divergence-free condition order 10^{-1} and higher.

Although the models proved a good match with the steady-state results for moderate

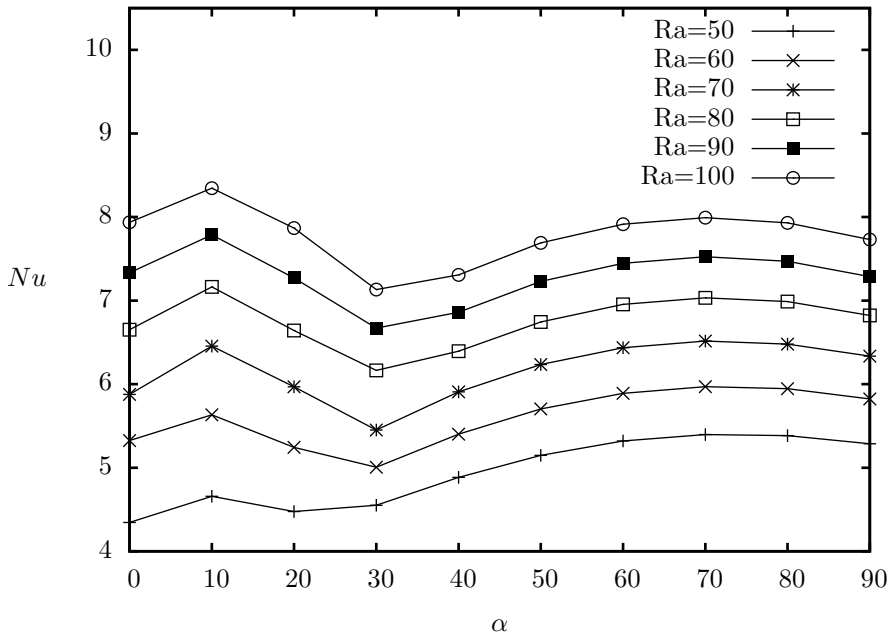

Figure 3.5: Steady state Nusselt number vs slope angle for an aspect ratio $D = 3$.

Rayleigh numbers, the vector potential algorithm was chosen for further 3D modeling on the basis that the primitive variables approach displays a higher dependency on the mesh size and demands a longer computing time when dealing with fine meshes, since the time step required is an order of magnitude smaller.

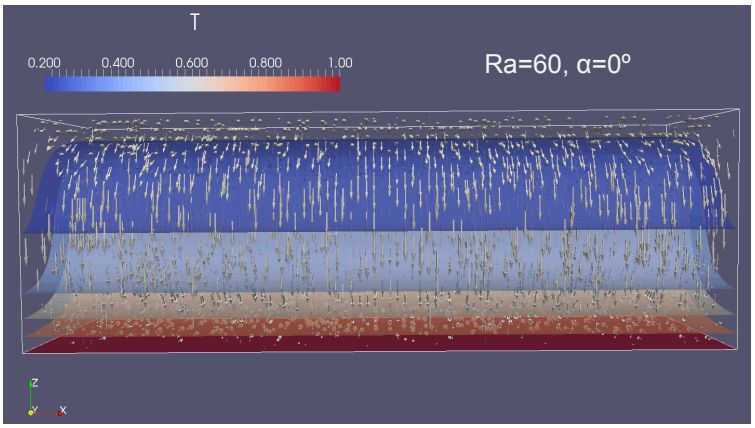

Figure 3.6: Longitudinal coil characteristic of $\alpha = 0$ and $D = 3$ with $Ra \leq 60$.

3.4.2 Sloping porous enclosure with aspect ratio $D = 3$

Figure 3.5 shows the global Nusselt number as a function of the slope angle for a set of Rayleigh numbers and an aspect ratio $D = 3$, local Nusselt maxima are shown in Table 3.2. Regarding the horizontal case ($\alpha = 0$), three different convective regimes were observed: a longitudinal coil (Figure 3.6) for moderate Rayleigh numbers ($Ra \leq 60$),

transverse rolls for $Ra \geq 63$ (Figure 3.7), and the transition between these convective modes for $Ra = 61$ to 62. The transverse rolls regime was characterized either by three or four cells depending on the Rayleigh number, three cells were observed up to $Ra = 65$ and four cells for higher Ra. The transition between longitudinal coil and transverse rolls for the horizontal box is characterized by an interaction of these convective modes as shown in Figure 3.8. For this particular case the simulation time required to reach the steady state was $t_{ss} = 9.1$. An additional simulation was carried out for further confirmation of this result using a long simulation time ($t = 60$) without a convergence criterion. The result was the same with a negligible difference in the Nusselt number ($\sim 0.02\%$), this supports the selection of the convergence criterion used to define the steady convection of the system.

Table 3.2: Local Nusselt maxima for a 3D porous enclosure with aspect ratio $D = 3$. The angle α at which the maximum is located is given beside each local maximum.

	Local Nu maximum	
Ra	$0° \leq \alpha \leq 30°$	$30° < \alpha \leq 90°$
50	4.66 ($\alpha = 10°$)	5.39 ($\alpha = 70°$)
60	5.63 ($\alpha = 10°$)	5.97 ($\alpha = 70°$)
70	6.45 ($\alpha = 10°$)	6.51 ($\alpha = 70°$)
80	7.16 ($\alpha = 10°$)	7.03 ($\alpha = 70°$)
90	7.78 ($\alpha = 10°$)	7.52 ($\alpha = 70°$)
100	8.34 ($\alpha = 10°$)	7.99 ($\alpha = 70°$)

As regards the sloping porous enclosure ($\alpha \neq 0$), a local maximum can be identified at $\alpha = 10°$ (Figure 3.5), which is absolute for $Ra = 80$ and higher (Table 3.2). At this angle the convective flow is characterized by three transverse rolls for every Rayleigh number from 50 to 100 (Figure 3.9). A summary of results is presented in Table 3.3. As the angle is increased there is a transition to a single cell regime. Initially, at

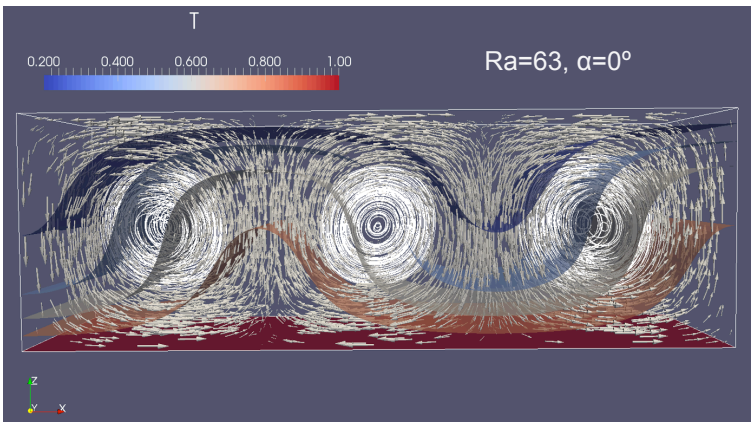

Figure 3.7: Transverse rolls convective mode for $D = 3$ and $\alpha = 0$. As presented in Table 3.3, up to 4 cells were observed at higher Rayleigh numbers.

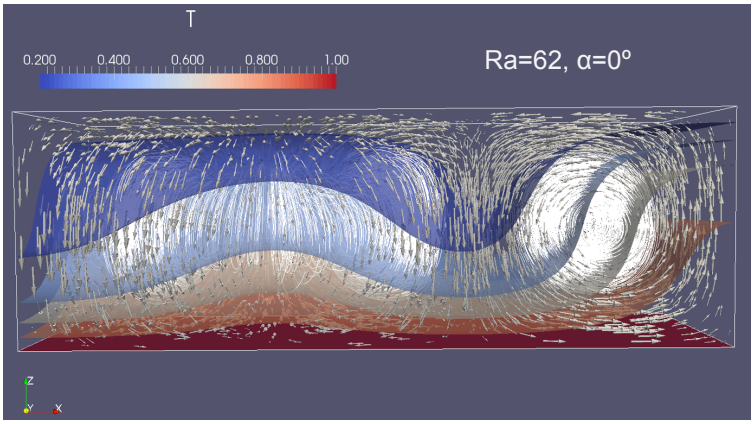

Figure 3.8: Convective mode characteristic of the transition between the longitudinal coil and transverse rolls for $D = 3$ and $\alpha = 0$.

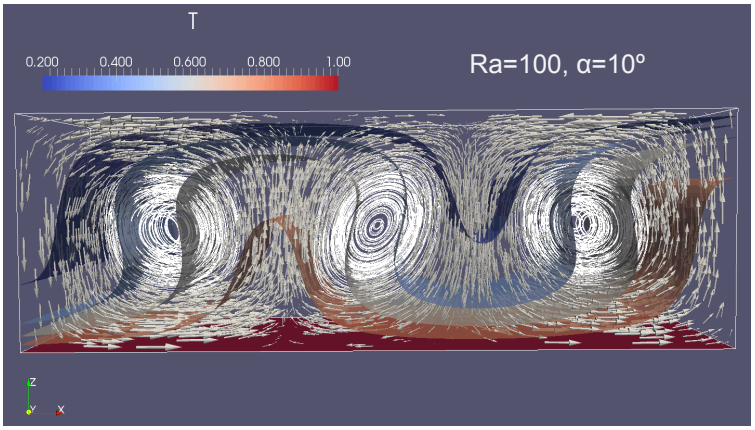

Figure 3.9: transverse rolls convective mode for $D = 3$, $Ra = 100$, and $\alpha = 10°$. This convective mode provides the maximum heat transfer rate ($Nu = 8.344$) for the parameters considered (Figure 3.5).

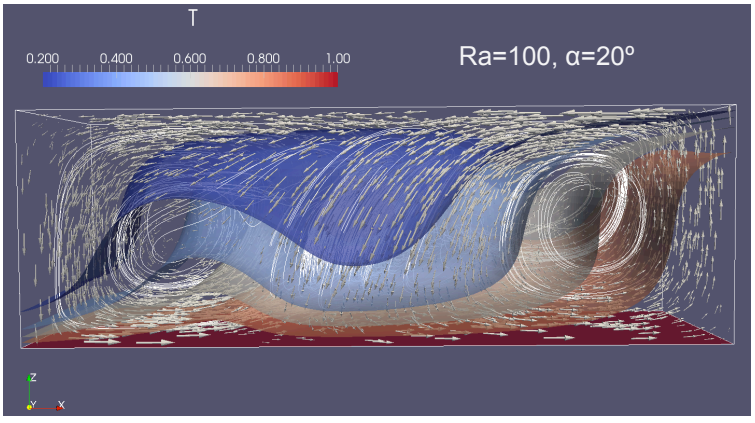

Figure 3.10: 3D velocity field distribution characteristic of the transition between transverse rolls and single cell convective modes for an aspect ratio $D = 3$.

$\alpha = 20°$, all the cases analyzed undergo a complex 3D velocity distribution (Figure 3.10) characterized by the interaction of two transverse rolls with a longitudinal coil located in the center of the box. This convective mode is accompanied by a decrease

Table 3.3: Convective modes and transition angles for the selected cases.

D	Ra	α	Convective mode	Nu	t_{ss}
3	50	0	longitudinal coil	4.345	9.06
		1	3 transverse rolls	4.399	5.29
		17	transverse rolls with a longitudinal coil	4.507	13.11
		22	external cell with 2 internal secondary cells	4.392	5.16
	100	0	4 transverse rolls	7.936	8.02
		1	5 transverse rolls	7.438	5.39
		6	3 transverse rolls	8.194	19.73
		11	transverse rolls with a longitudinal coil	8.090	14.51
		32	external cell with 2 internal secondary cells	6.871	4.86
5	50	0	longitudinal coil	7.242	9.03
		1	5 transverse rolls	7.295	6.04
		14	transverse rolls with a longitudinal coil	7.264	15.32
		30	external cell with 2 internal secondary cells	6.600	5.09
	100	0	7 transverse rolls	13.119	12.93
		9	partial rotation of transverse rolls	12.905	19.92
		11	transverse rolls with a longitudinal coil	13.263	11.09
		50	single cell	9.846	4.88
10	50	0	transverse rolls with a longitudinal coil	14.336	11.89
		1	11 transverse rolls	14.379	8.50
		10	transverse rolls with a longitudinal coil	14.353	30.76
		30	external cell with 2 internal secondary cells	11.602	4.62
	100	0	14 transverse rolls	26.196	32.78
		1	15 transverse rolls	25.775	8.62
		7	13 transverse rolls	26.656	14.45
		10	partial rotation of transverse rolls	25.493	22.34
		14	transverse rolls with a longitudinal coil	26.092	15.46

in the Nusselt number and is consistent with the observations by Caltagirone & Bories (1985) who reported an interaction of transverse and longitudinal coils for relatively

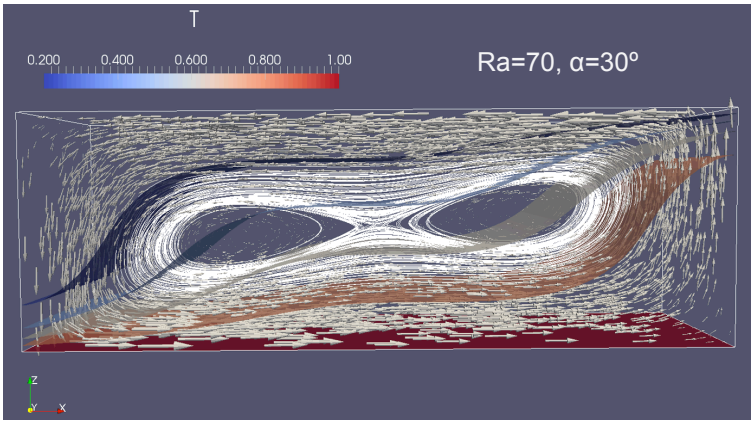

Figure 3.11: 2D convective mode characteristic of the transition to single-cell convection. The minimum Nusselt number was associated with this convective mode for $Ra = 60$ and higher.

small slope angles. When the angle is further increased, the convective regime reaches a 2D velocity distribution composed by an external cell with two internal secondary cells (Figure 3.11). This convective mode was obtained in our 2D study and it has also been described by Báez & Nicolás (2006), however, the 3D modeling presented in this chapter shows that the transition to this convective mode occurs for a higher α, due to the irregular 3D convective mode that is preceding ($\alpha = 20°$). Furthermore the associated Nu to this irregular convective mode is lower than that for the the multicellular flow ($\alpha = 10°$), so that the local maxima in the interval $0° \leq \alpha \leq 30°$ in the 3D model is located at $\alpha = 10°$ for all Ra unlike the 2D model (Table 2.2). Finally, at $\alpha = 50°$ the convective modes become single cell (Figure 3.12) with a maximum Nusselt located at $\alpha = 70°$ in agreement with the 2D results.

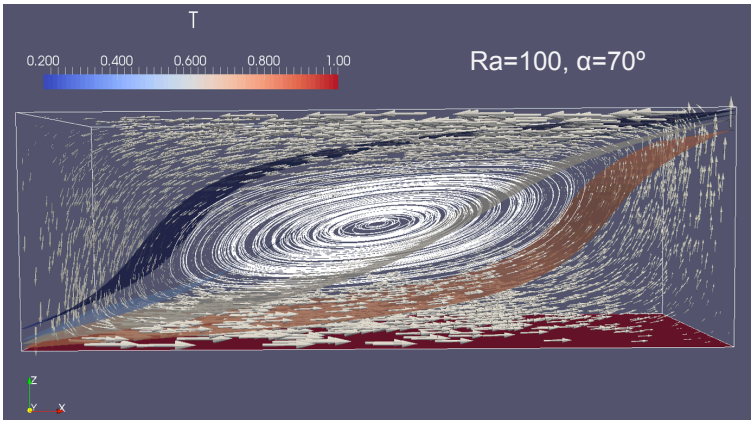

Figure 3.12: Single cell convective mode for $D = 3$ characteristic of high slope angles.

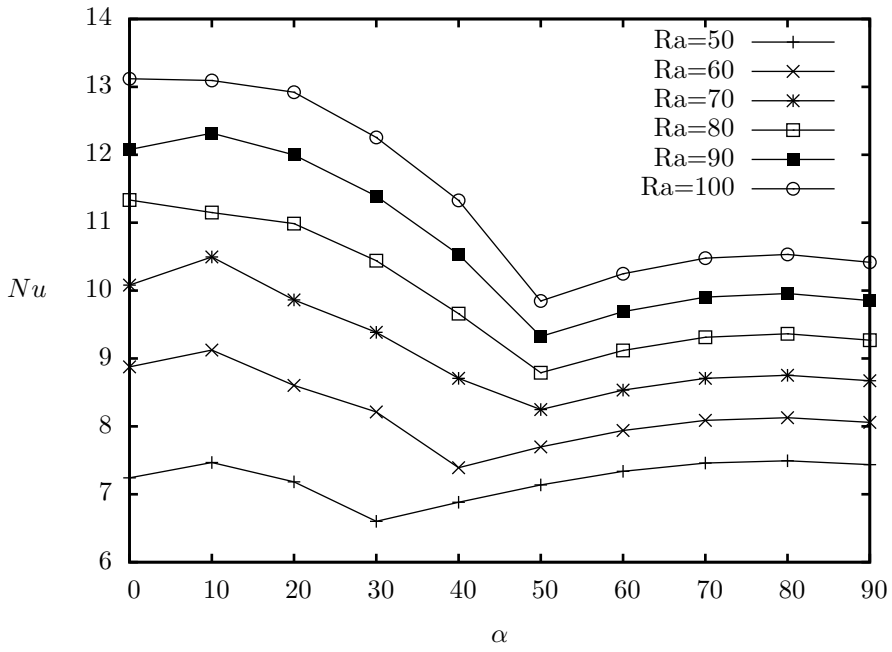

Figure 3.13: Steady state Nusselt number vs slope angle for an aspect ratio $D = 5$.

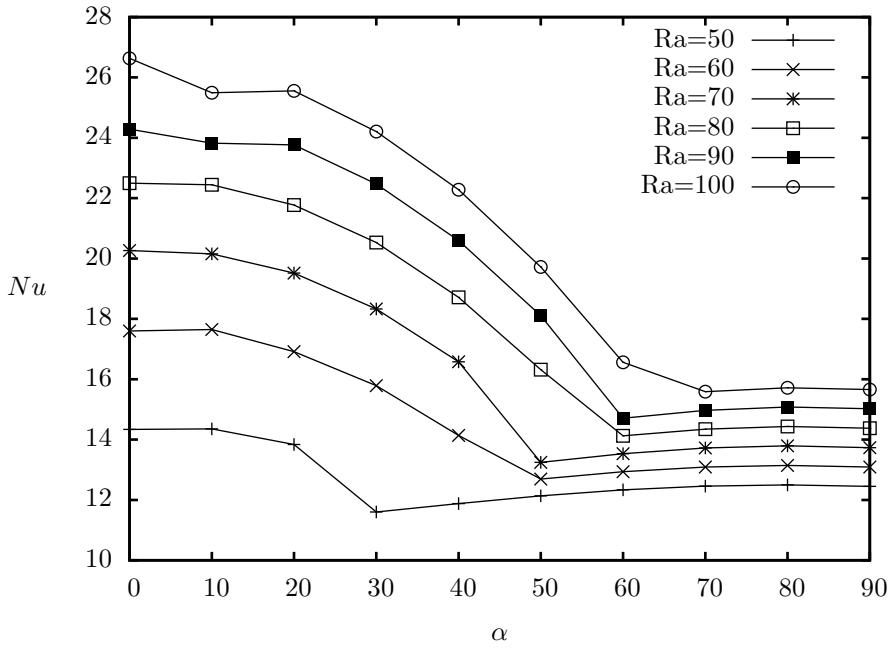

Figure 3.14: Steady state Nusselt number vs slope angle for an aspect ratio $D = 10$.

Table 3.4: Local Nusselt maxima for a 3D porous enclosure with aspect ratio $D = 5$. The angle α at which the maximum is located is given beside each local maximum.

	Local Nu maximum	
Ra	$0° \leq \alpha \leq 30°$	$30° < \alpha \leq 90°$
50	7.46 ($\alpha = 10°$)	7.49 ($\alpha = 80°$)
60	9.12 ($\alpha = 10°$)	8.13 ($\alpha = 80°$)
70	10.49 ($\alpha = 10°$)	8.75 ($\alpha = 80°$)
80	11.33 ($\alpha = 0$)	9.36 ($\alpha = 80°$)
90	12.31 ($\alpha = 10°$)	9.95 ($\alpha = 80°$)
100	13.11 ($\alpha = 0$)	10.53 ($\alpha = 80°$)

Table 3.5: Local Nusselt maxima for a 3D porous enclosure with aspect ratio $D = 10$. The angle α at which the maximum is located is given beside each local maximum.

	Local Nu maximum	
Ra	$0° \leq \alpha \leq 30°$	$30° < \alpha \leq 90°$
50	14.35 ($\alpha = 10°$)	12.49 ($\alpha = 80°$)
60	17.64 ($\alpha = 10°$)	13.14 ($\alpha = 80°$)
70	20.26 ($\alpha = 0$)	13.79 ($\alpha = 80°$)
80	22.49 ($\alpha = 0$)	14.43 ($\alpha = 80°$)
90	24.28 ($\alpha = 0$)	15.07 ($\alpha = 80°$)
100	26.63 ($\alpha = 0$)	15.71 ($\alpha = 80°$)

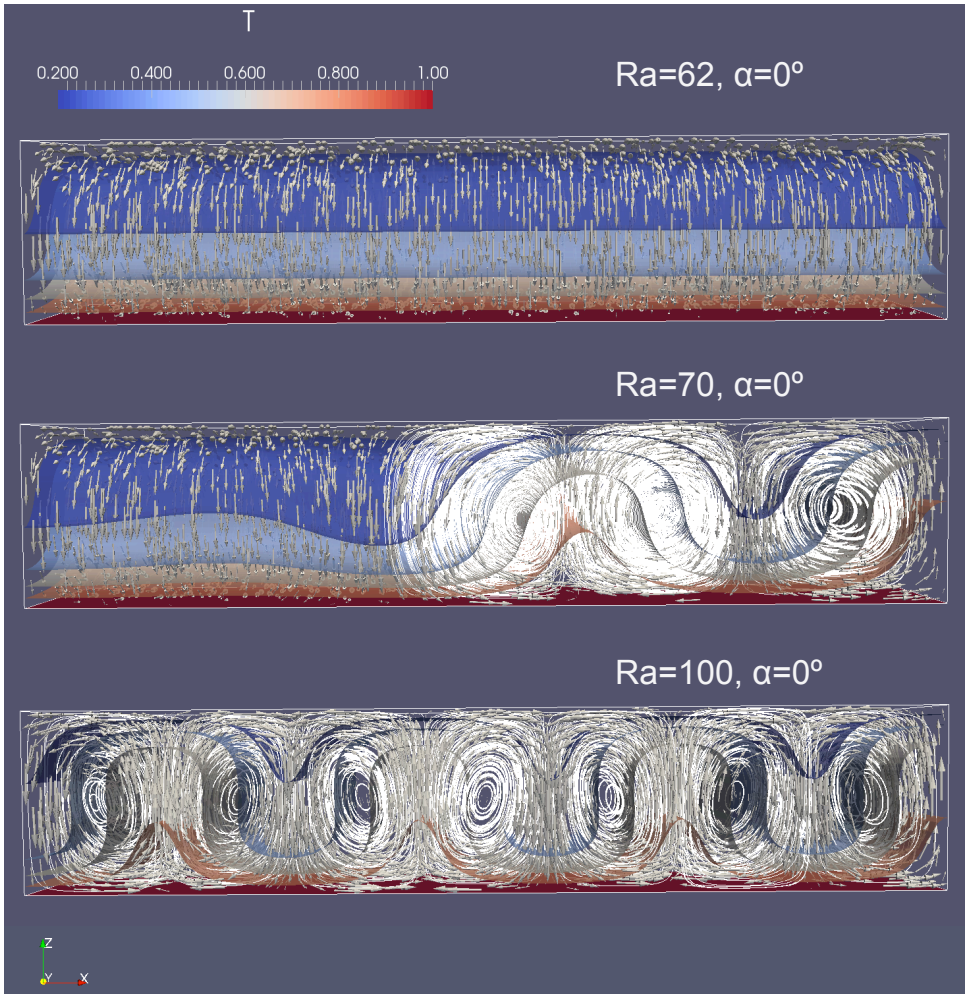

Figure 3.15: Convective modes characteristic of a horizontal porous enclosure with $D = 5$. As the Rayleigh number is increased the longitudinal coil regime becomes multicellular.

3.4.3 High aspect ratio porous enclosures $D = 5$ and $D = 10$

The parametric study for the aspect ratios $D = 5$ and 10 is shown in Figures 3.13 and 3.14, respectively. These figures show that the difference in the Nusselt number at small and large angles increases with the aspect ratio. This is due to the fact that a larger number of convective cells can be hosted in the transverse rolls regime characteristic of small slope angles, the multiplication of upwellings and downwellings enhances the heat transfer rate throughout the cavity. Firstly, let us discuss the horizontal case ($\alpha = 0$) for $D = 5$. A longitudinal coil was observed at this aspect ratio for $Ra \leq 62$ (Figure 3.15), which is characterized by a high up-flow and down-flow areas in comparison with the single cell regime characteristic of high α; for this reason the Nusselt number turns out to be higher even for moderate Ra (see for instance $Ra = 60$, Figure 3.13). The transition to transverse rolls in the horizontal case starts at $Ra = 63$ with an interaction of a longitudinal coil and transverse rolls. Unlike $D = 3$ this convective mode proved to be steady for a wider range of Rayleigh

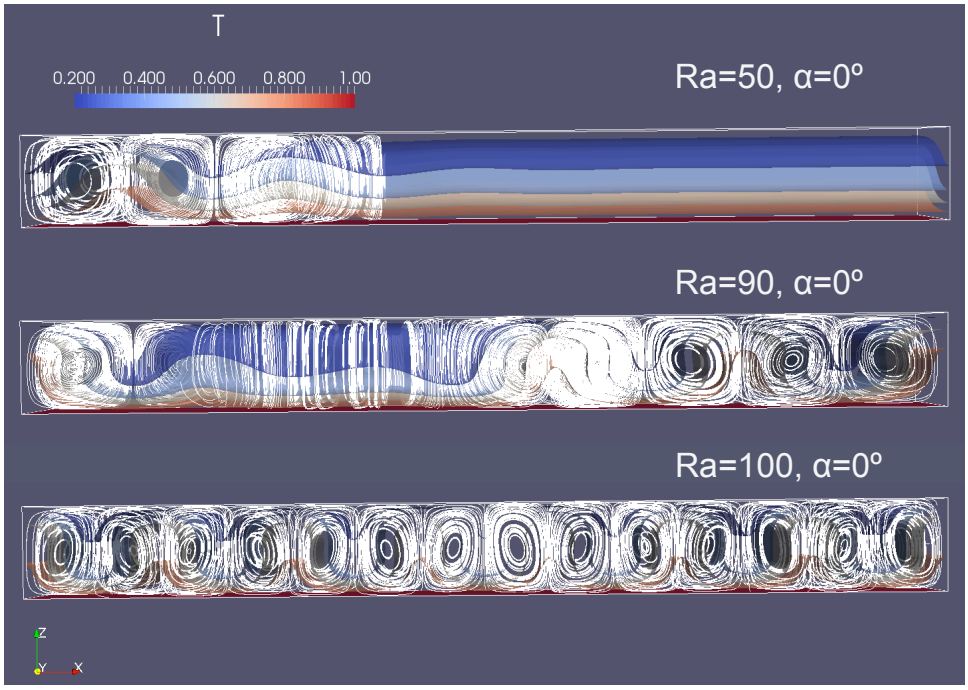

Figure 3.16: Convective modes characteristic of a horizontal porous enclosure with $D = 10$. A purely longitudinal coil was not attained for this aspect ratio for the Rayleigh numbers considered.

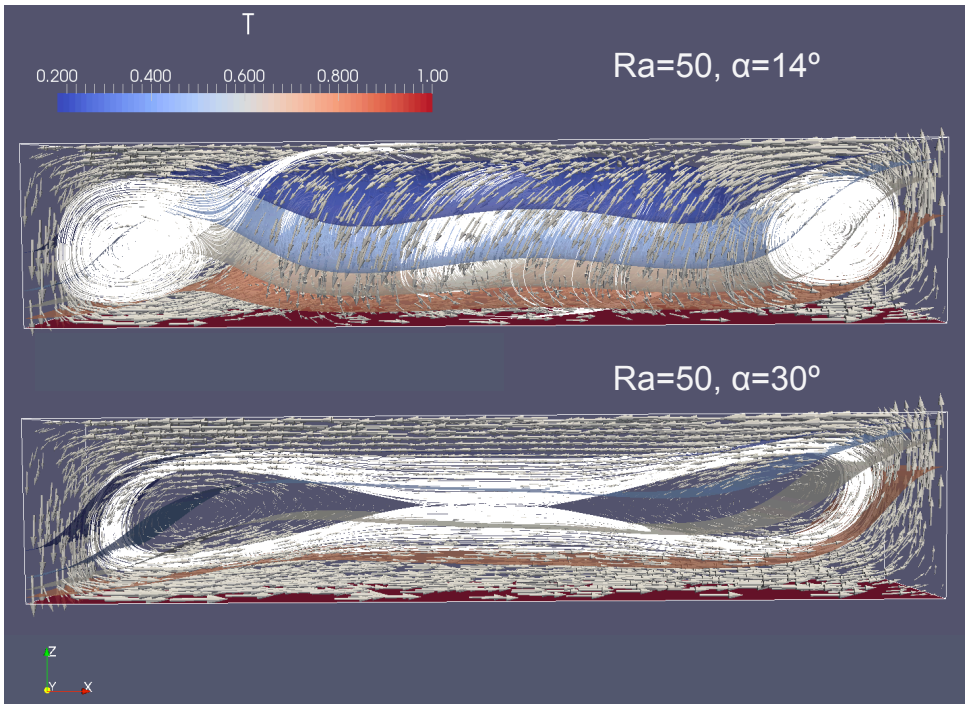

Figure 3.17: Steady state convective modes for $D = 5$ and $Ra = 50$. $\alpha = 14°$ and $\alpha = 30°$ represent transition angles (Table 3.3).

numbers, $Ra = 70$ was characterized by the same convective mode and transverse rolls were only observed at $Ra = 80$ and higher (Figure 3.15). On the other hand, as regards the horizontal case for the aspect ratio $D = 10$, the steady state was

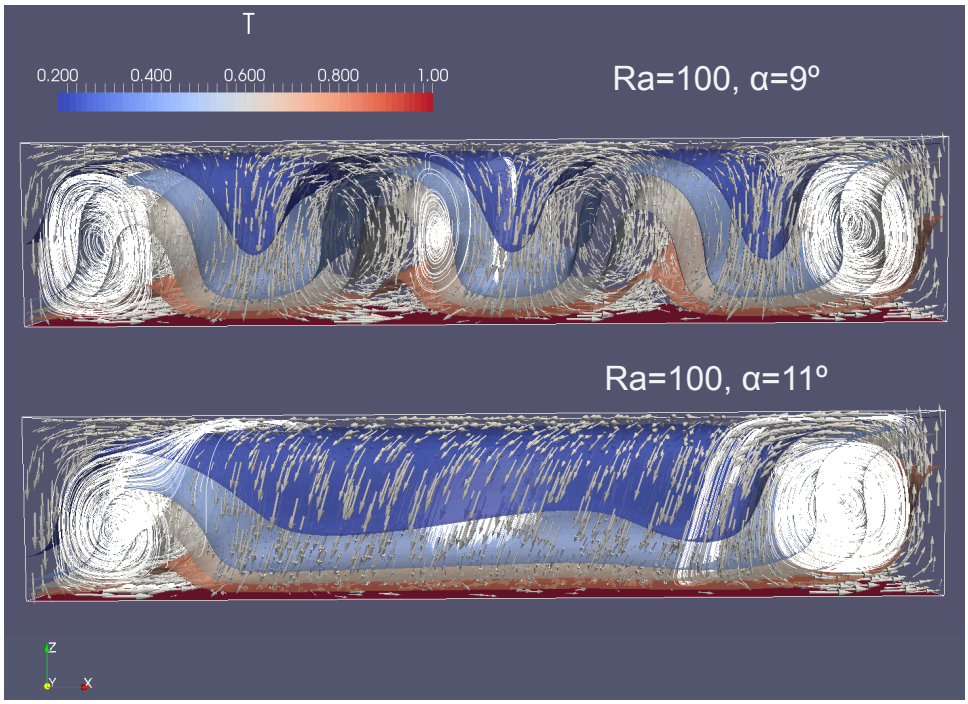

Figure 3.18: Steady state convective modes for $D = 5$ and $Ra = 100$. $\alpha = 9°$ and $\alpha = 11°$ are transition angles for $Ra = 100$ (Table 3.3).

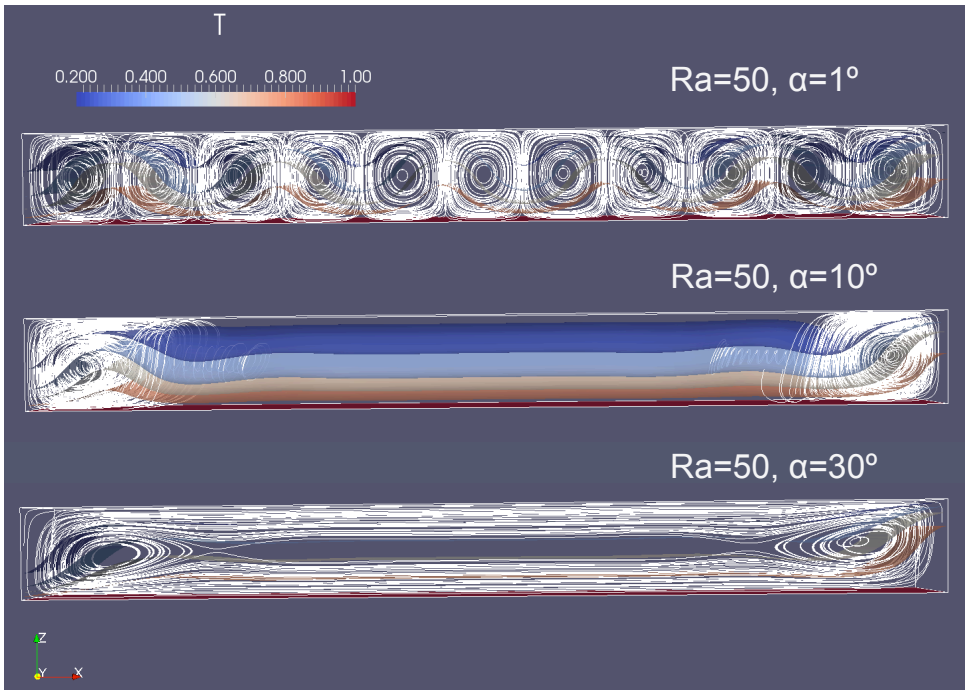

Figure 3.19: Steady state convective modes for $D = 10$ and $Ra = 50$ at the transition angles (Table 3.3).

characterized either by the interaction of longitudinal coil and transverse rolls or by a fully transverse rolls regime (Figure 3.16). Similar arguments apply to explain the high Nusselt number of these cases. It is interesting to observe that some of the local Nusselt maxima were located at $\alpha = 0$ (Tables 3.4 and 3.5) and for Rayleigh numbers

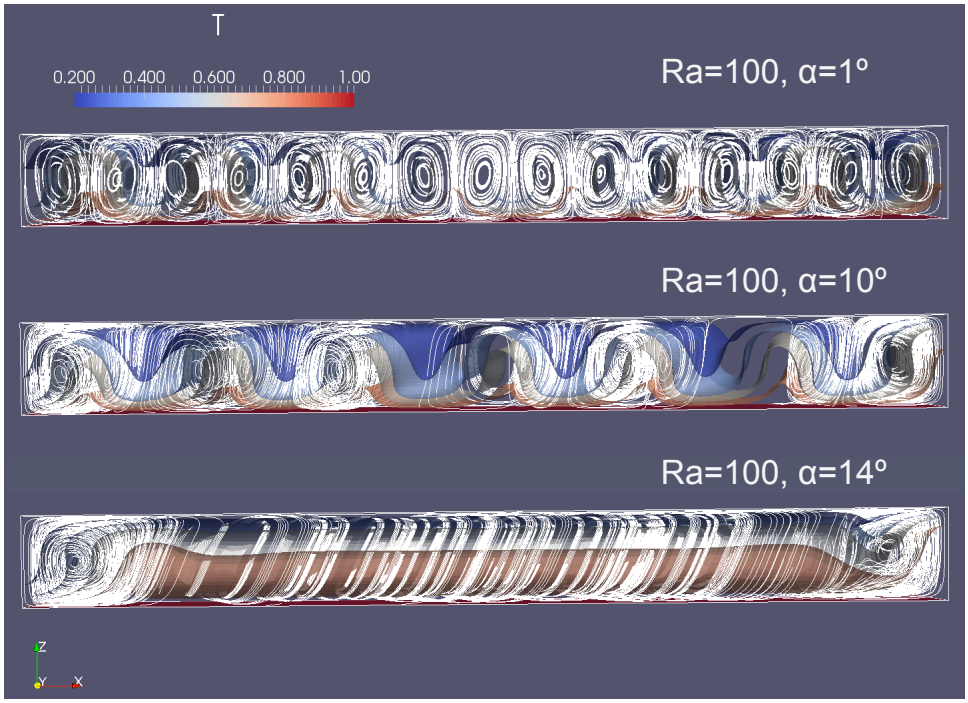

Figure 3.20: Steady state convective modes for $D = 10$ and $Ra = 100$ at the transition angles (Table 3.3).

as high as $Ra = 100$, which was not observed in out 2D results.

Considering the sloping case for $D = 5$ at $Ra = 50$, three transition angles were identified: $\alpha = 1°$, $\alpha = 14°$, and $\alpha = 30°$ (Figure 3.17, Table 3.3). The transition in the convective mode was characterized by a gentle variation in the Nusselt number with the maximum at $\alpha = 80°$ (Table 3.4) in response to the low Rayleigh number of the system. At $Ra = 100$, on the other hand, the maximum Nusselt number corresponds to $\alpha = 0$, which is transverse rolls convection. The transition to single-cell convection starts at $\alpha = 9°$, with a partial rotation of the cells located in the center of the cavity (Figure 3.18-upper), this rotation leads to the coalescence of these cells giving rise to a longitudinal coil that interacts with transverse rolls ($\alpha = 11°$). Single-cell convection is finally attained at $\alpha = 50°$ after a steep decrease in the Nusselt number.

Similarly, three transition angles were identified for $D = 10$ and $Ra = 50$: $\alpha = 1°$, $\alpha = 10°$, and $\alpha = 30°$, that correspond to transverse rolls, mixed transverse rolls with a longitudinal coil, and single cell with secondary cells, respectively (Figure 3.19). At $Ra = 100$ the convective mode remains multicellular until $\alpha = 10°$ (Figure 3.20). At this angle the transition to single cell starts in the same manner as $D = 5$, the innermost cells coalesce to give rise to a longitudinal coil that interacts with two remaining 2D rolls. For the space of parameters analyzed, the steady-state velocity field is no longer two-dimensional until $\alpha = 70°$, where the flow is single cell.

3.5 Conclusion

Three dimensional numerical simulations were carried out for the study of free convention in sloping porous enclosures in three dimensions. Two different approaches to solve the problem were compared: primitive variables and vector potential. In general terms, both models are suitable to study this problem. However, some limitations were identified in the primitive variables approach. Regarding the sensitivity of the model to the critical Rayleigh number for the onset of convection, it appeared that both models were equally sensitive to the Ra_c when using coarse meshes. When fine meshes were used however, the primitive variables model remained mainly conductive for $Ra = 41$, which is above the critical limit, whereas the vector potential solution was clearly convective. Furthermore, the time step required by primitive variables with a fine mesh was considerably smaller than the time step needed for vector potential, which results in a longer computing time for equivalent simulations. It was also observed that the primitive variables model produced mesh-dependent results, whereas vector potential was mesh independent.

A parametric study for moderate Rayleigh numbers (between 50 and 100) in a sloping porous enclosure permitted us to identify steady-state convective modes overlooked by 2D analysis, such as longitudinal coils in the horizontal case and mixed longitudinal coils with transverse rolls, which was observed at Rayleigh numbers as low as 50. As consequence of the presence of this irregular convective mode, the angles at which the local maximum Nusselt number is located for moderate α are not necessarily the same for 2D and 3D modeling. A purely longitudinal coil flow was observed only in the horizontal porous enclosure for low Ra and moderately high aspect ratios, $D = 3$ and $D = 5$. This convective flow was steady in both cases up to a Rayleigh number $Ra \sim 62$, above which occurs a transition to a multicellular regime. The stability of this solution is however affected for higher aspect ratios, since $D = 10$ did not attain a purely longitudinal coil regime.

Regarding the case of the sloping enclosure, there is a general tendency to maximize the heat flux with the transverse rolls regime due to the multiplication of upwellings and downwellings. For low D and Ra however, the Nusselt number associated with the single cell regime, characteristic of high slope angles, can be comparable or higher. On the other hand, the transition between transverse rolls and single-cell convection mode was characterized by a mixed multicellular and longitudinal coil convection accompanied by a decrease in the Nusselt number. An accurate analysis of transition angle to single cell convection as that presented for the 2D case is not achievable in 3D with the available computational facilities, therefore only an overall description can be done at this stage. At $Ra = 50$ the transition angle was clearly dependent on the aspect ratio, in agreement with the 2D study: $\alpha = 17°$, $\alpha = 13°$, and $\alpha =$

9° were the transition angles for $D = 3$, $D = 5$, and $D = 10$, respectively. It can be stated, however, based on the 2D results, that transverse rolls might prevail beyond those angles, this can be tested using suitable initial conditions. On the other hand, for $Ra = 100$, the relation between the transition angle and the aspect ratio is not present, being the transition angle between 9° and 11° for the three aspect ratios analyzed. A more detailed study of the parameter space would be necessary to describe more accurately the transition between the different convective modes observed, for which faster simulations would be convenient. As a final remark, the results show that convective modes in 3D can be of considerable complexity, which impacts not only on the heat transfer properties of the system but also on other aspects not covered in this work such as mass transport properties and entropy generation.

Chapter 4

3D free convection in a layered porous enclosure

4.1 Introduction

Early work on the onset of convection in layered porous media is that by McKibbin & O'Sullivan (1980, 1981). They studied two and three-layer systems considering constant thermal conductivity in a two-dimensional cell. They defined a Rayleigh number referred to the physical properties of the bottom layer and the total thickness and temperature drop of the enclosure. From linear stability analysis they calculated critical values (Ra_c) as a function of the permeability ratio. They found that considerably high permeability ratios between outer and internal layers (~ 20) are required to observe convective modes different from those for a homogeneous porous medium, these convective modes are characterized by some degree of confinement of convection in the high-permeability layers. Richard & Gounot (1981) studied the onset of convection in a layered porous medium considering both anisotropic and isotropic layers as regards the permeability and thermal conductivity. As a particular case study, they calculated numerically Ra_c for the onset of convection for a two-layer porous medium with isotropic layers and showed that the stability of the system increases when the permeability of the upper layer is decreased, their definition of Ra was based on a weighted average of permeability and thermal conductivity on the thickness of the layers. The magnitude of the increase was in turn dependent on the relative thickness of the layers. In a similar two-layer model Rosenberg & Spera (1990) reported an asymptotic increase in the Nusselt number as the permeability ratio of the top to the bottom layers was increased, they observed confinement of convection for a permeability ratio of the top to the bottom layers of 10 and $Ra = 35$, which was defined with respect to the bottom layer of the system. Rees & Riley (1990) investigated three-dimensional stability of convection in a layered porous medium. They found

the conditions under which the preferred flow patterns have a 3D distribution for a two and three-layer porous medium. They also described the relative importance of the different forms of instability in a wide parametric space for those cases. McKibbin & Tyvand (1982) investigated the conditions under which thermal convection in a layered porous medium can be comparable to that for an anisotropic porous medium. They pointed out that a multilayer system can be modelled by an analog anisotropic system when there is no confinement of convection in the layered system.

The problem of porous layers separated by conductive impermeable interfaces has also been investigated. Jang & Tsai (1988) studied the onset of convection in a two-layer system separated by a conductive interface. They defined an overall Rayleigh number considering the total thickness of the arrangement of layers and found that the presence of the impermeable layer increases considerably the stability of the system, the most stable cases being those with the impermeable layer located in the middle. More recently Rees & Genç (2011) studied multilayer systems separated by impermeable interfaces of negligible thickness and observed that the critical Ra, defined locally in each layer, tends asymptotically to 12 as the number of sublayers is increased. Patil & Rees (2014) extended the study to consider finite thickness of the conductive interfaces so that the conductivity had an impact on the behavior of the system. They reported that Ra_c and the associated wave number decreased when the thermal conductivity of the solid interfaces was decreased. Hewitt et al. (2014b) determined statistical steady state convection at high Ra in a 2D periodic porous enclosure. Their model consists of a thin low permeability layer sandwiched by two high permeability layers. Regarding the convective modes they found that for a given Ra and permeability ratio, an increase in the thickness leads to an ordered array of cells with stratification of the flow. On the other hand, they noted that the Nusselt number as a function of thickness of the low permeability layer experiences first a small increase for small thickness and then it decreases for larger thickness.

Although the scope of the analysis presented in this chapter is layered porous media, it is important to mention the work by Nield & Kuznetsov (2007, 2008) who investigated the effect of weak and moderate vertical and horizontal heterogeneities. They defined a Rayleigh number based on the mean properties of the porous enclosure and found that these heterogeneities lead to a reduction in Ra_c for all combinations of horizontal and vertical heterogeneities and all combinations of permeability and conductivity heterogeneities. Regarding this observation they pointed out that there is a higher relative importance of the vertical heterogeneity than the horizontal one. Capone et al. (2012) found that an increase in the permeability in the upward direction is destabilizing whereas an increase in the downward direction is stabilizing Nield & Kuznetsov (2013) reported that horizontal variations in both permeability and thermal diffusivity lead to slight destabilization in comparison with vertical variations.

The main purpose of the study presented here is to obtain 3D steady-state numerical solutions of free convection in a three-layer porous enclosure. As it was done in the previous case studies, the steady-state solutions are obtained from the simulation of the transient problem applying a convergence criterion. A parametric study is carried out to evaluate the Nusselt number as a function of the permeability, thermal conductivity, and thickness of the internal layer of the system.

4.2 Problem formulation

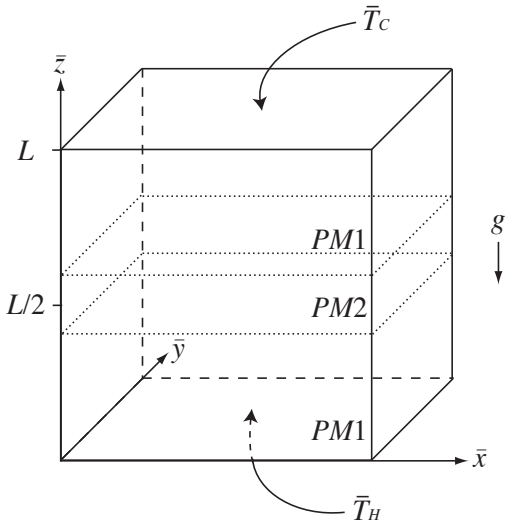

Figure 4.1: Schematic model of a layered porous enclosure heated from below and cooled from the top with adiabatic lateral boundaries. The external layers ($PM1$) have constant properties, whereas the properties of $PM2$ are allowed to vary.

The porous enclosure consists of a three-layer system, of which the external layers have the same and constant physical properties and the internal may differ as regards the permeability and thermal conductivity (Figure 4.1). It is assumed that the porous medium is isotropic within each layer. Fluid flow is governed by Darcy's law and the Boussinesq approximation is invoked. Local thermal equilibrium and negligible viscous heat generation are additional assumptions in this problem. From these considerations the momentum equation can be written in the following form:

$$\bar{\mathbf{u}} = -\frac{k(z)}{\mu}\left(\bar{\nabla}\bar{P} - \rho_0 g\beta(\bar{T} - \bar{T}_0)\hat{\mathbf{k}}\right), \tag{4.1}$$

where the permeability is defined as $k(z) = f(z)k_1$, with k_1 the permeability referred to that for the top and bottom layers, and $f(z)$ is a dimensionless smooth function, which in this case will be defined as a hyperbolic tangent function to represent layers.

The heat transfer equation is as follows

$$\sigma \frac{\partial \bar{T}}{\partial \bar{t}} + \bar{\mathbf{u}} \cdot \bar{\nabla} \bar{T} = \bar{\nabla} \cdot (\eta(z) \bar{\nabla} \bar{T}). \tag{4.2}$$

Likewise, the overall thermal diffusivity is defined as $\eta(z) = g(z)\eta_1$, with η_1 referred to $PM1$ and $g(z)$ a smooth function to represent layers. The condition of incompressibility of the fluid is also invoked:

$$\bar{\nabla} \cdot \bar{\mathbf{u}} = 0. \tag{4.3}$$

Dimensionless variables are defined as follows:

$$x = \frac{\bar{x}}{L}, \quad y = \frac{\bar{y}}{L}, \quad z = \frac{\bar{z}}{L}, \quad P = \frac{k_1}{\mu \eta_1} \bar{P},$$

$$\mathbf{u} = \frac{L}{\eta_1}(\bar{u}, \bar{v}, \bar{w}), \quad \theta = \frac{\bar{T} - \bar{T}_0}{\bar{T}_0 - \bar{T}_c}, \quad t = \frac{\bar{t}\eta_1}{\sigma L^2},$$

$$Ra = \frac{L k_1 g \beta \rho_0}{\eta_1 \mu}(\bar{T}_0 - \bar{T}_c),$$

where Ra is the Darcy-Rayleigh number and L the characteristic length. The dimensionless problem is then as follows. The momentum equation reads:

$$\frac{1}{f(z)}\mathbf{u} + \nabla P = Ra\theta \hat{\mathbf{k}}. \tag{4.4}$$

The dimensionless heat transfer equation reduces to:

$$\frac{\partial \theta}{\partial t} + \mathbf{u} \cdot \nabla \theta = \nabla \cdot (g(z) \nabla \theta). \tag{4.5}$$

That can be written as

$$\frac{\partial \theta}{\partial t} + \mathbf{u} \cdot \nabla \theta = g(z)\nabla^2 \theta + g'(z)\frac{\partial \theta}{\partial z}. \tag{4.6}$$

A global Nusselt number is defined to quantify the heat transfer through the upper surface $z = 1$:

$$Nu = \int \left| \frac{\partial \theta}{\partial z} \right|_{z=1} dA. \tag{4.7}$$

4.2.1 Boundary conditions and initial conditions

As initial condition both dimensionless temperature and velocity are set to zero. The lateral walls of the enclosure are adiabatic and the bottom and top boundaries have specified temperatures, so that the boundary conditions for the heat transfer equation can be written as

$$\frac{\partial \theta}{\partial x} = 0, \quad \text{for} \quad x = 0 \quad \text{and} \quad x = 1,$$
$$\frac{\partial \theta}{\partial y} = 0, \quad \text{for} \quad y = 0 \quad \text{and} \quad y = 1,$$

$$\theta = 1, \quad \text{for} \quad z = 0 \quad \text{and} \quad \theta = 0, \quad \text{for} \quad z = 1 \quad \text{for} \quad t > 0.$$

Regarding the momentum equation, impermeable boundary conditions are assumed. The implementation of these boundary conditions is described in the following section.

4.3 Numerical solution

Considering the results obtained in the previous chapter, the numerical implementation was carried out following the vector potential approach. Pressure is eliminated from the momentum equation (Eq. 4.4) by taking the curl:

$$\nabla \times \left(\frac{1}{f(z)} \mathbf{u} \right) = Ra \nabla \times \theta \hat{\mathbf{k}}. \tag{4.8}$$

This equation is then written in terms of the vector potential $\boldsymbol{\psi}$, such that $\mathbf{u} = \nabla \times \boldsymbol{\psi}$ and $\nabla \cdot \boldsymbol{\psi} = 0$. The components of the momentum equation turn out:

$$\begin{cases} \Gamma \nabla^2 \psi_1 = -Ra \frac{\partial \theta}{\partial y} - \frac{f'(z)}{f^2(z)} v, \\ \Gamma \nabla^2 \psi_2 = Ra \frac{\partial \theta}{\partial x} + \frac{f'(z)}{f^2(z)} u, \\ \Gamma \nabla^2 \psi_3 = 0, \end{cases} \tag{4.9}$$

with $\Gamma = \frac{1}{f(z)}$. The corresponding boundary conditions are:

$$\frac{\partial \psi_1}{\partial x} = \psi_2 = \psi_3 = 0, \quad \text{for} \quad x = 0 \quad \text{and} \quad x = 1,$$
$$\frac{\partial \psi_2}{\partial y} = \psi_1 = \psi_3 = 0, \quad \text{for} \quad y = 0 \quad \text{and} \quad y = 1,$$
$$\frac{\partial \psi_3}{\partial z} = \psi_1 = \psi_2 = 0, \quad \text{for} \quad z = 0 \quad \text{and} \quad z = 1.$$

The system can be further simplified noticing that $\psi_3 = 0$. The problem given by Equations 4.6 and 4.9 with the corresponding boundary conditions was discretized following the Finite Volume numerical method. As mentioned in the previous chapter the solution algorithm is based on the fixed point iteration.

The functions $f(z)$ and $g(z)$ to model layers

The layers are modelled by means of the continuous functions $f(z)$ and $g(z)$. Hyperbolic tangent functions were employed in this model to represent layers in a continuous way. Since the Rayleigh number is referred to the external layers ($PM1$) both $f(z)$ and $g(z)$ must be equal one in these layers. On the other hand, $f(z) = k_2/k_1$ and $g(z) = \eta_2/\eta_1$ in the internal layer ($PM2$). Taking for example the case of $f(z)$, if it is assumed that the medium consists of three layers of equal thickness and permeability ratio k_2/k_1, with $PM1$ at the bottom of the porous enclosure, a hyperbolic tangent function that approaches the condition of layering is

$$f(z) = \frac{1}{2}\left(1 - \frac{k_2}{k_1}\right)(\tanh[c(z - 1/3)] + 1), \tag{4.10}$$

with c a negative constant that measures the rate of change in $f(z)$ at the interface of the layers. This function defines the layering in the range $0 < z < 0.5$, and the symmetric part would define the interface in the interval $0.5 < z < 1$. Likewise, the derivative of $f(z)$ would be

$$f'(z) = \frac{c}{2}\left(1 - \frac{k_2}{k_1}\right)\text{sech}[c(z - 1/3)]^2. \tag{4.11}$$

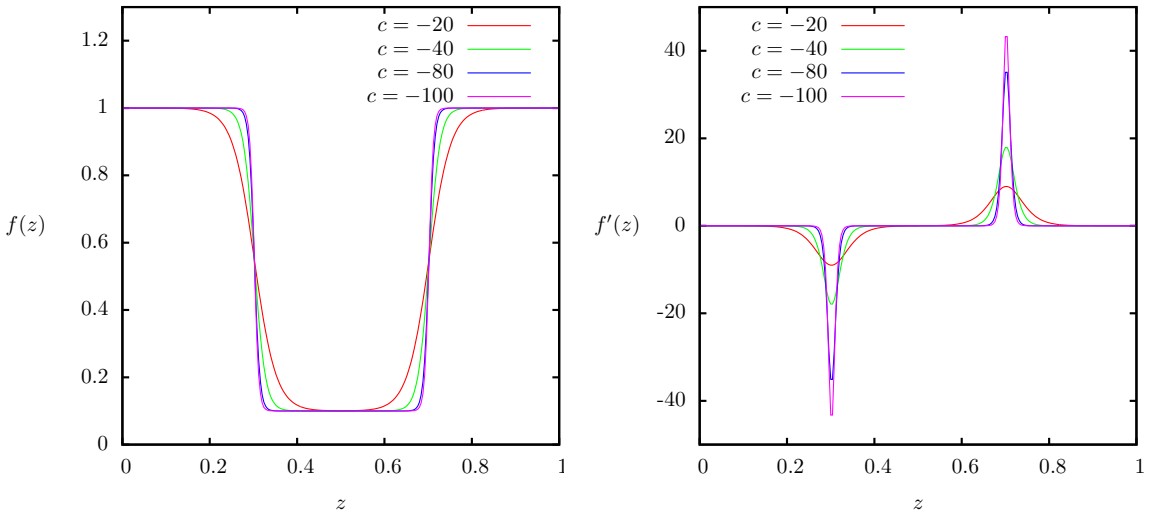

Figure 4.2: Function $f(z)$ and its derivative (Equations 4.10 and 4.11) to model two layers in a porous enclosure with $k_2/k_1 = 0.1$.

Figure 4.2 shows an example of the functions $f(z)$ and $f'(z)$ for $k_2/k_1 = 0.1$. It can be observed that as c increases the function approaches more closely to the discontinuous case that would be given by a step function. The associated cost however, is a very large source term $f'(z)$, which may become numerically difficult to handle. For the simulations presented here a constant $c = -100$ was employed to define both $f(z)$ and $g(z)$.

Discrete problem

The discretization was carried out on the mesh shown in Figure 3.3. The problem is written in the form of the fixed point iteration:

$$L\theta^{m+1} = L\theta^m - \lambda\Upsilon(\theta^m, \psi^m), \tag{4.12}$$

$$\Gamma\nabla^2\psi_1^{m+1} = -Ra\frac{\partial\theta^{m+1}}{\partial y} - \frac{f'(z)}{f^2(z)}v^{m+1}, \tag{4.13}$$

$$\Gamma\nabla^2\psi_2^{m+1} = Ra\frac{\partial\theta^{m+1}}{\partial x} + \frac{f'(z)}{f^2(z)}u^{m+1}. \tag{4.14}$$

In this case however, the heat transfer equation integrated in time (Υ) takes the form:

$$\Upsilon(\theta, \psi) = \frac{1}{\Delta t}\theta - g(z)\nabla^2\theta - g'(z)\frac{\partial\theta}{\partial z} + \mathbf{u}\cdot\nabla\theta - \frac{1}{\Delta t}\theta^0.$$

And the operator L is defined as $L = (\frac{1}{\Delta t} - g(z)\nabla^2)$. Integrating Equation 4.12 on a control volume θ_P (Fig. 3.3) turns out

$$\begin{aligned} &a_P\theta_P^{m+1} - a_E\theta_E^{m+1} - a_W\theta_W^{m+1} - a_N\theta_N^{m+1} - a_S\theta_S^{m+1} - a_F\theta_N^{m+1} - a_B\theta_S^{m+1} = \\ &a_P\theta_P^m - a_E\theta_E^m - a_W\theta_W^m - a_N\theta_N^m - a_S\theta_S^m - a_F\theta_N^m - a_B\theta_B^m \\ &- \lambda(b_P\theta_P^m - b_E\theta_E^m - b_W\theta_W^m - b_N\theta_N^m - b_S\theta_S^m - b_F\theta_F^m - b_B\theta_B^m + s_P). \end{aligned} \tag{4.15}$$

with

$$a_E = \frac{g(P)A_e}{\delta x}, \quad a_W = \frac{g(P)A_w}{\delta x}, \quad a_N = \frac{g(P)A_n}{\delta y},$$

$$a_S = \frac{g(P)A_s}{\delta y}, \quad a_F = \frac{g(f)A_f}{\delta z}, \quad a_B = \frac{g(b)A_b}{\delta z}.$$

Since the function g only varies with z the value of the function on the faces e, w, n, and s is simply the value of the function at the node P.

$$a_P = a_E + a_W + a_N + a_S + a_F + a_B + \frac{\Delta V}{\Delta t},$$

$$b_E = \frac{g(P)A_e}{\delta x} - \frac{u_e^m A_e}{2}, \quad b_W = \frac{g(P)A_w}{\delta x} + \frac{u_w^m A_w}{2},$$

$$b_N = \frac{g(P)A_n}{\delta y} - \frac{v_n^m A_n}{2}, \quad b_S = \frac{g(P)A_s}{\delta y} + \frac{v_s^m A_s}{2},$$

$$b_F = \frac{g(f)A_f}{\delta z} - \frac{w_f^m A_f}{2}, \quad b_B = \frac{g(b)A_b}{\delta z} + \frac{w_b^m A_b}{2},$$

$$b_P = b_E + b_W + b_N + b_S + b_F + b_B + \frac{\Delta V}{\Delta t},$$

$$s_P = -\theta^0 \frac{\Delta V}{\Delta t} - g'(P)(\theta_f - \theta_b)\delta x \delta y.$$

The integration of the vector potential equations (Eqs. 4.13 and 4.13) in their corresponding node ψ_P (Figure 3.3) has the general of

$$a_P \psi_P^{m+1} = a_E \psi_E^{m+1} + a_W \psi_W^{m+1} + a_N \psi_N^{m+1} + a_S \psi_S^{m+1} + a_F \psi_F^{m+1} + a_B \psi_B^{m+1} - s_P, \quad (4.16)$$

with

$$a_E = \frac{\Gamma_e A_e}{\delta x}, \quad a_W = \frac{\Gamma_w A_w}{\delta x}, \quad a_N = \frac{\Gamma_n A_n}{\delta y}, \quad a_S = \frac{\Gamma_s A_s}{\delta y}, \quad a_F = \frac{\Gamma_f A_f}{\delta z}, \quad a_B = \frac{\Gamma_b A_b}{\delta z},$$

$$a_P = a_E + a_W + a_N + a_S + a_B + a_F.$$

The source term for Equation 4.13 is

$$s_{P1} = \int_{CV} \left(-Ra \frac{\partial \theta^{m+1}}{\partial y} - \frac{f'(z)}{f^2(z)} v^{m+1} \right) dV = -Ra(\theta_n^{m+1} - \theta_s^{m+1})\delta x \delta z - \frac{f'(P)}{f^2(P)} v_P^{m+1} \Delta V.$$

Likewise, for Equation 4.14 the source term is given by

$$s_{P2} = \int_{CV} \left(Ra \frac{\partial \theta^{m+1}}{\partial x} + \frac{f'(z)}{f^2(z)} u^{m+1} \right) dV = Ra(\theta_e^{m+1} - \theta_w^{m+1})\delta y \delta z + \frac{f'(P)}{f^2(P)} u_P^{m+1} \Delta V.$$

The discrete problem was implemented in Fortran with parallel computing in OpenMP. The parallelisation was applied to the definition of the matrices given by Equation 4.15 and the two components of the vector potential, each of them given by a discrete equation of the form of Equation 4.16, with the corresponding source term s_{P1} or s_{P2}. The matrices were defined by means of do cycles that move through the $nx \times ny \times nz$ nodes in each iteration of the fixed point algorithm. The matrix for the temperature θ was defined in two steps; for convenience the discrete term $\lambda \Upsilon(\theta^m, \psi^m)$ was defined

first in a do cycle and subsequently, in a second do cycle, all the terms of the discrete heat transfer equation were gathered. On the other hand, the matrices of the components of the vector potential were each of them defined in a do cycle. This means that four do cycles were necessary to define the matrices in each fixed point iteration. The definition of these matrices comprises a large amount of the computational cost of the simulations. Therefore, the parallelisation of those cycles was the priority in the parallel implementation.

Standard OpenMP parallel do directives were applied to the four cycles required to define the matrices. A test model was simulated for purposes of comparison of the computing time between serial and parallel simulations. The model consisted of a homogeneous porous enclosure as that described in Section 3.4.1. In this case however, the Rayleigh number was $Ra = 200$ and the uniform mesh was defined as $\Delta x = \Delta y = \Delta z = 80^{-1}$. At these conditions the computing time required to reach steady state was 13.1 hours for a single thread (serial) simulation, whereas 8.1 hours were required in a two-thread simulation. This implies a decrease of around 38% of computing time.

Once the parallel version of the algorithm was tested, steady-state solutions were obtained from long simulation times using a convergence criterion. The convergence was based on the evaluation of the change in the temperature field during the last 2.2×10^3 successive iterations, which proved to be long enough. Convergence was defined when the average maximum change in the matrix of temperature was less than 5×10^{-7}. A time step $\Delta t = 2 \times 10^{-5}$ and a uniform mesh size $\Delta x = \Delta y = \Delta z = 100^{-1}$ were employed in all the simulations. With these numerical parameters the computing times spanned between 20 and 30 hours for the cases considered in the parametric study.

4.4 Numerical results and discussion

4.4.1 Validation

The validation of our model for the homogeneous case was presented in the previous chapter. A validation for the layered model is presented here using as a reference a three-layer porous enclosure with a thickness of the middle layer $h = 0.2$ and a permeability contrast $k_2/k_1 = 0.01$. For these conditions Rees & Riley (1990) reported a critical Rayleigh number $Ra_c \simeq 270$. McKibbin & O'Sullivan (1980) reported simulation results for these model parameters at $Ra = 300$, they showed a convective mode consisting of four convective rolls confined in the top and bottom layers. A simulation was carried out with our 3D model for the same thickness,

Rayleigh number and permeability ratio. The result was consistent with that reported by McKibbin & O'Sullivan (1980). The steady-state temperature and velocity fields are shown in Figure 4.3 and the streamlines of a 2D section in Figure 4.4.

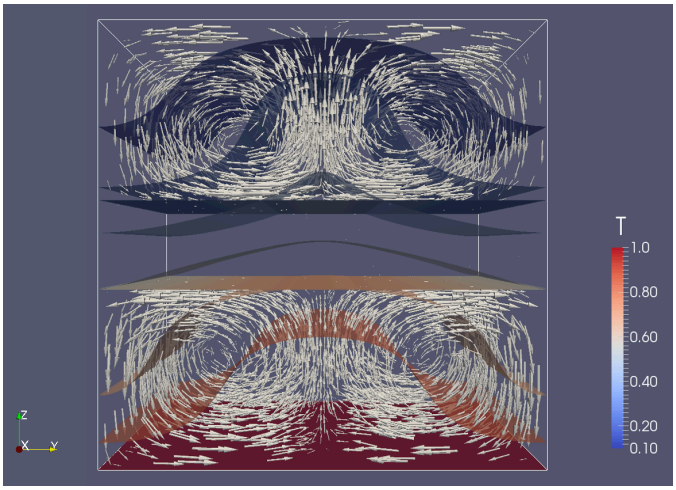

Figure 4.3: Steady-state temperature and velocity fields for $k_2/k_1 = 0.01$, $h = 0.2$, and $Ra = 300$. The corresponding Nusselt number for this result was $Nu = 1.43$.

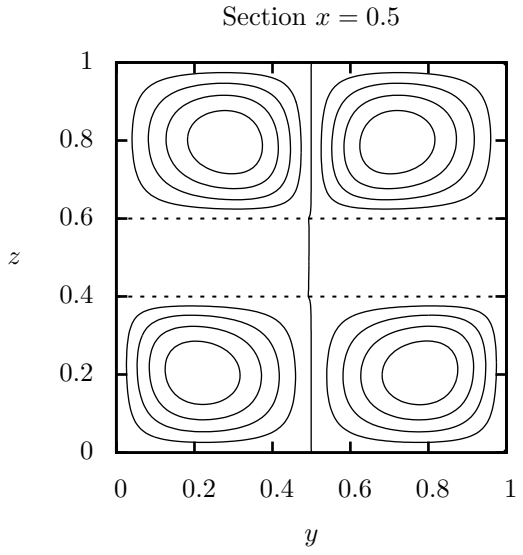

Figure 4.4: Streamlines calculated at the section $x = 0.5$ of Figure 4.3.

4.4.2 Nu vs permeability ratio and internal layer thickness

Let us discuss first the effect of the permeability ratio and internal layer thickness on the Nusselt number. All the simulations were carried out considering a constant $Ra = 200$ and three thicknesses were evaluated, $h = 0.1$, $h = 0.15$ and $h = 0.2$. Jang & Tsai (1988) reported critical Rayleigh numbers between 141 and 213 in this range of thicknesses and considering impermeable internal layer, so that $Ra = 200$ was

considered to be large enough to observe convection in the cases analyzed here. Figure 4.5 shows the steady-state Nusselt number for the three thicknesses analyzed. It can be observed that for relatively low permeability ratio there is a very small change in the Nusselt number, significant differences are observed only around $k_2/k_1 = 0.6$. Furthermore, there is first a slight increase in Nu when the permeability ratio is decreased from 1. Secondly, for high permeability contrast Nu is not necessarily inversely proportional to h as it can be seen at $k_2/k_1 = 0.2$, a similar behavior was reported by Hewitt et al. (2014b) in the context of thin layers and high Ra. In this study however, the reason for this behavior is that the convective modes attained in each thickness is not necessarily the same.

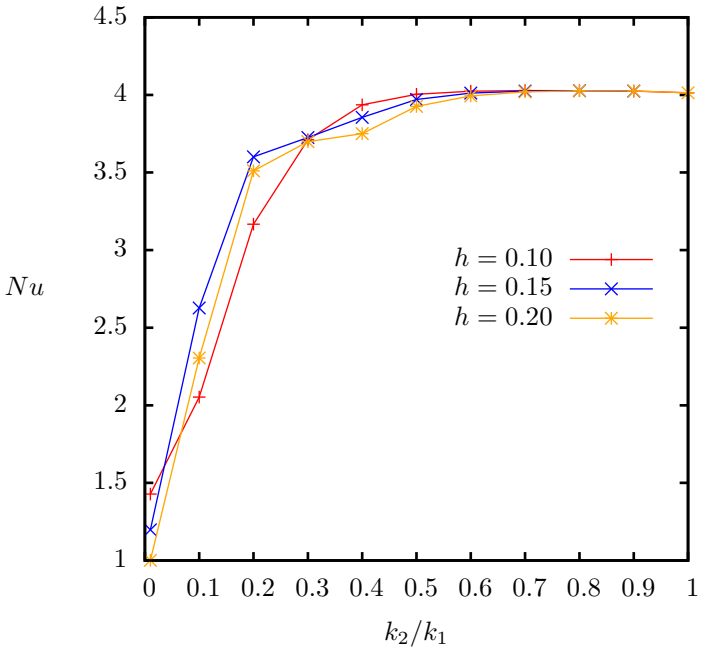

Figure 4.5: Nusselt number vs permeability ratio for three different internal layer thicknesses.

All the convective modes observed in these simulations were characterized by 2D cells. Figure 4.6 shows streamlines calculated at different cross sections perpendicular to the axis of the convective cells. For $k_2/k_1 = 0.01$ it is observed confinement of convection for $h = 0.1$ and $h = 0.15$. When the thickness is increased to $h = 0.2$ however, the system becomes conductive, as shown by the Nusselt number $Nu = 1.0$ (Figure 4.5). $k_2/k_1 = 0.1$ shows that $h = 0.1$ remains essentially as confined convection, whereas $h = 0.15$ and $h = 0.2$ present convection throughout the entire enclosure (Figure 4.7), this convective mode enhances the heat transfer as shown by a larger Nusselt number of these cases in comparison with $h = 0.1$. The same is true for $k_2/k_1 = 0.2$, although in this case there is no confinement, $h = 0.1$ presents a four-cell convective mode that reduces the convective heat transfer in the system in comparison with $h = 0.15$ and

$h = 0.2$, both characterized by two cells partially confined in the top and bottom layers. For the case $k_2/k_1 = 0.3$, the Nusselt number was almost the same (Figure 4.5), despite the convective mode, Figure 4.8 shows the convective modes for $h = 0.1$ and $h = 0.2$. For this permeability ratio, the orientation of the convective cells was not coincident as shown in the case $h = 0.15$, which convective cell was oriented in the y-axis direction. In summary, a strong permeability contrast is required ($k_2/k_1 < 0.5$) to notice a considerable impact on the Nusselt number of the enclosure. Likewise, both thickness and convective mode are important to determine how the Nusselt number is affected.

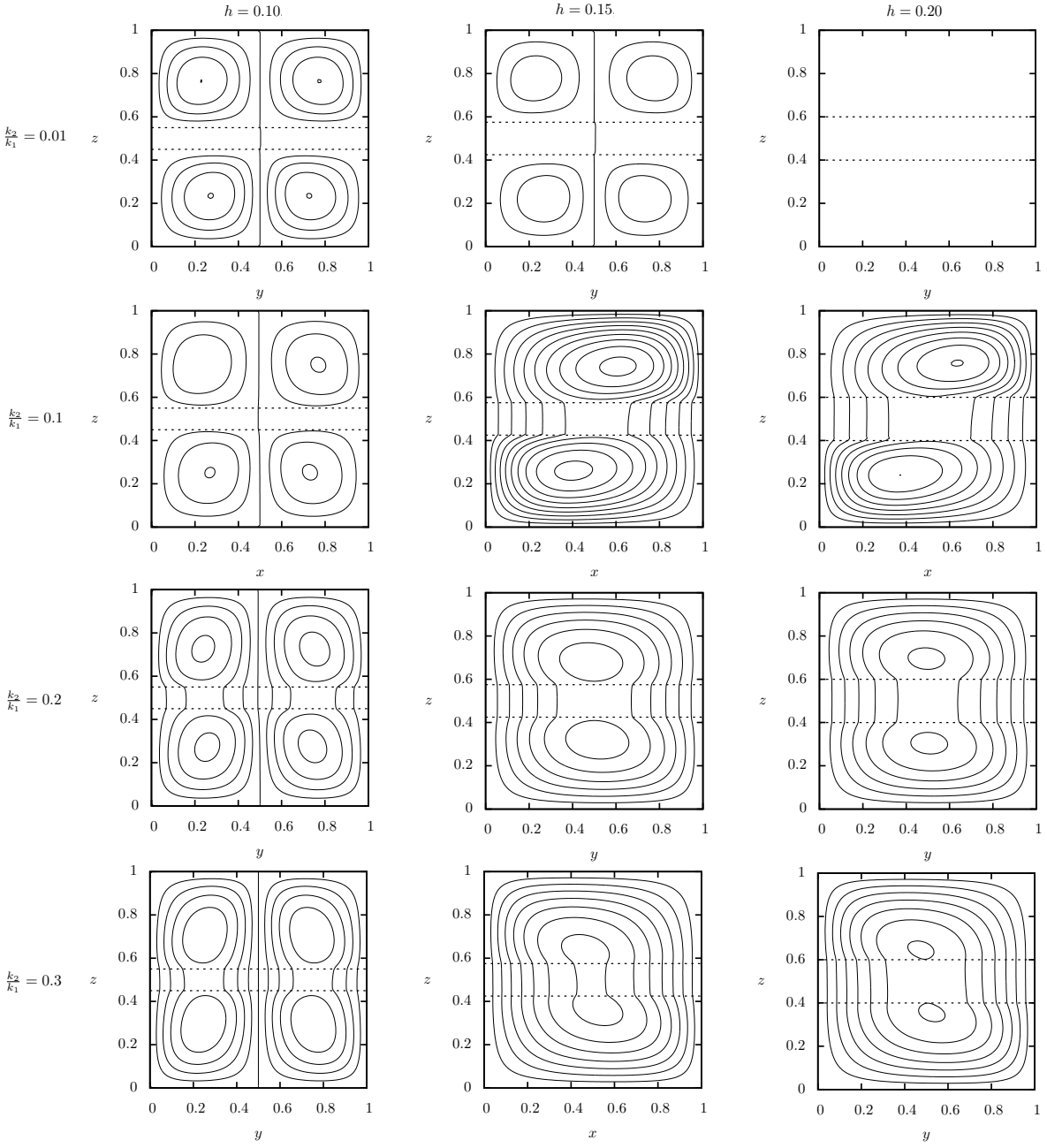

Figure 4.6: Streamlines at the cross section $x = 0.5$ and $y = 0.5$ for high permeability contrast at $Ra = 200$. The corresponding Nusselt numbers are shown in Figure 4.5.

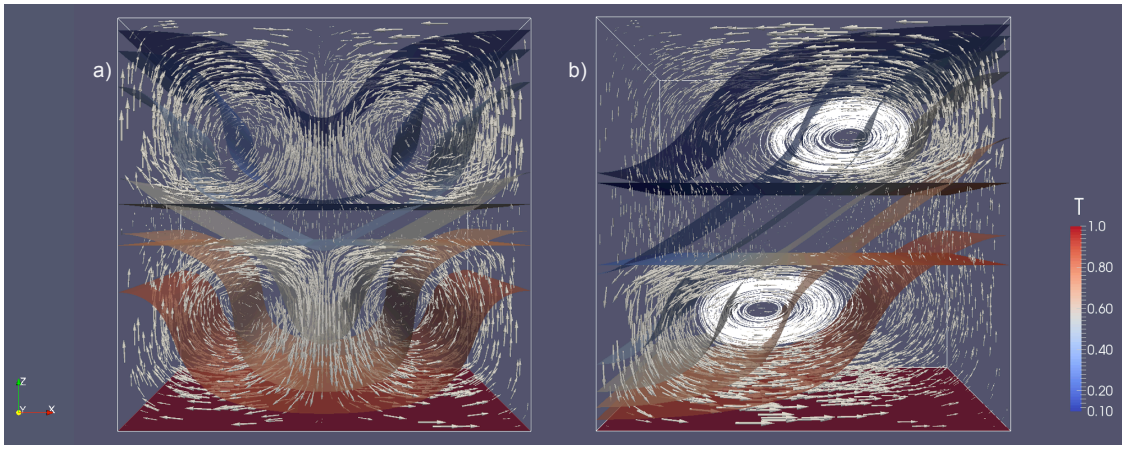

Figure 4.7: Steady-state solutions for $k_2/k_1 = 0.1$ and a) $h = 0.1$ and b) $h = 0.2$.

4.4.3 Nu vs conductivity ratio

The evaluation of the conductivity ratio was carried out considering a constant thickness $h = 0.1$ and $Ra = 200$ for two permeability ratios. No attempt is made here to follow a model for the relation between thermal conductivity and permeability, a presentation of such models can be referred to Bear (1979). Steady state Nusselt numbers of the studied cases are presented in Figure 4.9.

Internal layer with low thermal conductivity ($\eta_2/\eta_1 < 1$)

Let us discuss first the case $\eta_2/\eta_1 < 1$, in which the internal layer acts as a low thermal conductivity layer. In this case, in both permeability ratios, a slight increase in Nu was observed first as the thermal conductivity of the layer was decreased and subsequently Nu decreases. This behavior can be understood as a destabilizing effect of decreasing the thermal conductivity, a further reduction in η_2 leads to a

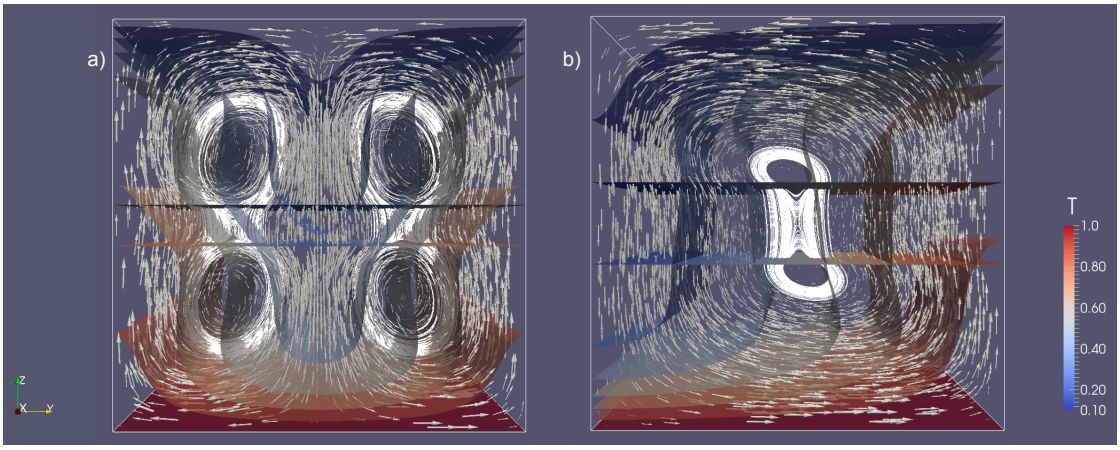

Figure 4.8: Steady state solutions for $k_2/k_1 = 0.3$ and a) $h = 0.1$ and b) $h = 0.2$.

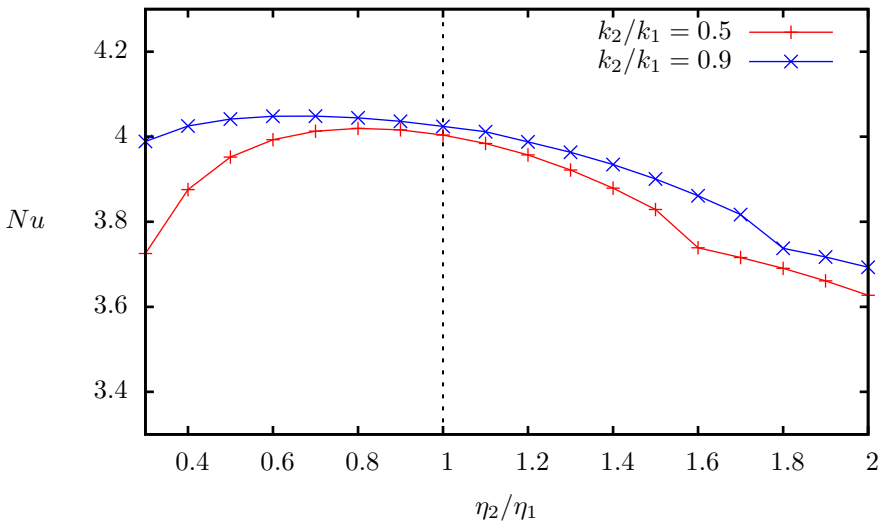

Figure 4.9: Nusselt number vs conductivity ratio for a constant thickness $h = 0.1$ and $Ra = 200$.

drop in Nu as the isolating effect of the layer becomes more important. Regarding the permeability ratio $k_2/k_1 = 0.5$, a high sensitivity to the thermal diffusivity ratio was observed for $\eta_2/\eta_1 < 0.5$, for these values the layer behaves more effectively as a barrier for the heat flux. The convective modes for this permeability ratio were characterized by two main convective cells with secondary internal cells separated by the middle layer. Streamlines are shown in Figure 4.10 and the corresponding temperature and velocity fields in Figure 4.11.

On the contrary, for a weak permeability contrast ($k_2/k_1 = 0.9$) there was in general a low sensitivity to η_2/η_1. Since the system is close to the homogeneous case with

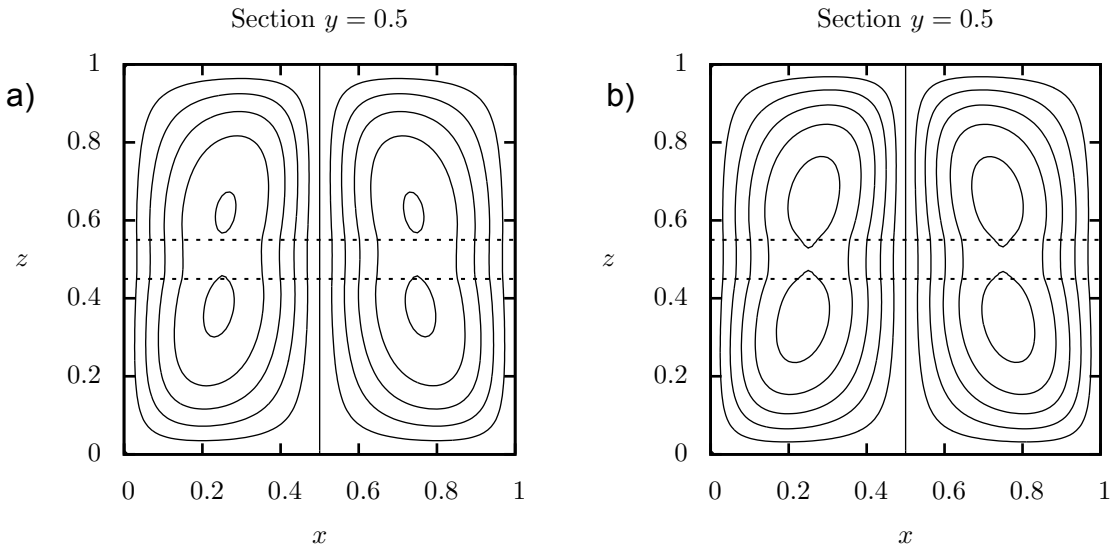

Figure 4.10: Streamlines for $k_2/k_1 = 0.5$ and a) $\eta_2/\eta_1 = 0.2$, b) $\eta_2/\eta_1 = 1.0$.

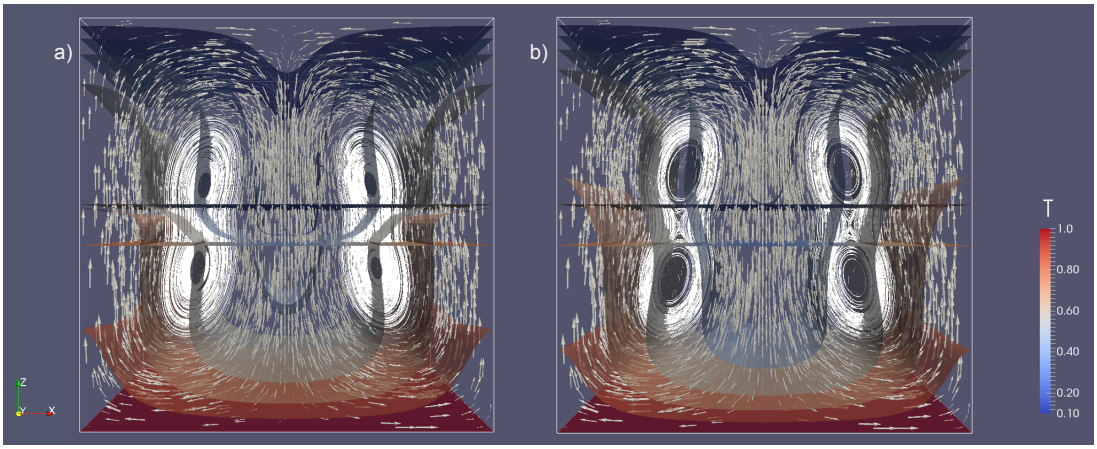

Figure 4.11: Steady-state solutions for $k_2/k_1 = 0.5$ and a) $\eta_2/\eta_1 = 0.2$, b) $\eta_2/\eta_1 = 1.0$.

$Ra = 200$ the convective effects dominate the system and consequently decreasing the thermal conductivity of the layer has little impact. The convective modes of this series were also characterized by 2D velocity distributions consisting of two convective cells. Streamlines of two examples are shown in Figure 4.12 and 3D temperature field in Figure 4.13, respectively.

Internal layer with high thermal conductivity ($\eta_2/\eta_1 > 1$)

On the other hand, the overall effect of increasing the thermal conductivity of the internal layer ($\eta_2/\eta_1 > 1$) was the attenuation of convection in the system. A constant decrease in Nu was observed in both permeability ratios that followed an approximately linear trend (Figure 4.9). Additionally, the correlation between Nu and η_2/η_1 displayed a weak dependence on the permeability ratio for the values analyzed. Two

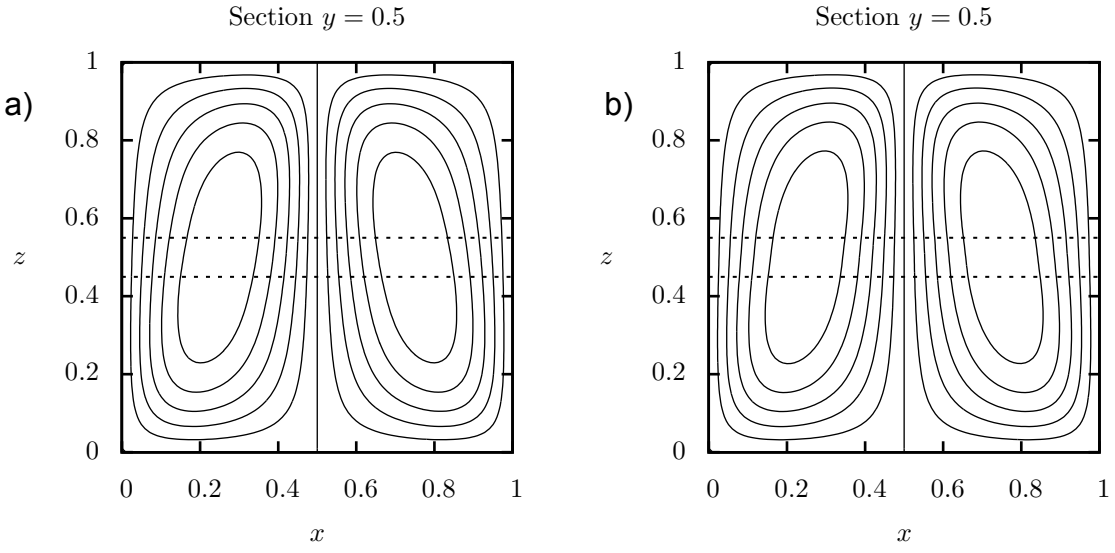

Figure 4.12: Streamlines for $k_2/k_1 = 0.9$ and a) $\eta_2/\eta_1 = 0.3$, b) $\eta_2/\eta_1 = 1.0$.

convective modes were observed in both permeability ratios, for $k_2/k_1 = 0.5$ the multiple cell convective mode shown in Figure 4.10 remains until $\eta_2/\eta_1 = 1.5$. Likewise, for $k_2/k_1 = 0.9$ the two cell regime remains until $\eta_2/\eta_1 = 1.8$, at these thermal diffusivity ratios the convection becomes single cell as shown in Figures 4.14 and 4.15.

4.5 Conclusion

Three-dimensional numerical simulations of free convection were carried out in a porous enclosure consisting of three layers of which the internal one was allowed to vary in permeability, thickness and thermal conductivity. The parametric study to evaluate the effect of decreasing the permeability of the internal layer on the Nusselt number showed that permeability ratios lower than 0.6 are required to observe an appreciable drop in Nu. In agreement with this behavior increasing the thickness of the middle layer had little impact on Nu in the range $0.6 \gtrsim k_2/k_1 < 1$. The steady-state convective modes attained in this parametric study were all characterized by two-dimensional velocity distributions. The three thicknesses analyzed displayed the same convective modes until $k_2/k_1 = 0.4$, in this range of permeability ratios the Nusselt number was, as expected, inversely proportional to h. For permeability ratios between 0.1 and 0.3 the convective modes attained by $h = 0.1$ were different to those for $h = 0.15$ and $h = 0.2$. The thickness $h = 0.1$ developed four convective rolls partially of fully confined in the top and bottom layers, whereas $h = 0.15$ and $h = 0.2$ were characterized by a single cell with two secondary internal cells, this convective mode turned out to enhance the convective heat transfer of the porous enclosure and consequently the Nusselt number was higher in these cases than that for the thinest layer $h = 0.1$. The inverse proportionality relation of Nu with h was recovered at the highest permeability contrast $k_2/k_1 = 0.01$ for which the convection of $h = 0.1$ and $h = 0.15$ was confined convective rolls and $h = 0.2$ led to a conductive solution.

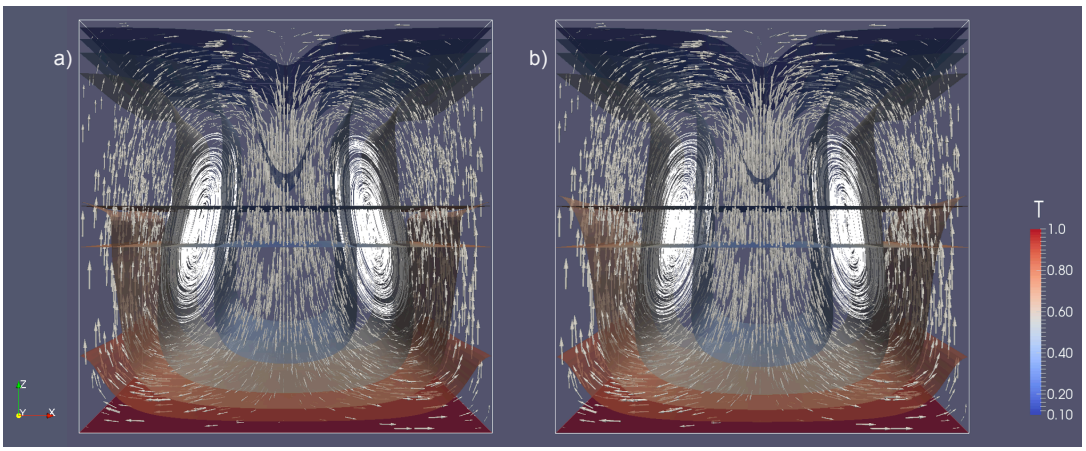

Figure 4.13: Steady-state solutions for $k_2/k_1 = 0.9$ and a) $\eta_2/\eta_1 = 0.3$, b) $\eta_2/\eta_1 = 1.0$.

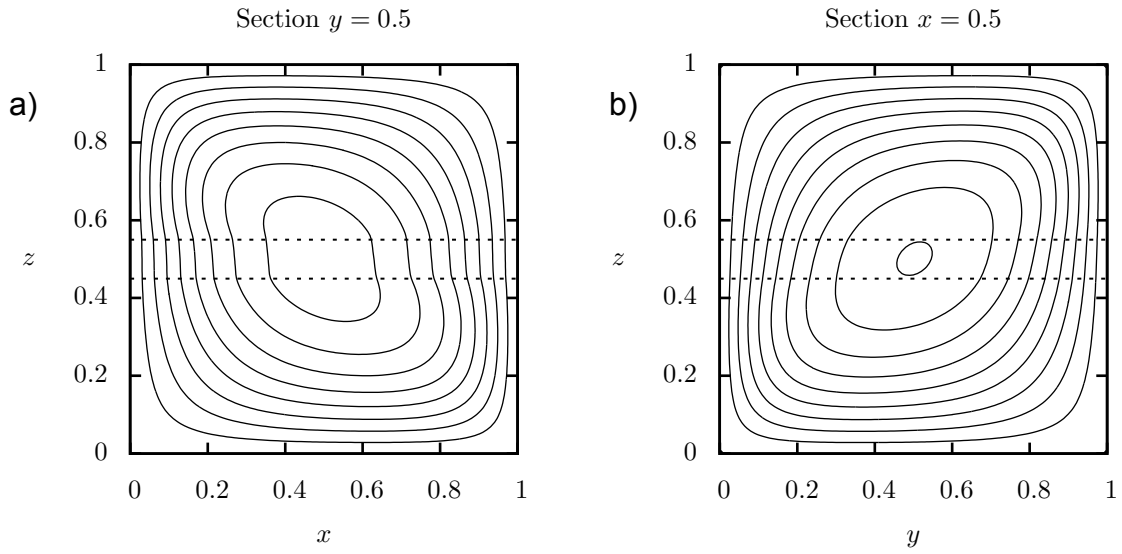

Figure 4.14: Streamlines for a) $k_2/k_1 = 0.5$ and $\eta_2/\eta_1 = 1.6$ and b) $k_2/k_1 = 0.9$ and $\eta_2/\eta_1 = 1.8$.

A slight enhancement of the heat transfer in the enclosure was produced when the thermal diffusivity of the middle layer was decreased up to moderate values. The porous enclosure with a weak permeability contrast $k_2/k_1 = 0.9$ presented a low sensitivity to the decrease, which indicates the dominance of convection in the system. Regarding the permeability ratio $k_2/k_1 = 0.5$, after the slight increase in Nu referred above, the system experienced a monotonic decrease in Nu as the thermal diffusivity of the middle layer was further decreased. At this permeability ratio the layer acted more effectively as a barrier for the heat flux. On the other hand, increasing the thermal diffusivity of the middle layer had a more consistent effect in the two permeability ratios analyzed, which was an approximately linear decrease in

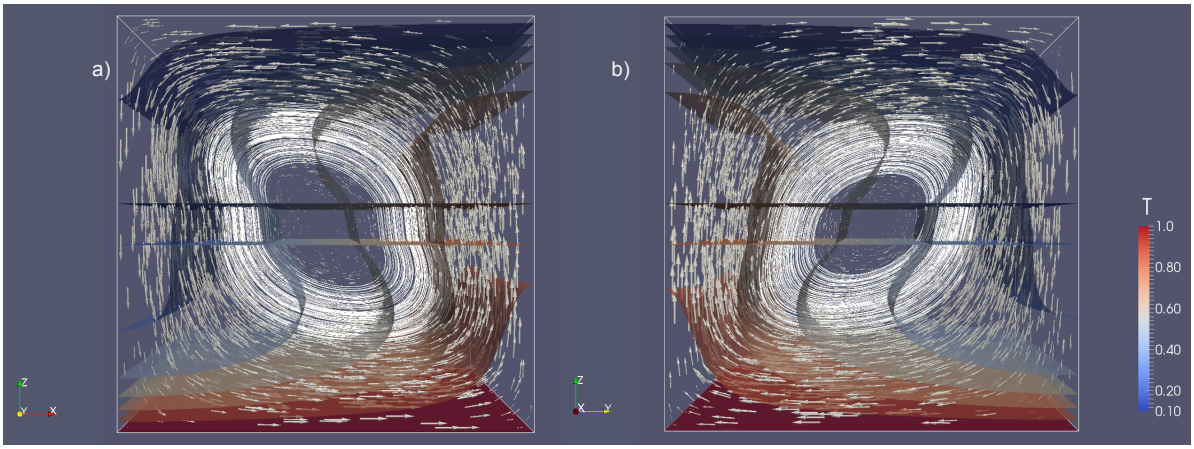

Figure 4.15: Steady-state solutions for a) $k_2/k_1 = 0.5$ and $\eta_2/\eta_1 = 1.6$ and b) $k_2/k_1 = 0.9$ and $\eta_2/\eta_1 = 1.8$.

Nu. Two different convective modes were observed in this case: a dual-cell regime at moderate thermal diffusivity ratios and a single-cell regime at high ratios. However, the transition between these convective modes also appeared to be dependent on the permeability contrast.

The study presented in this chapter permits to qualitatively characterize important features of 3D convection in a layered porous medium. Extension of such an approach to real systems, such as geothermal reservoirs, would require definition of a parameter space reflecting robust models of the relation between thermal conductivity and permeability. No unique model of such relation exists however, as thermal conductivity is largely controlled by mineralogical composition, whereas permeability is principally controlled by independent physical phenomena. Case-specific parameterization would therefore be required in all instances for real natural domains.

Chapter 5

Conclusions

5.1 Achievement of aim and objectives

A comprehensive study of numerical modeling of free convection in porous media was presented in this thesis from which a phenomenological numerical model was developed in three dimensions. Firstly, the problem was solved in two dimensions following two different approaches: primitive variables and stream function, which required different solution algorithms. These numerical schemes were the basis for the solution of the problem in three dimensions. The 2D models were validated considering the case study of a sloping porous enclosure. The models were consistent in terms of the convective modes predicted and the Nusselt number, and were also in agreement with the results available in the literature. The comparison of the computing time associated with the models showed that the stream function is a computationally faster algorithm than the primitive variables approach. A parametric study of the 2D problem of free convection in a sloping porous enclosure showed that two convective modes are possible: multicellular and single cell. When multicellular convection is possible there is in general a wide variety of forms this convective mode can occur. Each of them is characterized by a number of cells (n), and by the way clockwise and anti-clockwise rotation cells are distributed. These configurations displayed different stability as the slope angle was varied. n-odd cases containing more cells rotating as the single-cell configuration for large inclination turned out to be the predominant convective modes. This means that they were the preferred modes to adopt when other configurations were destabilized and also that they prevailed in the largest range α before becoming single cell. Regarding the transition to single-cell convection it was observed that n-odd multicellular configurations can remain as steady state at angles larger than the critical (31.49°), becoming unstable at angles as large as 45°. This angle represents the physical limit for multicellular convection.

Prior to the development of a 3D model, a literature review was carried out and the

vector potential approach was identified as the preferred method to solve the problem in three dimensions. However a comparison between this method and the primitive variables approach was not available in the literature. For this reason, two numerical models based on these approaches were developed. The vector potential approach can be considered as the 3D counterpart of the stream function approach and the solution algorithm was the same as that for the 2D stream function model. The models were compared and validated considering a cubic porous enclosure. The results showed that both models are equivalent in terms of the convective modes and the Nusselt number. The model based on the primitive variables approach however, was found to be less sensitive to the critical Rayleigh number than the vector potential model. Likewise, primitive variables turned out highly sensitive to the mesh size, and finally, as in the 2D analysis, the vector potential model turned out a faster algorithm. Based on these results, the 3D vector potential numerical model was employed to carry out a parametric study of free convection in a sloping porous enclosure in 3D.

A comparison between 2D and 3D results of the parametric study of free convection in a sloping porous enclosure with adiabatic lateral boundaries showed that often the 2D assumptions of the problem are not met even when at low Rayleigh numbers, which seem to justify the assumption. The convective modes present in the 3D analysis comprised longitudinal coil, interaction between longitudinal coil and transverse rolls, and single cell convection. The presence of 3D velocity distributions implies a difference in the transition angles in comparison with the 2D study, as well as the angles associated with the local maxima, particularly at small slope angles. This comparison emphasized the importance of three-dimensional numerical models for the understanding of the phenomenon in real systems in contrast with the 2D idealization.

The third objective of this research was pursued once the best model to simulate free convection in 3D was identified. A porous enclosure comprising three layers was defined, of which the external ones shared the same physical properties and the internal one was allowed to vary permeability and thermal conductivity. The model of layers was defined using continuos hyperbolic trigonometric functions for which high resolution meshes were required. The associated increase in the computational cost was handled implementing parallel computing techniques based on OpenMP libraries available in Fortran 90. The model was validated against 2D results available in the literature and afterwards a parametric study was carried out to analyze the relation between the Nusselt number and the permeability and thermal conductivity contrast keeping the Rayleigh number constant. The main findings of this parametric study are the following: 1) High permeability contrasts (higher than 50%) are required to observe convective modes different from those for a homogeneous porous enclosure, these convective modes are characterized by some degree of confinement of the con-

vection in the high permeability layers. This result is in agreement with previous 2D studies of this problem. 2) For a given permeability ratio, the Nusselt number is proportional to the thickness of the internal layer as long as the convective mode does not change. If an increase in the thickness produces a change in the convective mode the Nusselt number may increase. On the other hand, regarding the relation between the Nusselt number and the thermal conductivity ratio, it was observed that decreasing the thermal conductivity of the internal layer has little impact on the Nusselt number when the porous enclosure is close to the homogeneous case (when the permeability contrast between the layers is low). A permeability ratio $k_2/k_1 = 0.5$ was required to observe an appreciable drop in the Nusselt number as the thermal conductivity was decreased. Interestingly, regardless of the permeability ratio, as the thermal conductivity was decreased it was observed first a slight increase in Nu and then a decrease, which indicates that a slight decrease in the thermal conductivity of the internal layer has a slight positive effect in the convective heat transfer. As regards the increase in the thermal conductivity of the internal layer, the effect is always a decrease in Nu following an approximately linear trend with the conductivity ratio.

5.2 Some contributions of this thesis

The main contributions of the research presented in this thesis are given in the following list:

- Two numerical models to solve free convection in an homogeneous sloping porous enclosure in 2D were proposed and validated. A comparison between these models was not available in the literature.

- A parametric study was presented to analyze the impact on the Nusselt number of the slope angle, aspect ratio, and Rayleigh number, as well as all the possible forms multicellular convection can take and their transition angles. The paramertic space studied here was not available in the literature.

- Likewise, the three dimensional counterparts of the 2D models were proposed. Two 3D models were compared and the choice of the best model was justified in terms of the numerical accuracy and computing time. Although the vector potential approach is often chosen as the most suitable model, a comparison with the primitive variables approach had not been presented before in the literature.

- An equivalent parametric study to that developed for the 2D model was carried out in 3D and visualizations of the convective modes were presented. The

result obtained in this work are also a contribution to this field of research and stresses the importance of 3D phenomenological studies for the understanding of the problem of free convection in real geological systems.

- A numerical model for free convection in a layered porous enclosure was also proposed. A parametric study was carried out to evaluate the impact of the permeability, internal layer thickness, and thermal conductivity ratio on the Nusselt number. This parametric analysis complements previous 2D studies of this problem and also presents high quality visualizations of the convective modes in 3D which are not available in the literature.

- In the parametric study that was carried out for the layered model, it was pointed out that the Nusselt number may increase when the thickness of the internal low-permeability layer of the enclosure is increased. Although this phenomenon has been reported by Hewitt et al. (2014b), their 2D analysis was in the context of thin layers at high Rayleigh numbers, whereas in the case analyzed here the conditions of the problem were different and the explanation was related with a change in the convective mode in the system when the thickness is varied.

5.3 Recommendations for future research

As regards the parametric study that was carried out for the sloping porous enclosure three areas of future work were identified: 1) carrying out a high-resolution parametric study similar to that presented for the 2D case in order to identify transition angles and multiple solutions in 3D. Due to the high computational capacity this would require, solution algorithms faster than Gauss-TDMA in combination with parallel computing would be necessary in the numerical model. 2) Incorporating layers to the sloping porous enclosure would be a new research line since this problem has not been investigated according with the available literature for the development of this thesis. 3) Incorporating mass transport models for the study of combined density-driven flow due to thermal and concentration gradients. An alternative model independent of the Boussinesq assumption would be required however and incorporated to the numerical model. 4) Entropy generation would be another research line of interest to identify whether there is a relation between entropy generation in the system and the steady states obtained in a 3D porous enclosure.

The parametric study of the layered porous enclosure proposed here offers the following research lines for future work: 1) It would be important to incorporate models of the relation between permeability and thermal conductivity to define a parameter space that approaches real geological systems of interest. As it was mentioned in

the conclusions of Chapter 4, there is not a unique model for that relationship, so that it would be necessary to choose case studies of geological formations and layers commonly found in engineering contexts and to investigate if the models for the relation permeability-thermal conductivity exist for those geological systems. 2) The case of free convection in a vertically layered porous enclosure is equally important in the context of geothermal systems since fault zones constitute high permeability structures that very often can be modeled using the continuum assumption (when the number of fractures per unit volume and orientation make possible the determination of a representative elementary volume. See Appendix A.1.). Likewise, low permeability intrusions such as volcanic dikes located in permeable horizons can act as barriers for the flow with different thermal properties. Research in this case study has been less profuse than that for the horizontally layered porous medium (Nield & Bejan 2013) and therefore it is an opportunity for future development of the numerical model presented in this thesis.

Appendix A

Overview of numerical modeling of geothermal systems

A.1 Introduction

The aim of this literature review is to provide a context of application of the processes of fluid flow and heat transfer in porous media, as well as to present the most common assumptions that are made when modeling theses systems. The first part of this review is dedicated to present basic concepts and assumptions for geothermal modeling. The second part is dedicated to describe common approaches to model fluid flow in discontinuous media.

Geothermal energy is a renewable energy resource currently used around the world for electricity production, district heating, and other direct uses of heat. As regards power generation, around 27 countries generate electricity from geothermal resources and the total installed capacity worldwide is 12,729 MW (Bertani 2016). This energy resource is located in the earth crust and consists essentially of a heat source (in most cases of volcanic origin), an overlaying reservoir in which high-temperature geothermal water is stored, and an impermeable cover (seal cap) that reduces thermal contact between the reservoir water and shallower low temperature groundwater.

Modeling geothermal reservoirs involves solving mathematical models based on partial, non-linear and coupled differential equations that make necessary the use of numerical methods and computational simulation techniques to obtain approximate solutions. The increasing power of computational facilities have made possible the development of these techniques in recent decades, giving rise to the important research field of Geothermal Reservoir Simulation. Reviews on this area of research have been presented recently (O'Sullivan et al. 2001, Ingebritsen et al. 2010, Sanyal et al. 2000a). The reviews by O'Sullivan et al. (2001) and Ingebritsen et al. (2010) are focused on conventional hydrothermal systems, whereas Sanyal et al. (2000a) is

focused on enhanced geothermal systems (EGS).

Specific areas of application of geothermal reservoir modeling are the following (Pruess 1990):

- Pressure decline in the depletion of boiling reservoirs
- Evaluation of boiling and condensation zones
- Reservoir exploitation strategies
- Liquid-vapour counterflow systems (vapour-dominated and liquid-dominated heat pipes)
- Transition to vapour-dominated from liquid-dominated conditions
- Natural evolution of hydrothermal convection systems
- Fluid and heat transfer in fractured porous media

Ingebritsen et al. (2010) present the most common assumptions in geothermal reservoir modeling:

Representative elementary volume: An elementary volume exists across which properties such as permeability, thermal conductivity and porosity can be treated as being constant. Some fractured systems do not attain this condition.

Darcian flow: laminar flow assumptions led to multiphase versions of Darcy's law. If turbulence is present, Darcian flow assumption will overestimate the flow rate. There is an upper limit for Darcy's law based on Reynolds number. Its application to flow in porous or fractured media is somewhat problematic, particularly in the context of variable density, multiphase systems. Flow rates sufficient to violate Darcy's law are not common in the subsurface but can occur in geyser conduits, near MOR vents, during phreatic eruptions, and, more generally, in open and well-connected fracture systems.

Local thermal equilibrium: This assumption is generally justified by the generally low rates of subsurface fluid flow and the relative efficiency of heat conduction in geologic media which acts to homogenize the local temperature field. The assumption of thermal equilibrium may not be suitable at the pore scale or in highly fractured media, given sufficiently high, transient flow rates.

Thermal conduction and radiative heat transfer: The thermal conductivity of most common rocks decreases nonlinearly with increasing temperature to at least 250 C. Above 600 C radiative heat transfer becomes significant and can be approximated by a radiative thermal conductivity, which increases with increasing temperature. Both the temperature dependence of thermal conductivity and radiative heat

transfer are usually neglected in hydrothermal modeling. A medium thermal conductivity is typically approximated by a single bulk conductivity of the fluid and rock. Temperature-dependent thermal conductivity is straightforward to implement in numerical solutions and is not computationally expensive considering present computational facilities.

Relative permeabilities: The concept is invoked in multiphase flow problems to express the reduction in mobility of one fluid phase due to the interfering presence of one or other phases. It is treated as a scalar function of volumetric fluid saturation varying from 0 to 1. Relative permeabilities are essentially "fudge factors" that allow Darcy's law to be applied to various empirical data on multiphase flow. Realistic relative permeabilities should vary with porous and fracture geometry, and therefore with scale, and should presumably include hysteresis (between, for example, gas imbibition and gas drainage in water saturated media). However, hysteresis is often ignored in simulations of non-isothermal, multiphase flow, and for modeling purposes, a single global relative permeability is global relative permeability function is commonly invoked. The choice of relative permeability functions can have a large influence on the results of simulations. They are also the largest potential source of nonlinearity in equations greatly complicating numerical solution of any problem invoking extensive multiphase flow.

Capillary pressures: Like relative permeability, capillary pressures are usually computed as functions of saturation using empirical relations and do not account for dynamic effects such as hysteresis. Capillary pressures are often neglected in simulations of hydrothermal flow. This omission is perhaps justified by the limited empirical data on steam-liquid water capillary behavior; the fact that relative permeability functions can incorporate some capillary effects, for instance, through residual liquid saturation; and the fact that surface tension of water decreases with temperature and vanishes at the critical point, where the properties of steam and liquid water merge. However, simulations using plausible functional relations for capillary pressure have shown that capillary forces can increase the efficiency of the heat transfer via countercurrent flow (Udell 1985) and that in rocks with porous matrix and network fractures, typical of hydrothermal systems, capillary pressure tends to keep the vapor phase in the fractures and the liquid in the matrix (Urmeneta et al. 1998).

Boussinesq Approximation: This approximation allows straightforward solution, using a stream function approach, which is particularly useful to resolve boundary layers in convective hydrothermal systems. However it is inappropriate in the general hydrothermal case even if mass based stream function is used because 1) the effects of fluid expansion and pressurization due to in situ heating are neglected, 2) the compressibility of multiphase hydrothermal fluids can be considerably high, 3) the stream function approach can not describe the hydrodynamics of phase separation

and two phase flow. Another deficiency of the Boussinesq approximation is that it assumes that $\frac{\partial \rho}{\partial t} = 0$ and this is not strictly valid for transient flow simulations. Stream function solution of governing equations is no longer necessary but remains quite common.

Nonreactive fluid flow: The rock-water interactions that lead to precipitation and dissolution of minerals are commonly referred to as "reactive transport", that is normally ignored in reservoir models. Laboratory experiments and field observations show that circulating hydrothermal fluids are highly reactive and that hydrothermal reactions have a strong feedback effect on the fluid flow field because they significantly affect rock and fluid properties. However many laboratory experiments involve a strong chemical disequilibrium that may not be representative of natural systems.

Simplified descriptions of permeability: For practical purposes, it is commonly assumed that a REV exists over which fracture permeability can be described by an equivalent porous medium approximation. Transient variations in permeability are commonly ignored. Only a few numerical models have considered variable permeability. (Hurwitz et al. 2002), for example, presented a 2-D numerical model to simulate thermal evolution below Kilauea summit, they considered permeability decrease to represent basalt alteration.

The following section presents a review of the most common approaches to model fluid flow in rocks which is particularly important for the topic addressed in this thesis.

A.2 Fluid flow in rock masses

The presence of fluid flow is a common phenomenon in earth systems, particularly in geothermal systems. Due to its ubiquity and importance in defining other physical phenomena such as heat and mass transport, and mechanical deformation, the best way of modeling fluid flow in rocks has been of interest to many researchers. A detailed study of the subject was presented by Lee & Farmer (1993).

Fluid flow in rock masses is fundamentally different from fluid flow in conventional porous media. A rock mass can be described as a series of blocks of intact rock separated by discontinuities. Fluid flow through a rock mass is determined both by the properties of the intact rock and of the discontinuities, it differs from conventional Darcian flow, which assumes a homogeneous porous continuum with flow through interconnected pore space. In the earth crust, especially in crystalline rocks, the intact rock usually has such low permeability that discontinuities are dominant and fluid flow occurs mainly through discontinuities. In these cases the hydraulic behavior of the rock mass is determined by the geometry of the fracture or discontinuity system.

The study of fluid flow in rock masses consists of several areas, for example: rock and rock mass permeability, geometric characterization of single fractures and fracture networks, fracture statistics and scaling properties, network connectivity and percolation theory. Berkowitz (2002) presented a review and identified several open questions in this area of research, which gives an idea of its current development.

With respect to flow models, there are essentially two schemes: discrete fracture models and continuum models. As pointed out by Berkowitz (2002), these terms can be confusing because in most cases discrete fracture models employ continuum approaches to treat flow within each fracture. The difference consists on whether the model explicitly represents fractures or not, irrespective of the physical assumptions for modeling flow within the fractures.

A.2.1 Continuum models

Continuum models are based on a simplified representation of hydraulic properties of the medium by means of a spacial averaging approach. A discontinuous medium is assumed to have a sufficient number of randomly oriented and interconnected fractures to make it possible to define its average properties statistically and meaningfully.

This assumption implies that a representative elementary volume (REV) exists over which fracture permeability can be described by an equivalent porous media (EPM) approximation. The concept of REV is an extension from the study of homogeneity in porous media. In this context, it is assumed that a macroscopic scale may be found for which a porous medium is seen as a continuum (Figure A.1). On this scale the medium is said to be homogeneous. However, there is no guarantee that such a REV exists for every permeable system (Long et al. 1982).

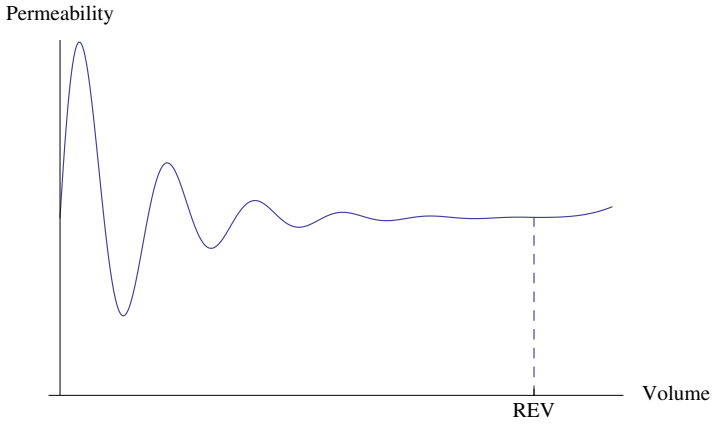

Figure A.1: Statistical definition of a representative elementary volume (REV) for which a porous medium is seen as a continuum (after Long et al. (1982))

In general, a REV approximation can be justified if a formation contains of a dense network of highly interconnected fractures. If a REV can only be defined at a scale

similar to the problem of interest (as is the case for poorly connected networks), or if a network clearly consists of fractures with no characteristic size limit, then the REV approach is inappropriate (Berkowitz 2002). In the presence of heat transfer, it is also necessary that the rock matrix and fractures remain in approximate local thermal equilibrium at all times (Pruess 1990).

Continuum models consists of single continuum (or effective continuum), double continuum (or double porosity) and multiple interacting continua (MINC).

Single continuum

Single continuum models consist of an equivalent porous media formulation. The problem is reduced to Darcian flow and there is no explicit representation of fractures at all. In this method it is assumed that a REV may be found for the fractured rock mass. At this respect, Long et al. (1982) presented a 2-D numerical study of fracture networks based on statistical considerations of geometric parameters of fractures (size, orientation, aperture) as well as the density of the fracture network (number of fractures per unit volume).

Long et al. (1982) pointed out that it only makes sense to look for REV's in fractured rocks in presence of flow systems, which would produce a constant gradient and linear flow lines in a truly homogeneous anisotropic medium. This implies that every part within the test volume receives the same emphasis from the hydraulic gradient. In addition, the following conditions must be met in order to replace a heterogeneous system of given dimensions with an equivalent homogeneous system for the purposes of analysis: 1) There is an insignificant change in the value of the equivalent permeability with a small addition or subtraction to the test volume; 2) An equivalent symmetric permeability exists, which predicts the correct flux when the direction of gradient in a REV is changed.

More recent 2-D studies for the estimation of permeability tensor and REV are attributed to Min et al. (2004) and Chen et al. (2008). These studies were based on the concept of Discrete Fracture Network (DFN). DFN analysis is a widely applied modeling approach, where the fluid flow is dominated by the fractures and the matrix permeability is negligible (Müller et al. 2010). Both studies are based on stochastic generation of DFN's and presented the corresponding algorithms. Min et al. (2004) presented a detailed methodological framework to calculate the REV, however they assumed uniform aperture of fractures that omits the rough nature of fracture planes.

Chen et al. (2008) generated a series of fractured rock samples (DFN's) by means of Monte Carlo method. Geometric parameters of the fractures were defined considering probability models. They analyzed the seepage characteristics of the rock samples changing their sizes and orientations to evaluate the variation of the permeability

components and to determine the existence of the permeability tensor and the representative elementary volume. They presented a detailed algorithm to optimize the stochastic analysis and processing of a large amount of samples.

More recently, Li & Zhang (2010) presented a field study on a compacted, cracked soil ground to determine REV. Although the formation of cracks in soils has a different nature from the formation of fractures in crystalline rocks, the methodology to determine REV and to establish the equivalent continuum approximation is essentially the same. They presented a statistical analysis of geometric parameters of cracks (location, length, aperture, and orientation) and found that the locations and orientations of the cracks followed a uniform distribution, differing from the distribution of fracture sets often observed in fractured rocks. In contrast, they reported that crack length and aperture followed a lognormal distribution, which is consistent with those of rock fractures.

Müller et al. (2010) evaluated the existence of a REV in a fractured geothermal sandstone using DFN model approach. They obtained a quantitative description of their DFN model from field measurements of outcrop reservoir analogues (with exception of fracture aperture that was assumed to be constant). They observed that DFN geometry is largely influenced by lithological layering. Subsequently, 2-D fracture networks were generated and numerical simulations were performed to determine effective hydraulic conductivity tensor and REV. They pointed out that joint spacing in sedimentary rocks tends to be regular, unlike intrusive igneous rocks, and that fracture spacing is roughly proportional to the thickness of the layer.

Some of the first 3-D studies on single continuum are attributed to Long et al. (1985) and Cacas et al. (1990). These authors generated several DFN's by stochastic techniques and further statistical analysis was carried out to evaluate global hydraulic properties (equivalent continuum). Parallel plates representation of fractures was common in early analysis as well as steady flow condition. More details of these methods will be presented in Section A.2.2.

Care must be taken to the presence of coupled processes in order to make a correct application of the equivalent continuum approach. Müller et al. (2010) emphasized that permeability of a fractured reservoir is not only dependent of the geometry of the fracture system but also depends on the stress state of the reservoir. In the same sense, Lee & Farmer (1993) pointed out that flow-related changes in effective stress and fracture surface properties may affect flow patterns, this results in changes in fracture aperture that affect hydraulic behavior. They pointed out that it is also important to evaluate the degree of inter-connectivity of fractures, and superconnection with faults, as well as the presence of chemical changes of dissolution and precipitation. A continuum model involving conventional tensor analysis of an anisotropic rock mass

may not be enough to evaluate flow within a rock mass.

Double porosity and double permeability

In many problems of practical interest the single continuum approach can not be used because the hydraulic equilibrium is not locally established between rock matrix and fractures, so that different average properties for two equivalent continua in the same test volume must be considered.

Dual porosity model has been developed to study these systems in which flow through both rock matrix and discontinuities occur simultaneously, as it is the case of high-porosity rocks. This method has been of particular interest in petroleum reservoir modeling. The proportions of fracture flow and matrix flow can be determined by solution of two sets of flow equations using coupling parameters to represent flow between the matrix and fractures.[1] The head and flux should be balanced in these two flow domains (Berkowitz 2002).

As Berkowitz (2002) pointed out, there is a distinction between double porosity and double permeability models. In the former, it is assumed that the host rock only acts as a storage for fluid that is released to the fractures in presence of pressure drop, while in double permeability models fluid can advance through host rocks so that they form an active part in the flow system.

Double porosity model was first presented by Barenblatt et al. (1960). They studied the problem of seepage (infiltration) considering fissuring as a natural characteristic of the medium. They introduced the conceptualization of two liquid pressures at each point in the space: liquid pressure in the pores and liquid pressure in the fissures, and they take into consideration the transfer of liquid between fissures and pores. The rock mass is conceptualized as the superposition of two porous media, one is observed at a macroscopic scales (fissures) and the other is observed at a microscopic scale (pores). Fluid flow in is governed by Darcy's law in both media.

The pressure related to fissures at each point is the average pressure of the liquid in the fissures in the neighborhood of the given point, while the pressure related to pores is the average pressure in the pores in the neighborhood of the given point. In order to obtain reliable averages, the scale of averaging should include sufficiently large number of blocks.[2] The method of analysis of infinitesimals is then applied to derive the equations of seepage.

[1] These coupling parameters are known in the literature as *exchange coefficients* or *transfer coefficients* and are connected to the so-called shape factor introduced in petroleum engineering (Landereau et al. 2001)

[2] Due to the averaging method of analysis, it is frequent to find the concept of REV in the context of double porosity methods.

Warren & Root (1963) also presented this method. In order to describe reservoir rocks they used the definitions of *primary porosity* as that controlled by deposition and lithification, and *secondary porosity* as that controlled by fracturing, jointing or solution in circulating water. The medium is idealized as discrete volumetric elements with primary porosity that are anisotropically coupled by secondary voids. An important physical assumption in their model is that flow can only occur between primary and secondary porosities; but flow through primary-porosity elements can not occur. They also assumed quasi-steady state in the primary porosity elements at all times. For the mathematical formulation they treat the reservoir as if it were homogeneous so that can define two averaged pressures at each point. Most of the material properties in their mathematical model are determined from statistical information of previous field work and well tests. The secondary porosity and the shape factor that describes the communication between primary and secondary porosity are not known in advance and must be obtained from the analysis of pressure build-up well tests.

Gerke & Genuchten (1993) derived a general expression for the exchange coefficient that accounts for the transfer of fluid between the macropore (or fracture) and soil (or rock matrix). The coefficient is related to the shape and size of matrix blocks and to hydraulic conductivity of the matrix at the matrix-fracture interface. They considered 1-D analysis and assumed that fluid transfer is proportional to the difference in pressure head between the two pore systems. They suggested further work considering more complex geometries to obtain physical insight on realistic problems. Alternatively, their model may be extended to more realistic geometries considering empirical factors which must be calibrated to observed field data.

Quintard & Whitaker (1996) derived governing equations for a double porosity flow system consisting of a slightly compressible fluid in a slightly deformable porous matrix. They used an up-scale approach in their derivation: the description of flow was made first in a pore-scale, subsequently in a Darcy-scale and finally in large-scale. The large-scale analysis was developed using a *two-equation* scheme corresponding to double porosity approach. They subsequently developed the volume-averaged equations for large-scale description of flow and obtained relationships between the local scale description and effective properties. They also identified the domain of validity of their model in terms of a series of time and length scales constraints. The authors emphasized that their results are based on the assumption that Darcy's law is valid to describe flow in both media.

Landereau et al. (2001) presented a 2-D numerical model of a double porosity flow system to study the general behavior of the large-scale coefficients based on the results of Quintard & Whitaker (1996). They studied the relation between the large-scale permeability tensor and fracture connectivity and matrix diffusion, as well as the relation

between exchange coefficient and matrix blocks geometry. For this, they generated a 200×200 m^2 stochastic fracture system using a realistic statistical distribution of fracture parameters, however the numerical implementation was made using average fracture thickness. They reported that there is a double dependence of the large scale hydraulic behaviour, on the geometric parameters of the fracture network, on the one hand, and on the local-scale ratio of fracture conductivity to matrix permeability by the other hand. This double dependence resulted particularly important for the large-scale fracture permeability tensor. Their study also included a comparison of their model with previous ones and they found that for infinite fracture to matrix permeability ratio their results are comparable to other approaches.

More recently, Moutsopoulos & Tsihrintzis (2009) presented a 1-D analytical study of unsteady flow in an infinite double permeability aquifer and compared their model with that obtained from the single continuum approach. Despite the simplifications made by the authors, some basic results were obtained. For sufficiently long times hydraulic equilibrium is obtained, and the piezometric head of both media (fractures and matrix) can be approximated in leading order by the single continuum. They obtained consistent results with Landereau et al. (2001) in the sense that once mechanical equilibrium has been reached, the value of the exchange coefficient has no impact.

Multiple interacting continua

The multiple interacting continua method (MINC) is an extension the early double porosity method of Warren & Root (1963), however it was conceived for numerical applications unlike the more analytical conception of double porosity scheme. This characteristic makes them different in practice. This approach to model flow in fractured media is incorporated to the TOUGH family codes (Pruess (1991)) that has been widely used in geothermal reservoir simulation.

The MINC method was proposed by Pruess & Narasimhan (1985) to take into account the persistent non-equilibrium conditions between matrix blocks and transient effects within the blocks which are conceptualized as nested continua (Figure A.2). These conceptualization is at the same time the computational grid for the numerical implementation, with the outer continuum corresponding to the fractures (area 1, Figure A.2). The latest version of this method includes global flow through matrix blocks.

A limitation of this method arises from the continuum representation of the fracture network. This approximation leads to fracture spacings considerably larger than those typically found. It is also assumed that the equipotential surfaces, as pressure or temperature, have constant distance to the nearest fracture (due to the nested con-

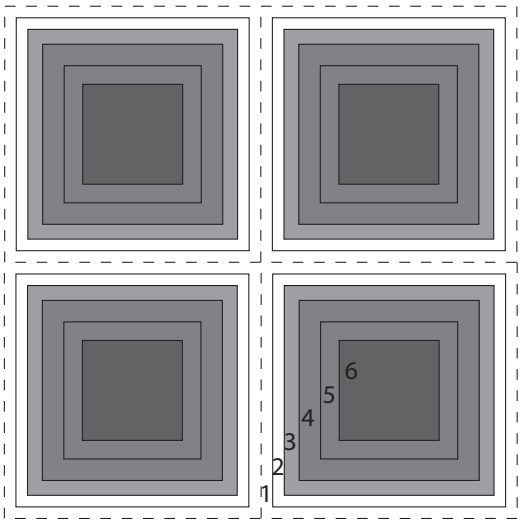

Figure A.2: Nested discretization of the domain to represent matrix blocks and fractures as multiple interacting continua MINC (after Pruess (1990)).

centric cells of the grid blocks), this is not true in reality, however this approximation could be acceptable in some conditions.

A.2.2 Discrete fracture models

Discrete fracture models consist of explicit representation of fractures in the flow domain. The explicit representation of discontinuities permits a more realistic modeling of the flow systems commonly found in engineering. This modeling scheme has been developing into two main research areas: one of them is the study of fundamental processes of flow and transport, some of these studies serve as a feedback to continuum models in addition to provide understanding of transport phenomena in discontinuous rocks. The other area is related to engineering applications in which the geological model of the system of study provides explicit information on the presence of discontinuities and they must be incorporated to transport models.

Shapiro & Andersson (1983) presented one of the first explicit fracture models that aim at predicting the behavior of systems in which the location and nature of fractures is partially known. They proposed to couple the conceptualizations of double porosity and discrete fracture and apply each in the regions where they are most applicable. A problem arises since the scale associated with the discrete fracture and continuum representation are significantly different.

Long & Witherspoon (1985) investigated the effect of the degree of interconnection of fractures on the magnitude and nature of the permeability of the fractured medium. Their study was based on finite element numerical simulations. They generated randomly-oriented fracture networks in 2-D (considering constant apertures

and lengths) and assumed that the matrix rock is impermeable. Flux in the elements is calculated using the cubic law under the assumption that the fractures behave as parallel plates. Steady-state flow through the network was then calculated by solving a series of equations which guarantee that mass balance is maintained. Their work provided feedback to single and double porosity schemes since they analyzed conditions under which a fractured system behaves as an equivalent porous medium. However, it has been shown that the classical view of a rock fracture as a pair of smooth, parallel plates is not an adequate description of flow (Brown 1987, Oron & Berkowitz 1998). It is possible to accurately characterize and incorporate fracture roughness into models.

Andersson & Dverstorp (1987) developed a 3-D numerical model capable of generating a fracture network from stochastic models and solving for the steady state flow. Fractures are modeled as discs of arbitrary size, orientation, transmissivity and location in an impervious matrix. On each fracture disc the flow equations, expressed in terms of hydraulic head, are discretized with the boundary element method. They pointed out that the main problem of using discrete fracture models is to measure and estimate the fracture network statistics from a realistic amount of field data, rather than the complexity of solving the flow through them. They also presented a method for estimating the distribution parameters of the network model from field measurements. Only fracture size, orientation, and density were analyzed since fracture transmissivities were consider to have a log-normal distribution from the previous results by Snow (1970). They used field observations for conditioning the fracture network by requiring that all realizations of the model reproduce the observed traces and only those. The flow problem is expressed in terms of the hydraulic head, for which boundary conditions of specified head or no flow were given. They obtained qualitatively consistent results with previous 2-D works (such as Long & Witherspoon (1985)). They pointed out that one of the most important assumptions of their model is to consider constant transmissivity in the fracture planes, further work was suggested to consider variable transmissivity and channeling phenomenon.

Channel-based interpretation of flow in fractured media

The conceptualization of fractures as parallel plates has been considered unsuitable to capture the complex flow regime in fractures. Tsang & Neretnieks (1998) described several laboratory experiments and field tests at different scales that confirm the strongly heterogeneous flow paths in fractured media for which channeling conceptualization results more suitable.

Brown (1987) presented one of the earliest numerical models for the analysis of flow in a rough-wall fracture. He studied the magnitude and nature of the disagree-

ment between the predictions of the parallel plate model and the actual flow through rough-walled fractures from a series of two-dimensional simulations. His flow model was based on the Reynolds equation and fractal model for the surface topography. The Reynolds equation is commonly used in lubrication problems and is suitable in conditions of low speed flows when inertial effects can be neglected (see for example Karniadakis et al. (2005)). The disagreement between the cubic law and flow through rough-wall fracture was measured by comparing the flow rates obtained by the two approaches. He showed that largest disagreements, up to a factor of two, are obtained for the smallest apertures that were tested.

Tsang & Tsang (1987) proposed to consider channels, rather than single fractures, as the basic unit for modeling a fractured medium. They hypothesized that fluid flow and solute transport through a tight rock medium is by means of a limited number of tortuous and intersecting channels (Figure A.3). The parameters that characterize the channels are 1) the aperture density distribution, which gives the relative probability of occurrence of a given aperture value, 2) the effective channel length and 3) the spatial correlation length of the aperture, which gives the spatial range within which the aperture values are similar.

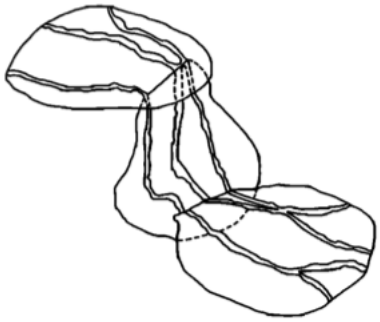

Figure A.3: Conceptual model of flow channel in a fractured medium (after Tsang & Tsang (1987)).

They proposed a model to analyze the expected steady-state pressure distribution in a fractured medium under constant pressure boundary conditions and the tracer concentration as a function of time in tracer transport measurements. Despite of simplifications, such as considering constant channel width or neglecting the matrix diffusion on the tracer transport, their work presented the conceptual basis to have a more realistic flow regime in fractured media.

Further development of this model was presented by Tsang et al. (1991). They presented a variable aperture channel model to evaluate tracer transport field data from the Stripa mine, Sweden, that lies in granitic rock. The experiment consisted of a system of tracer injection boreholes drilled above two mine drifts in the form of a cross, the longer drift was 75m long and the shorter was 25m long. Tracer collectors

were placed uniformly over the ceiling of the drift to measure tracer flow rates and to analyze flow paths.

The Stripa 3D data were analyzed based on the hypothesis that the dispersion is advection dominated. In their conceptual model they emphasized that the channels are not physical pipes in the fracture plane, but they arise directly from the wide range of apertures distributed over each fracture. They considered that the injected tracer may be transported through the medium along several tortuous channels in a three-dimensional space as a result of the fracture network heterogeneity. Each of these flow channels consists of a number of flow paths of comparable but not identical mean velocities, thus giving rise to some kind of dispersion within each flow channel. Each flow path that makes up the channel has variable aperture along its length. They assumed that matrix diffusion and chemical retardation processes are not important. From the time dependence of the tracer collection, they identified channels or groups of flow paths which have comparable residence times. They assumed homogeneous one-dimensional porous medium to model flow in channels. Their analysis of the experimental data confirmed the existence of preferential flow paths.

Cacas et al. (1990) also considered channeling. The purpose of their study was to develop a method to estimate the permeability of a hypothetical REV in rocks characterized in the context of nuclear waste repository applications. They generated DFN's whose geometry is statistically similar to the observed in the field. Hydraulic simulations were carried out in an intermediate scale: larger than the mean fracture size but smaller than the hypothetical REV, and each simulation on a different fracture configuration provided a "punctual" value of the global permeability of the fractured network. Flow is governed by the hydraulic gradient and hydraulic conductivity of the fractures.

From statistical analysis of a series of DFN models they calculated global permeability based on a result from Gutjahr et al. (1978), that relates the global permeability with the geometric mean of the punctual permeabilities. Validation was carried out from estimations of "global" hydraulic permeability and taking into account diverse field measurements such as piezometric head monitoring, injection tests, and tracer tests. From their results, they estimated that a 10 m-edge cubic block seems to be reasonably representative of the punctual scale of the equivalent continuum.

To simulate channelling, they assumed that flow occurs through bonds joining the center of each disc to the center of adjacent discs (Figure A.4), provided that the fractures are connected, so that the circular shape of the fractures is not of great consequence in their modeling technique. Since the representation of channels was not realistic, calibration of bonds conductivity from injection test data was necessary.

A recent report by Black & Barker (2007) summarizes the most important experimen-

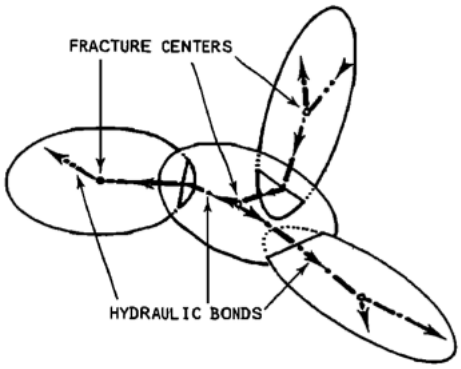

Figure A.4: Conceptual model of flow channeling through bonds joining the center of connected fractures (After Cacas et al. (1990)).

tal observations and theoretical results regarding the channel-based interpretation:

- Groundwater flows within sparse network of channels just above the percolation limit.
- The frequency of intersections is low in that individual channels extend considerable distances between significant junctions.
- Individual channels often extend over many fracture surfaces and the resulting flow system is only weakly related to the density or size of mappable fractures.
- The sparseness of the systems compared to the size of drifts and tunnels means that very few "flow channels" are intersected by drifts and tunnels. Highly convergent flow is required to connect to the rest of the network and this is misinterpreted by a skin of low hydraulic conductivity.
- Systems are so sparse that they are controlled by a few "chokes" that give rise to compartments of head, and probably, of groundwater chemistry.
- The actively flowing sparse channel network, occurring within any particular rock, is a naturally selected, small subset of the available channels. Hence, there are many conductive channels that do not participate within the active network but are connected to it, however tortuously.

According to Lee & Farmer (1993) from early studies on discrete fracture models was concluded that, whether a rock mass behaves like a continuum or a discrete fracture model, the discontinuity size and frequency are important factors. Thus, the estimation of flow behaviour in rock masses requires a detailed description of discontinuity geometry.

More recently de Dreuzy et al. (2012) presented a 3D numerical study of DFN's embedded in impervious matrices to analyze the combined effect of fracture-scale

heterogeneities and network-scale topology on the equivalent permeability of the fractured medium. Their analysis was based on 2×10^6 DFN simulations that accounted for an extensive sampling of parameter space. They investigated different types of network structures, including networks with a power law size distributions of the fracture sizes. They also varied density from configurations far above the percolation threshold to the vicinity of the percolation threshold. Fractures were modeled as parallel plates, however they used a Gaussian law distribution to define fracture local apertures. Channeling effects were considered.

For the flow model they considered creeping flow (no inertial effects) and a gradient of the aperture field topography much smaller than 1, from which they assumed that pressure field only depends on the two dimensional position along the mean fracture plane and that the local flux field is related at each point of the mean fracture plane to the local pressure gradient according to a local cubic law. They pointed out that this model is valid for Reynolds numbers lower than 1 in all fractures of the network.

As a general result, they pointed out that fracture heterogeneities led to a reduction of the equivalent fracture transmissivity up to a factor of 6 as compared to the parallel plate of identical mean aperture. Permeability is enhanced by the highly transmissive zones within the fractures that can bridge fracture intersections within a fracture plane, and it is reduced by the closed and low transmissive areas that break up connectivity and flow paths. Further studies were proposed to understand how anisotropic mechanical load impacts on the permeability.

Graf & Therrien (2008) presented a three-dimensional model of a variable-density flow and solute transport in discretely fractured porous media. Unlike previous discrete fracture models, in which fractures are modeled as parallel plates in space, they modeled flow in a non-planar fracture, permitting the definition of more complex geometry of the fracture. They used the computational program HydroGeoSphere, a numerical 3D variable-density, variably-saturated groundwater flow and multi-component solute transport model for fractured porous media based on a control volume finite element method (CVFE). The program had to be modified to include triangular fracture elements. The flow model in the fracture is Darcian and they did not considered variable aperture so that channeling effects were disregarded. Their work presented fundamental processes of solute transport and density-gradient driven flow in fractures, such as fingering of solute concentration and coalescence. Further improvements to represent non-planar fractures embedded in porous media were presented by Mustapha et al. (2010), they proposed optimized algorithms to generate non-structured finite element meshes using Delaunay criterium (Shewchuk 2002).

Inertial effects in flow in fractured media (non-Darcian flow)

Kolditz (2001) studied fluid flow in fractured rock in which convective acceleration is important, giving rise to non-linear flow, i.e., a flow regime deviated from the conventional linear relationship between pressure gradient and seepage velocity described by Darcy's law. He pointed out that fracture roughness as well as fracture intersections in networks may be causes of non-linear (non-Darcian) flow phenomena in fractured media. Phenomena as no parallel motion (i.e. velocity components normal to the fracture plane arise from asperities) and channeling effects in fracture planes are commonly associated to non-linear flow. His work is focused on modeling effects of high flow rates and fracture roughness.

The author presented first the most important theoretical considerations to describe non-linear flow and to derive governing equations, from which the pressure-gradient dependence of the hydraulic permeability was highlighted. Subsequently, finite-element numerical simulations were carried out using the program Rockflow in a plane single fracture and in a fracture network generated from field data. The fracture network was composed by seven fractures corresponding to those identified in the crystalline-rock reservoir of the Soultz site, France.

He pointed out that in ordinary porous media the order of critical Reynolds numbers for which non-linear effects become evident, determined in experiments, is about 1-10 (Barenblatt et al. 1990). The corresponding velocities are only in the range of millimeters or centimeters per second. There is a transition between the flow regimes because of the range of pore radii. For flow in fractures, however, critical Reynolds numbers are in the same order of those for tube flows (about two orders of magnitude larger than those for flow in a porous medium).

For the case of a smooth single fracture, critical Reynolds numbers for onset of non-linear flow behaviour were found in agreement with those known from experiments. But on the other hand, fracture roughness as well as non-linear flow phenomena lead to reduction of effective permeabilities. For the fracture network, pumping test data of the field were well reproduced by applying the non-linear flow model. Further work was suggested on critical Reynolds numbers for natural (rough) fractures and for more complex flow conditions, as well as storativity of fracture systems.

Appendix B

Finite volume integration of a Poisson equation

In this appendix we present the general form of discrete Poisson equation in the Finite volume numerical method. Lets assume that a variable ϕ is described by a Poisson equation with a source term q as follows

$$\Gamma \nabla^2 \phi = q \tag{B.1}$$

The integration of this equation in a 3D control volume with central node P (Figure B.1) is as then

$$\int_{CV} \Gamma \nabla^2 \phi dV = \int_{CV} q dV$$

$$\int_b^f \int_s^n \int_w^e \left(\Gamma \frac{\partial^2 \phi}{\partial x^2} + \Gamma \frac{\partial^2 \phi}{\partial y^2} + \Gamma \frac{\partial^2 \phi}{\partial z^2} \right) dx dy dz = q_P \delta V$$

Integrating term by term and doing the control volume approximation it turns out

$$\left[\left(\Gamma \frac{\partial \phi}{\partial x} \right)_e - \left(\Gamma \frac{\partial \phi}{\partial x} \right)_w \right] \delta y \delta z + \left[\left(\Gamma \frac{\partial \phi}{\partial y} \right)_n - \left(\Gamma \frac{\partial \phi}{\partial y} \right)_s \right] \delta x \delta z + \left[\left(\Gamma \frac{\partial \phi}{\partial z} \right)_f - \left(\Gamma \frac{\partial \phi}{\partial z} \right)_b \right] \delta x \delta y = q_P \delta V$$

Applying central differencing to approximate the derivatives and renaming the areas

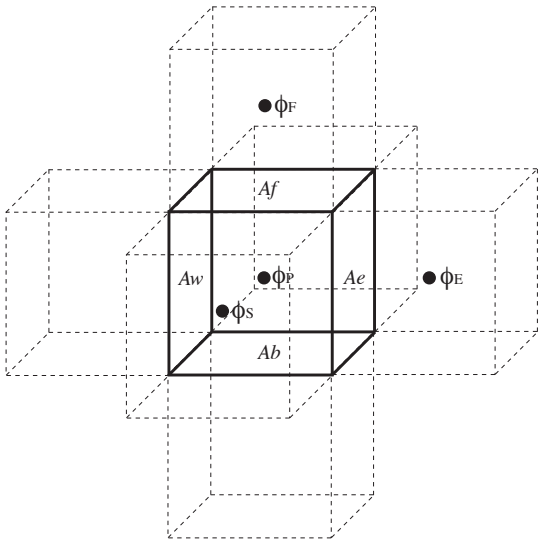

Figure B.1: Three-diemensional control volume for the integration of Equation B.1.

of the faces $\delta y \delta z$, $\delta x \delta z$, and $\delta x \delta y$

$$\left[\Gamma_e A_e \frac{\phi_E - \phi_P}{\delta x} - \Gamma_w A_w \frac{\phi_P - \phi_W}{\delta x}\right] + \left[\Gamma_n A_n \frac{\phi_N - \phi_P}{\delta y} - \Gamma_s A_s \frac{\phi_P - \phi_S}{\delta y}\right] + \left[\Gamma_f A_f \frac{\phi_F - \phi_P}{\delta z} - \Gamma_b A_b \frac{\phi_P - \phi_B}{\delta z}\right] = q_P \delta V \tag{B.2}$$

This can be written as

$$a_P \phi_P = a_E \phi_E + a_W \phi_W + a_N \phi_N + a_S \phi_S + a_F \phi_F + a_B \phi_B - s_P \tag{B.3}$$

with

$$a_E = \frac{\Gamma_e A_e}{\delta x}, \quad a_W = \frac{\Gamma_w A_w}{\delta x}, \quad a_N = \frac{\Gamma_n A_n}{\delta y}, \quad a_S = \frac{\Gamma_s A_s}{\delta y}, \quad a_F = \frac{\Gamma_f A_f}{\delta z}, \quad a_B = \frac{\Gamma_b A_b}{\delta z}$$

$$\Gamma_e = \frac{\Gamma_P + \Gamma_E}{2}, \quad \Gamma_w = \frac{\Gamma_W + \Gamma_P}{2}, \quad \Gamma_n = \frac{\Gamma_N + \Gamma_P}{2}$$

$$\Gamma_s = \frac{\Gamma_S + \Gamma_P}{2}, \quad \Gamma_f = \frac{\Gamma_F + \Gamma_P}{2}, \quad \Gamma_b = \frac{\Gamma_B + \Gamma_P}{2}$$

$$a_P = a_E + a_W + a_N + a_S + a_B + a_F$$

and

$$s_P = q_P \delta V$$

Dirichlet boundary conditions

Let us take the x-axis as a example on the integration of the equation at the boundaries. As regards the lower boundary, the Dirichlet condition establishes a constant value for ϕ_W, that we can call ϕ_{WB}, a node that would be lying at the boundary. Additionally, since the distance between P and the boundary is $\delta x/2$ the discrete form of Equation B.1 takes the form

$$\left[\Gamma_e A_e \frac{\phi_E - \phi_P}{\delta x} - 2\Gamma_w A_w \frac{\phi_P - \phi_{WB}}{\delta x}\right] + \left[\Gamma_n A_n \frac{\phi_N - \phi_P}{\delta y} - \Gamma_s A_s \frac{\phi_P - \phi_S}{\delta y}\right] + \left[\Gamma_f A_f \frac{\phi_F - \phi_P}{\delta z} - \Gamma_b A_b \frac{\phi_P - \phi_B}{\delta z}\right] = q_P \delta V$$

Simplifying this expression it can be seen that the coefficients and source term of Equation B.3 are

$$a_E = \frac{\Gamma_e A_e}{\delta x}, \quad a_W = \frac{2\Gamma_w A_w}{\delta x}, \quad a_N = \frac{\Gamma_n A_n}{\delta y}, \quad a_S = \frac{\Gamma_s A_s}{\delta y}, \quad a_F = \frac{\Gamma_f A_f}{\delta z}, \quad a_B = \frac{\Gamma_b A_b}{\delta z}$$

$$a_P = a_E + a_W + a_N + a_S + a_B + a_F$$

and

$$s_P = q_P \delta V - \frac{2\Gamma_w A_w}{\delta x}\phi_{WB}$$

Similarly for the upper boundary, given ϕ_{EB} the coefficients are

$$a_E = \frac{2\Gamma_e A_e}{\delta x}, \quad a_W = \frac{\Gamma_w A_w}{\delta x}, \quad a_N = \frac{\Gamma_n A_n}{\delta y}, \quad a_S = \frac{\Gamma_s A_s}{\delta y}, \quad a_F = \frac{\Gamma_f A_f}{\delta z}, \quad a_B = \frac{\Gamma_b A_b}{\delta z}$$

$$a_P = a_E + a_W + a_N + a_S + a_B + a_F$$

and

$$s_P = q_P \delta V - \frac{2\Gamma_e A_e}{\delta x}\phi_{EB}$$

Neuman boundary conditions

On the other hand, taking again the x-axis as an example, if the gradient is given at the boundaries we have that $\frac{\phi_P - \phi_W}{\delta x} = \phi'_{WB}$ and $\frac{\phi_E - \phi_P}{\delta x} = \phi'_{EB}$, are known values. For the lower boundary, Equation B.2 takes the form

$$\left[\Gamma_e A_e \frac{\phi_E - \phi_P}{\delta x} - \Gamma_w A_w \phi'_{WB}\right] + \left[\Gamma_n A_n \frac{\phi_N - \phi_P}{\delta y} - \Gamma_s A_s \frac{\phi_P - \phi_S}{\delta y}\right] + \left[\Gamma_f A_f \frac{\phi_F - \phi_P}{\delta z} - \Gamma_b A_b \frac{\phi_P - \phi_B}{\delta z}\right] = q_P \delta V$$

Considering this, it can be seen that the coefficients of Equation B.3 are

$$a_E = \frac{\Gamma_e A_e}{\delta x}, \quad a_W = 0, \quad a_N = \frac{\Gamma_n A_n}{\delta y}, \quad a_S = \frac{\Gamma_s A_s}{\delta y}, \quad a_F = \frac{\Gamma_f A_f}{\delta z}, \quad a_B = \frac{\Gamma_b A_b}{\delta z}$$

$$a_P = a_E + a_N + a_S + a_B + a_F$$

and

$$s_P = q_P \delta V + \Gamma_w A_w \phi'_{WB}$$

Similarly for the upper boundary, given ϕ'_{EB} the coefficients are

$$a_E = 0, \quad a_W = \frac{\Gamma_w A_w}{\delta x}, \quad a_N = \frac{\Gamma_n A_n}{\delta y}, \quad a_S = \frac{\Gamma_s A_s}{\delta y}, \quad a_F = \frac{\Gamma_f A_f}{\delta z}, \quad a_B = \frac{\Gamma_b A_b}{\delta z}$$

$$a_P = a_W + a_N + a_S + a_B + a_F$$

and

$$s_P = q_P \delta V - \Gamma_e A_e \phi'_{WE}$$

Further details on the integration of the differential equation in Finite Volume can be referred to Versteeg & Malalasekera (1995).

Bibliography

Andersson, J. & Dverstorp, B. (1987), 'Conditional simulations of fluid flow in three-dimensional networks of discrete fractures', *Water Resources Research* **23**(10), 1876–1886.

Báez, E. & Nicolás, A. (2006), '2D natural convection flows in tilted cavities: Porous media and homogeneous fluids', *International Journal of Heat and Mass Transfer* **49**(25-26), 4773–4785.

Báez, E. & Nicolás, A. (2013), 'From cat's eyes to multiple disjoint natural convection flow in tall tilted cavities: A direct primitive variables approach', *Physics Letters A* **377**(37), 2270–2274.

Barenblatt, G. I., Entov, V. M. & Ryzhik, V. M. (1990), *Theory of fluid flows through natural rocks*, Kluwer Academic Publishers, Dordrecht.

Barenblatt, G. I., Zheltov, I. P. & Kochina, I. N. (1960), 'Basic concepts in the theory of seepage of homogeneous liquids in fissured rocks (strata)', *Journal of Applied Mathematics and Mechanics* **24**(5), 1286–1303.

Barletta, A. & Storesletten, L. (2011), 'Thermoconvective instabilities in an inclined porous channel heated from below', *International Journal of Heat and Mass Transfer* **54**(13-14), 2724–2733.

Baytaş, A. C. (2000), 'Entropy generation for natural convection in an inclined porous cavity', *International Journal of Heat and Mass Transfer* **43**(12), 2089–2099.

Baytaş, A. C. & Pop, I. (1999), 'Free convection in oblique enclosures filled with a porous medium', *International Journal of Heat and Mass Transfer* **42**(6), 1047–1057.

Bear, J. (1979), *Hydraulics of groundwater*, McGraw-Hill.

Berkowitz, B. (2002), 'Characterizing flow and transport in fractured geological media: A review', *Advances in Water Resources* **25**, 861–884.

Bertani, R. (2016), 'Geothermal power generation in the world 2010-2014 update report', *Geothermics* **60**, 31–43.

Bird, R. B., Stewart, W. E. & Lightfoot, E. N. (2002), *Transport phenomena*, John Wiley & Sons.

Black, J. H. & Barker, J. A. (2007), An investigation of "sparse channel networks", characteristic behaviors and their causes, Technical report, Svensk Kärnbränslehantering AB, Swedish Nuclear Fuel and Waste Management Co.

Bories, S. A. & Combarnous, M. A. (1973), 'Natural-convection in a sloping porous layer', *Journal of Fluid Mechanics* **57**(Jan 23), 63–79.

Brown, S. (1987), 'Fluid flow through rock joints: the effect of surface roughness', *Journal of Geophysical Research* **92**(B2), 1337–1347.

Cacas, M. C., Ledoux, E., De Marsily, G., Tillie, B., Barbreau, A., Durand, E., Feuga, B. & Peaudecerf, P. (1990), 'Modeling fracture flow with a stochastic discrete fracture network: calibration and validation 1. The flow model', *Water Resources Research* **26**(3), 479–489.

Caltagirone, J. P. & Bories, S. (1985), 'Solutions and stability criteria of natural convective flow in an inclined porous layer', *Journal of Fluid Mechanics* **155**(Jun), 267–287.

Capone, F., Gentile, M. & Hill, A. (2012), 'Convection problems in anisotropic porous media with nonhomogeneous porosity and thermal diffusivity', *Acta Applicandae Mathematicae* **122**(1, si), 85–91.

Carvalho, P. H. S. & de Lemos, M. J. S. (2013), 'Turbulent free convection in a porous square cavity using the thermal equilibirum model', *International Communications in Heat and Mass Transfer* **49**, 10–16.

Chen, S. H., Feng, X. M. & Isam, S. (2008), 'Numerical estimation of REV and permeability tensor for fractured rock masses by composite element method', *International Journal for Numerical and Analytical Methods in Geomechanics* **32**, 1459–1477.

Davis, G. & Jones, I. (1983), 'Natural-convection in a square cavity - a comparison exercise', *International Journal for Numerical Methods in Fluids* **3**(3), 227–248.

de Dreuzy, J. R., Méheust, Y. & Pichot, G. (2012), 'Influence of fracture scale heterogeneity on the flow properties of three-dimensional discrete fracture networks (DFN)', *Journal of Geophysical Research* **117**, B11207.

De La Torre Juárez, M. D. & Busse, F. H. (1995), 'Stability of 2-dimensional convection in a fluid-saturated porous-medium', *Journal of Fluid Mechanics* **292**, 305–323.

Elder, J. (1967), 'Steady free convection in a porous medium heated from below', *Journal of Fluid Mechanics* **27**(1), 29–48.

Evans, D. & Raffensperger, J. (1992), 'On the stream function for variable-density groundwater flow', *Water Resources Research* **28**(8), 2141–2145.

Fisher, A. (1998), 'Permeability within basaltic oceanic crust', *Reviews of Geophysics* **36**(2), 143–182.

Franco, A. & Vaccaro, M. (2012), 'An integrated "Reservoir-Plant" strategy for a sustainable and efficient use of geothermal resources', *Energy* **37**, 299–310.

Freeze, R. A. (1994), 'Henry Darcy and the fountains of Dijon', *Ground Water* **32**(1), 23–30.

Gerke, H. H. & Genuchten, M. T. (1993), 'Evaluation of a first-order water transfer term for variably saturated dual-porosity flow models', *Water Resources Research* **29**(4), 1225–1238.

Graf, T. & Therrien, R. (2008), 'A test case for the simulation of three-dimensional variable-density flow and solute transport in discretely-fractured porous media', *Advances in Water Resources* **31**, 1352–1363.

Graf, T. & Therrien, R. (2009), 'Stable-unstable flow of geothermal fluids in fractured rock', *Geofluids* **9**(2), 138–152.

Guillou-Frottier, L., Carre, C., Bourgine, B., Bouchot, V. & Genter, A. (2013), 'Structure of hydrothermal convection in the upper rhine graben as inferred from corrected temperature data and basin-scale numerical models', *Journal of Volcanology and Geothermal Research* **256**, 29–49.

Gutjahr, A. L., Gelhar, L. W., Bakr, A. A. & MacMillan, J. R. (1978), 'Stochastic analysis of spatial variability in subsurface flows. 2. Evaluation and application', *Water Resources Research* **14**(5), 953–959.

Gvirtzman, H., Garven, G. & Gvirtzman, G. (1997), 'Thermal anomalies associated with forced and free ground-water convection in the dead sea rift valley', *Geological Society of America Bulletin* **109**(9), 1167–1176.

Harfash, A. J. (2014), 'Three-dimensional simulations for convection problem in anisotropic porous media with nonhomogeneous porosity, thermal diffusivity, and variable gravity effects', *Transport in Porous Media* **102**(1), 43–57.

Hewitt, D. R., Neufeld, J. A. & Lister, J. (2014a), 'High Rayleigh number convection in a three-dimensional porous medium', *Journal of Fluid Mechanics* **748**, 879–895.

Hewitt, D. R., Neufeld, J. A. & Lister, J. R. (2014b), 'High Rayleigh number convection in a porous medium containing a thin low-permeability layer', *Journal of Fluid Mechanics* **756**, 844–869.

Holst, P. H. & Aziz, K. (1972), 'Transient three-dimensional natural-convection in confined porous media', *International Journal of Heat and Mass Transfer* **15**(1), 73–90.

Horne, R. N. (1979), 'Three-Dimensional natural-convection in a confined porous-medium heated from below', *Journal of Fluid Mechanics* **92**(JUN), 751–766.

Horton, C. W. & Rogers, F. T. (1945), 'Convection currents in a porous medium', *Journal of Applied Physics* **16**(6), 367–370.

Hurwitz, S., Ingebritsen, S. E. & Sorey, M. L. (2002), 'Episodic thermal perturbations associated with groundwater flow: An example from Kilauea Volcano, Hawaii', *Journal of Geophysical Research* **107**(B11), 2297.

Ingebritsen, S. E., Geiger, S., Hurwitz, S. & Driesner, T. (2010), 'Numerical simulation of magmatic hydrothermal systems', *Reviews of Geophysics* **48**, RG1002.

Jang, J. Y. & Tsai, W. L. (1988), 'Thermal-instability of 2 horizontal porous layers with a conductive partition', *International Journal of Heat and Mass Transfer* **31**(5), 993–1003.

Jupp, T. & Schultz, A. (2004), 'Physical balances in subseafloor hydrothermal convection cells', *Journal of Geophysical Research - Solid Earth* **109**(B5).

Kaneko, T., Mohtadi, M. F. & Aziz, K. (1974), 'Experimental study of natural convection in inclined porous media', *International Journal of Heat and Mass Transfer* **17**(4), 485–496.

Karniadakis, G., Beskok, A. & Aluru, N. (2005), *Microflows and nanoflows: Fundamentals and simulation*, Springer.

Karniadakis, G. E., Israeli, M. & Orszag, S. A. (1991), 'High-order splitting methods for the incompressible navier stokes equations', *Journal of Computational Physics* **97**(2), 414–443.

Khanafer, K. (2013), 'Fluid-structure interaction analysis of non-Darcian effects on natural convection in a porous enclosure', *International Journal of Heat and Mass Transfer* **58**(1-2), 382–394.

Kolditz, O. (2001), 'Non-linear flow in fractured rock', *International Journal of Numerical Methods for Heat & Fluid Flow* **11**(6), 547–575.

Landereau, P., Noetinger, B. & Quintard, M. (2001), 'Quasi-steady two-equation models for diffusive transport in fractured porous media: large-scale properties for densely fractured systems', *Advances in Water Resources* **19**, 863–876.

Lapwood, E. (1948), 'Convection of a fluid in a porous medium', *Proceedings of the Cambridge Philosophical Society* **44**(4), 508–521.

Lee, C. H. & Farmer, I. (1993), *Fluid flow in discontinuous rocks*, Chapman & Hall, London.

Li, J. H. & Zhang, L. M. (2010), 'Geometric parameters and REV of a crack network in soil', *Computers and Geotechniques* **37**, 466–475.

Long, J. C. S., Gilmour, P. & Witherspoon, P. A. (1985), 'A model for steady fluid flow in random three-dimensional networks of disc-shaped fractures', *Water Resources Research* **21**(8), 1105–1115.

Long, J. C. S., Remer, J. S., Wilson, C. R. & Witherspoon, P. A. (1982), 'Porous media equivalents for networks of discontinuous fractures', *Water Resources Research* **18**(3), 645–658.

Long, J. C. S. & Witherspoon, P. A. (1985), 'The relationship of the degree of interconnection to permeability in fracture networks', *Journal of Geophysical Research* **90**(B4), 3087–3098.

Mannington, W., O'Sullivan, M. & Bullivant, D. (2004), 'Computer modelling of the Wairakei-Tauhara geothermal system, New Zealand', *Geothermics* **33**, 401–419.

McKibbin, R. & O'Sullivan, M. J. (1980), 'Onset of convection in a layered porous-medium heated from below', *Journal of Fluid Mechanics* **96**, 375–393.

McKibbin, R. & O'Sullivan, M. J. (1981), 'Heat-transfer in a layered porous-medium heated from below', *Journal of Fluid Mechanics* **111**, 141–173.

McKibbin, R. & Tyvand, P. A. (1982), 'Anisotropic modeling of thermal-convection in multilayered porous-media', *Journal of Fluid Mechanics* **118**(May), 315–339.

Min, K. B., Jing, L. & Stephansson, O. (2004), 'Determining the equivalent permeability tensor for fractured rock masses using a stochastic REV approach: Method and application to the field data from Sellafield, UK', *Hydrogeology Journal* **12**, 497–510.

Moutsopoulos, K. N. & Tsihrintzis, V. A. (2009), 'Analytical Solutions and Simulation Approaches for Double Permeability Aquifers', *Water Resources Management* **23**, 395–415.

Moya, S. L., Ramos, E. & Sen, M. (1987), 'Numerical study of natural-convection in a tilted rectangular porous material', *International Journal of Heat and Mass Transfer* **30**(4), 741–756.

Müller, C., Siegesmund, S. & Blum, P. (2010), 'Evaluation of the representative elementary volume (REV) of a fractured geothermal sandstone reservoir', *Environmental Earth Sciences* **61**, 1713–1724.

Mustapha, H., Dimitrakopoulos, R., Graf, T. & Firoozabadi, A. (2010), 'An efficient method for discretizing 3D fractured media for subsurface flow and transport simulations', *International Journal for Numerical Methods in Fluids* **67**, 651–670.

Nield, D. A. & Bejan, A. (2013), *Convection in Porous Media*, 4th edn, Springer, New York.

Nield, D. A. & Kuznetsov, A. V. (2007), 'The effects of combined horizontal and vertical heterogeneity on the onset of convection in a porous medium', *International Journal of Heat and Mass Transfer* **50**(9-10), 1909–1915.

Nield, D. A. & Kuznetsov, A. V. (2008), 'The effects of combined horizontal and vertical heterogeneity on the onset of convection in a porous medium: Moderate heterogeneity', *International Journal of Heat and Mass Transfer* **51**(9-10), 2361–2367.

Nield, D. A. & Kuznetsov, A. V. (2013), 'Onset of convection with internal heating in a weakly heterogeneous porous medium', *Transport in Porous Media* **98**(3), 543–552.

Noorollahi, Y. & Itoi, R. (2011), 'Production capacity estimation by reservoir numerical simulation of northwest (NW) Sabalan geothermal field', *Energy* **36**, 4552–4569.

Oron, A. P. & Berkowitz, B. (1998), 'Flow in rock fractures: The local cubic law assumption reexamined', *Water Resources Research* **34**(11), 2811–2825.

Orszag, S. A., Israeli, M. & Deville, M. O. (1986), 'Boundary conditions for incompressible flows', *Journal of Scientific Computing* **1**(1), 75–111.

O'Sullivan, M. J., Pruess, K. & Lippmann, M. J. (2001), 'State of the art of geothermal reservoir simulation', *Geothermics* **30**, 395–429.

Patil, P. M. & Rees, D. A. S. (2014), 'The onset of convection in a porous layer with multiple horizontal solid partitions', *International Journal of Heat and Mass Transfer* **68**, 234–246.

Pruess, K. (1990), 'Modeling of geothermal reservoirs: fundamental processes, computer simulation and field applications', *Geothermics* **19**(1), 3–15.

Pruess, K. (1991), *TOUGH2 – a general-purpose numerical simulator for multiphase fluid and heat flow*, Earth Science Division, Lawrence Berkeley Laboratory.

Pruess, K. & Narasimhan, T. (1985), 'A practical method for modeling fluid and heat-flow in fractured porous-media', *Society of Petroleum Engineers Journal* **25**(1), 14–26.

Quintard, M. & Whitaker, S. (1996), 'Transport in chemically and mechanically heterogeneous porous media. I: Theoretical development of region-averaged equations for slightly compressible single-phase flow', *Advances in Water Resources* **19**(1), 29–47.

Rees, D. A. S. & Bassom, A. P. (2000), 'The onset of Darcy-Bénard convection in an inclined layer heated from below', *Acta Mechanica* **144**(1-2), 103–118.

Rees, D. A. S. & Genç, G. (2011), 'The onset of convection in porous layers with multiple horizontal partitions', *International Journal of Heat and Mass Transfer* **54**(13-14), 3081–3089.

Rees, D. A. S. & Riley, D. S. (1990), 'The 3-dimensional stability of finite-amplitude convection in a layered porous-medium heated from below', *Journal of Fluid Mechanics* **211**, 437–461.

Richard, J. & Gounot, J. (1981), 'Criterion for the onset of natural-convection in stratified porous layers', *International Journal of Heat and Mass Transfer* **24**(8), 1325–1334.

Riley, D. S. & Winters, K. H. (1990), 'A numerical bifurcation study of natural-convection in a tilted two-dimensional porous cavity', *Journal of Fluid Mechanics* **215**, 309–329.

Rosenberg, N. D. & Spera, F. J. (1990), 'Role of anisotropic and or layered permeability in hydrothermal convection', *Geophysical Research Letters* **17**(3), 235–238.

Sanyal, S. K., Butler, S. J., Swenson, D. & Hardeman, B. (2000a), 'Review of the state-of-the-art of numerical simulation of enhanced geothermal systems', *Proceedings of the World Geothermal Congress, Kyushu-Tohoku, Japan, 28 May-10 Jun. 2000* pp. 3853–3858.

Schubert, G. & Straus, J. M. (1979), 'Three-dimensional and multicellular steady and unsteady convection in fluid-saturated porous-media at high rayleigh numbers', *Journal of Fluid Mechanics* **94**(sep), 25–38.

Sen, M., Vasseur, P. & Robillard, L. (1987), 'Multiple steady-states for unicellular natural-convection in an inclined porous layer', *International Journal of Heat and Mass Transfer* **30**(10), 2097–2113.

Shapiro, A. M. & Andersson, J. (1983), 'Steady State fluid response in fractured rock: A boundary element solution for a coupled, discrete fracture continuum model', *Water Resources Research* **19**(4), 956–969.

Shewchuk, J. R. (2002), ' Delaunay refinement algorithms for triangular mesh generation', *Computational Geometry-Theory and Applications* **22**, 21–74.

Simmons, C. T. (2008), 'Henry Darcy (1803-1858): Immortalised by his scientific legacy', *Hydrogeology Journal* **16**(6), 1023–1038.

Snow, D. T. (1970), ' Frequency and apertures of fractures in rock', *International Journal of Rock Mechanics and Mining* **7**, 23–40.

Souche, A., Dabrowski, M. & Andersen, T. B. (2014), 'Modeling thermal convection in supradetachment basins: example from western Norway', *Geofluids* **14**(1), 58–74.

Straus, J. M. (1974), 'Large-amplitude convection in porous-media', *Journal of Fluid Mechanics* **64**(Jun), 51–63.

Tritton, D. J. (1988), *Physical fluid dynamics*, Clarendon, Oxford.

Tsang, C. F. & Neretnieks, I. (1998), 'Flow channeling in heterogeneous fractured rocks', *Reviews of Geophysics* **36**(2), 275–298.

Tsang, C. F., Tsang, Y. W. & Hale, F. V. (1991), 'Tracer transport in fractures: Analysis of field data based on a variable-aperture channel model', *Water Resources Research* **27**(12), 3095–3106.

Tsang, Y. W. & Tsang, C. F. (1987), 'Channel model of flow through fracture media', *Water Resources Research* **23**(3), 467–479.

Udell, K. S. (1985), 'Heat transfer in porous media considering phase change and capillarity - the heat pipe effect', *International Journal of Heat and Mass Transfer* **28**(2), 485–495.

Urmeneta, N. A., Fitzgerald, S. & Horne, R. N. (1998), The role of capillary forces in the natural state of fractured geothermal reservoirs, *in* 'Proceedings of the 23rd Workshop on Geothermal Reservoir Engineering', Vol. 26, Stanford University, Stanford, California, pp. 100–109.

Versteeg, H. K. & Malalasekera, W. (1995), *An Introduction to Computational Fluid Dynamics, The Finite Volume Method*, Prentice Hall.

Warren, J. E. & Root, P. J. (1963), 'The behavior of naturally fractured reservoirs', *Society of Petroleum Engineers* pp. 245–255.

Wellmann, J. F. & Regenauer-Lieb, K. (2015), 'How predictable are temperatures in geothermal resources', *Proceedings of the World Geothermal Congress, Melbourne, Australia, 19-25 April 2015* .

Wilkes, J. & Churchill, S. (1966), 'Finite-difference computation of natural convection in a rectangular enclosure', *A.I.Ch.E. Journal* **12**(1), 161–&.